UNIVERSITY OF CALIFORNIA
SANTA CRUZ

HIGH SPATIAL RESOLUTION THERMAL INFRARED INTEGRAL FIELD SPECTROSCOPY

A dissertation submitted in partial satisfaction of the
requirements for the degree of

DOCTOR OF PHILOSOPHY

in

ASTRONOMY AND ASTROPHYSICS

by

Zackery Wyatt Briesemeister

June 2022

The Dissertation of Zackery Wyatt Briesemeister
is approved:

Professor Andrew I. J. Skemer, Chair

Professor Rebecca Jensen-Clem

Professor Timothy D. Brandt

Professor Jason X. Prochaska

Peter Biehl
Vice Provost and Dean of Graduate Studies

Table of Contents

List of Figures

List of Tables

Abstract

High Spatial Resolution Thermal Infrared Integral Field Spectroscopy

by

Zackery Wyatt Briesemeister

I introduce high spatial resolution thermal infrared integral field spectroscopy to the astronomical community. The 2-5 micron sensitivity enables detection and characterization of a wide variety of exoplanets, including exoplanets detected through long-baseline astrometry, radial velocity planets on wide orbits, accreting protoplanets in nearby star-forming regions, and reflected-light planets around the nearest stars. I introduce ALES as the first thermal infrared integral field spectrograph, operating from 2.8–5 microns in multiple, low-resolution spectral modes. I used ALES to deliver the first spatially resolved thermal infrared spectra of the HD 130948BC system. I use the success of the ALES/LBTI thermal infrared integral field spectrograph to motivate the dedicated SCALES/Keck instrument, which vastly improves upon stability and sensitivity of the nascent technology to provide 10-m class diffraction limited thermal infrared low-/med-resolution spectra and imaging. I led the project to develop an end-to-end simulator for SCALES, and have used it to perform a novel information content analysis approach to identifying tolerances for SCALES. I identify the exoplanets detected using the astrometric baseline of *Hipparcos*, *Gaia*, and *Roman* as an age-insensitive sample

of "informed" targets to remove the potential risks of non-detections and improve the efficiency of detection and detailed imaging and spectroscopy of giant exoplanets with SCALES for a broad range of masses, separations, and ages.

I dedicate this thesis to my future dog,

Eccentric Kozai-Lidov Mechanism "Kozai" Briesemeister.

May there be many more dogs in my life.

Acknowledgments

I would like to effusively thank my advisor, Andy Skemer, for supporting me in every way I needed in graduate school. Emily Martin, Steph Sallum, Jordan Stone, and Deno Stelter have each helped me in innumerable ways, and I cannot thank them enough for the support they have given me. I want to thank Tim Brandt for writing postdoc letters and emphasizing the synergy of high-contrast imaging and astrometry that has led me to my postdoc at NASA Goddard. I also want to collectively thank my entire thesis committee, Andy Skemer, Becky Jensen-Clem, Tim Brandt, and X Prochaska, for supporting the completion of my thesis work. I must also thank the Eugene V. Cota-Robles Fellowship and the National Science Foundation Graduate Research Fellowship for funding my graduate work.

I thank my parents, Patrick and Lynda, every day for their love and support on this path through life. I thank my older brothers, Nick and Ben, for fostering my love for science, history, engineering, and nature. I became an uncle in January 2022 to Nick and his wife, Laura's, son, Fox. I couldn't stop smiling.

I am hostile towards the concept of COVID-19, but my quarantine pod with Callie Hood, Amanda Quirk, Enia Xhakaj, Grecco Oyarzun, and Matt Siebert has been critical to my mental (and often physical) well-being during the pandemic. Thank you all for the love and support!

The text of this thesis includes reprints of the following previously published material:

- Briesemeister, Z; Skemer, A. I. J.; Stone, J. M.; Stelter, R. D.; Hinz, P.; Leisenring, J.; Skrutskie, M. F.; Woodward, C. E.; Barman, T. S. 2018, *Proc. SPIE*, 10702, 107022Q, DOI: 10.1117/12.2312859, ©SPIE. Reproduced with permission

- Briesemeister, Z. W.; Skemer, A. I. J.; Stone, J. M.; Barman, T. S.; Hinz, P.; Leisenring, J.; Skrutskie, M. F.; Woodward, C. E.; Spalding, E. 2019, AJ, 157, 6, 244, DOI: 10.3847/1538-3881/ab1901, ©AAS. Reproduced with permission

- Briesemeister, Z.; Sallum, S.; Skemer, A. I. J.; Stelter, R. D.; Hinz, P.; Brandt, T. 2020, *Proc. SPIE*, 11477, 114474Z, DOI: 10.1117/12.2562143, ©SPIE. Reproduced with permission

- Briesemeister, Z.; Sallum, S.; Skemer, A. I. J.; Batalha, N. 2021, *Proc. SPIE*, 11823, 1182308, DOI: 10.1117/12.2594880, ©SPIE. Reproduced with permission

The co-authors listed in these publications directed and supervised the research which forms the basis for the thesis.

Chapter 1

Introduction

Vision has long been an important concept to human beings. Not only in the ability to think about or plan the future with imagination or wisdom, but in the capacity to detect electromagnetic waves that we use to interpret the universe around us. The human eye is truly a marvel of evolutionary biology, comprising an adjustable aperture (iris) and color-sensitive detector (retina) that nearly all humans use to collect a tiny fraction of electromagnetic spectrum and form a basis of architecture for many modern optical imaging systems. With the birth of modern astronomy with Galileo's first use of a telescope around 1609, astronomical observations were no longer limited to the power of the unaided eye. Telescopes remained extensions of the human eye until the invention of photography in the 19th century, enabling astronomers to store and share objective reproductions of

their observations. The manufacturing of optical glasses of constant quality spread matured optical systems such as telescopes, microscopes, and photographic objectives into scientific, medical and consumer applications. Digital detectors have recently replaced the need for photographic plates, delivering astronomy into the modern era where advanced post-processing algorithms performed by computers have dramatically accelerated scientific discovery. Astronomical instrument technology has expanded narrow wavelength coverage from those visible to the human eye to the entire electromagnetic spectrum.

It took foresight for astronomers to collectively direct resources towards overcoming the challenges besetting the field of high-contrast (direct) imaging of exoplanets, which takes vision to the extreme. The angular resolution of the naked human eye, or the smallest angular separation with which the human eye can distinguish two point sources from one another, is around an arcminute. Typical angular resolutions of high-contrast imaging systems are $\sim$50 millarcseconds, or a factor 1200 smaller. At the same time, stars are typically a million (Jupiter-like) to a billion (Earth-like) times brighter than the exoplanets that orbit them.

While the premise of direct imaging is straightforward, in practice it is quite complex. Geometrically, distant planetary systems are fainter and more compact when viewed from Earth. Astrophysically, the intrisically high-contrast environments, coupled with the intrinsic rarity of wide-separation companions and the

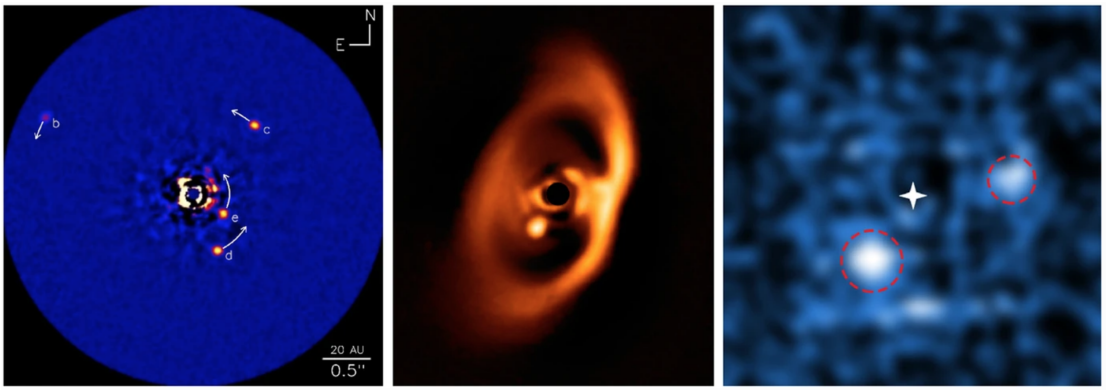

Figure 1.1: The two directly imaged systems with multiple planets so far, with Left: HR 8799, Middle: PDS 70, Right: PDS 70. Image credits: C.Marois; Müller et al.; S. Haffert.

long-term passive cooling of their atmospheres, conspire to make detection rates low. Locally, turbulence in Earth's atmosphere degrades image quality, and the atmosphere's bright, highly variable thermal background redward of 2 microns is also plagued with OH lines in the near infrared. From an engineering standpoint, stellar light would saturate detectors in the integration time necessary to observe exoplanetary photons, and the emissive optics and thermal background warrants cryogenic instruments. Technically, characterization of exoplanet light requires sophisticated instrumentation and data processing infrastructure.

An uphill challenge reaps rich reward, however few (Figure 1.1). High-contrast imaging presents major advantages over other techniques for detecting exoplanets *and* enables their characterization. Unambiguously separating stellar light from

the light emitted (or reflected) by an exoplanet enables isolation of their thermal emission (or reflection) spectra with spectrographs, providing constraints on the chemical compositions, pressure–temperature profiles, and energy transport in exoplanetary atmospheres (e.g., Konopacky et al., 2013; Macintosh et al., 2015a; Hu, 2019). Transit detections are limited to compact edge-on orbits, and radial velocity are most sensitive to massive exoplanets on short, near edge-on orbits. High-contrast imaging is not geometrically restricted (apart from being limited by small angular separation from the star) and is most sensitive to massive exoplanets at wide separation. Fecund transit and radial velocity surveys are biased towards older systems, as young stars produce a large quantity of pathological astrophysical noise (star spots, circumstellar material, etc.; Crockett et al., 2012; van Eyken et al., 2012; Yu et al., 2015). High-contrast imaging is most sensitive to young, self-luminous gas giants. These rewards, in turn, populate the otherwise underexplored region of exoplanet parameter space.

NASA's *Kepler* mission has shown planets are ubiquitous: 50-100% of Sun-like stars host some form of planetary system (Winn and Fabrycky, 2015), with 10-20% expected to host one or more rocky planets (Fressin et al., 2013; Petigura et al., 2013). Large surveys from Keck and other facilities (e.g., Galicher et al., 2016; Nielsen et al., 2019) have now indicated that directly observable exoplanets (i.e., young gas giants orbiting far from their host star) are rare, with estimates of a few

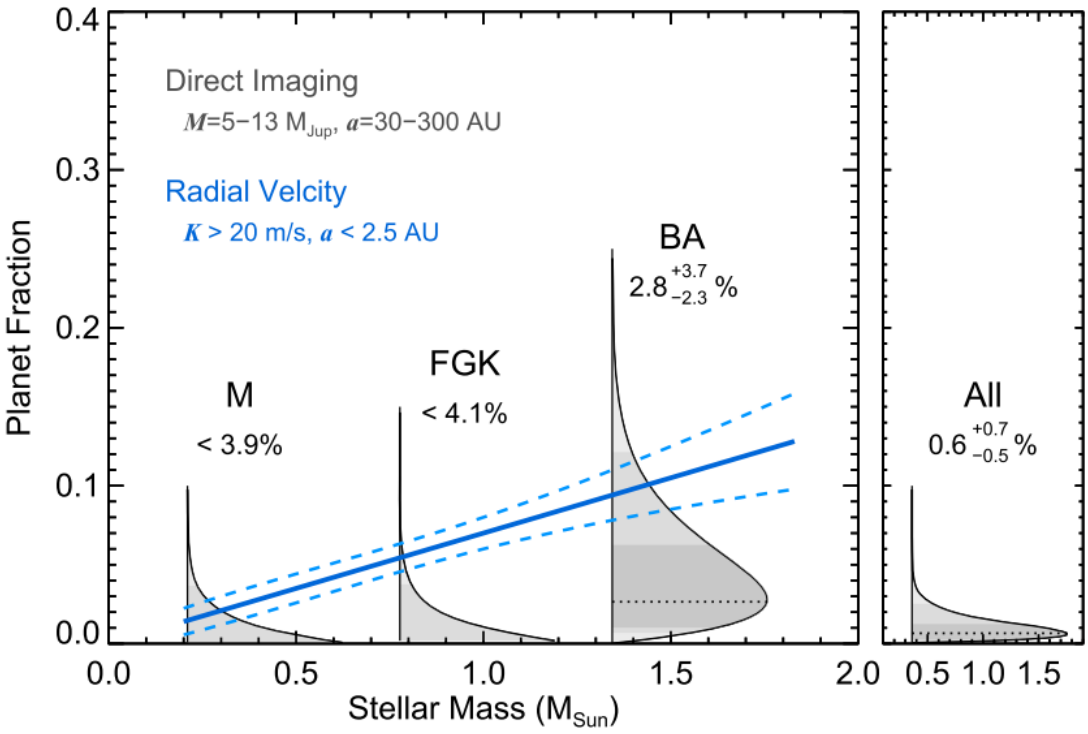

Figure 1.2: Probability distributions for the occurrence rate of giant planets for four populations of host stars. From (Bowler, 2016), Figure 12.

percent of stars host such giant planets (Figure 1.2). This is in agreement with the gas giant occurrence rate inferred from radial velocity data, which suggests a peak in the giant planet distribution around the snow line (∼2-5 AU around a young Sun-like star; Mulders et al., 2015) with a decline to a few percent further out (Fernandes et al., 2019). Adaptive optics-fed direct imaging surveys that have invested >1000 nights of 8–10-m telescope time to discover ∼1–2 dozen exoplanets (Bowler, 2016).

Nevertheless, understanding the formation and evolution of giant planets is a fundamental goal of modern astrophysics. New scientific frontiers such as exoplanetology and astrobiology rely on the wealth of information gathered from the detection and characterization of the entire range of exoplanet formation outcomes. The tacit goal of exploring terrestrial habitability cannot be understood in isolation. Jupiter and Saturn likely played an important role for the formation and evolution of the Solar System, and have predominantly dictated its present-day architecture (Morbidelli et al., 2007). This migration may provide explanations for the peculiar axial tilt of Uranus and Venus, the catastrophic impact that may have been responsible for the formation of the Moon, the Late Heavy Bombardment and the presence and distribution of planetesimals in the solar system (Thommes et al., 1999; Gomes et al., 2005; Tsiganis et al., 2005; Levison et al., 2008). Giant planets accrete large amounts of matter from the protoplanetary disk and can open gaps in the disk's radial dust distribution which form barriers for radial dust drift, limiting the amount of material available for the formation of smaller planets closer in (Rice et al., 2006). They also gravitationally interact with planets in the system and the protoplanetary disk itself, causing orbital resonances and migration (D'Angelo and Marzari, 2012).

This discussion can be broadly expanded to include all substellar companions, including brown dwarfs (typically confined to the mass regime above the

deuterium burning limit ($13M_J$) and below the hydrogen burning limit ($75M_J$); Oppenheimer et al., 2000). Brown dwarfs are of scientific interest in their own right, but their usage as analogs for exoplanets due to their similarities in color space (Figure 1.3) and relative ease of measurement cannot be understated (e.g., Cushing et al., 2005; Miles et al., 2018). Substellar objects lack of a sustainable source of internal energy from nuclear reactions, with more massive objects starting hotter and more luminous then gradually cooling and contracting. As this occurs, its surface gravity will increase, making log(g) a tracer of age (Martin et al., 2017). Young, low surface gravity objects are particularly analogous to directly imaged exoplanets; clouds are a nearly universal feature, with thicker cloud decks appearing in low gravity objects (Helling and Casewell, 2014).

A class of dedicated high-contrast imaging systems comprising integral field spectrographs capable of characterizing exoplanet atmospheres amongst other astrophysical features have come online in the past two decades. Project 1640 at Palomar (P1640; Claudi et al., 2008), Gemini Planet Imager (GPI; Macintosh et al., 2008), Spectro-Polarimetric High-contrast Exoplanet REsearch (Claudi et al., 2008, SPHERE;), and Coronagraphic High Angular Resolution Imaging Spectrograph (CHARIS; McElwain et al., 2012) collectively observe blueward of 2.5 microns with the goal of imaging exoplanetary systems at separations below 10 AU. These instruments continue to find fewer giant exoplanets than predicted,

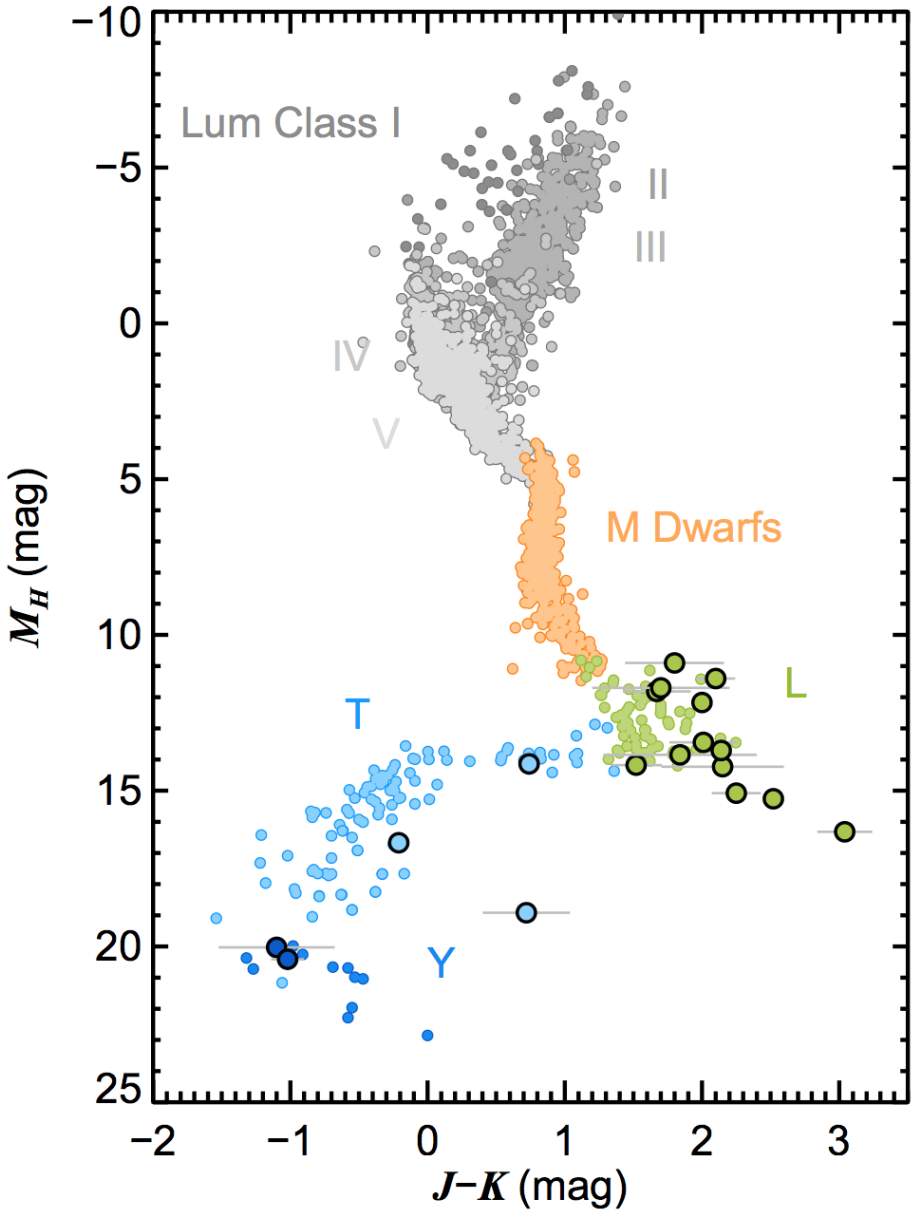

Figure 1.3: Color-magnitude diagrams for several directly imaged planetary mass companions in bold circles with amongst field LT-type brown dwarfs and stars. From Bowler (2016), Figure 7.

suggesting the discrepancy between the planet mass function extrapolated from radial velocity surveys and the true giant exoplanet mass function remains unresolved. Near-infrared spectra alone are also insufficient for precise atmospheric constraints of substellar atmospheres due to degeneracies between effective temperature, cloud coverage, convection and non-equilibrium carbon chemistry (e.g., Stephens et al., 2009; Skemer et al., 2014; Barman et al., 2015).

In the thermal infrared (3–5 μm), the spectral energy distribution (SED) of gas-giant planets contains a low-opacity atmospheric window that emits a large fraction of a planet's flux (Figure 1.4), especially at cool temperatures. Major atmospheric absorbers, such as CH_4, CO and H_2O, have strong absorption features at $\sim 3.3\mu$m, $\sim 4.7\mu$m and $\sim 4-5\mu$m, respectively. Additionally, the thermal infrared continuum shape is sensitive to cloud thickness and patchiness (Madhusudhan et al., 2011; Currie et al., 2011; Skemer et al., 2014). Previous works have exploited broad wavelength spectrophotometry extending into the thermal infrared in order to constrain the thermal profiles, compositions, cloud properties and bolometric luminosities of gas-giant planets (e.g., Currie et al., 2011; Barman et al., 2011; Madhusudhan et al., 2011; Marley et al., 2012; Skemer et al., 2012, 2014; Ingraham et al., 2014; Morzinski et al., 2015; Rajan et al., 2017).

The rest of the introduction expounds upon these ideas and endeavors to motivate the development of a new class of high-contrast imaging system capable

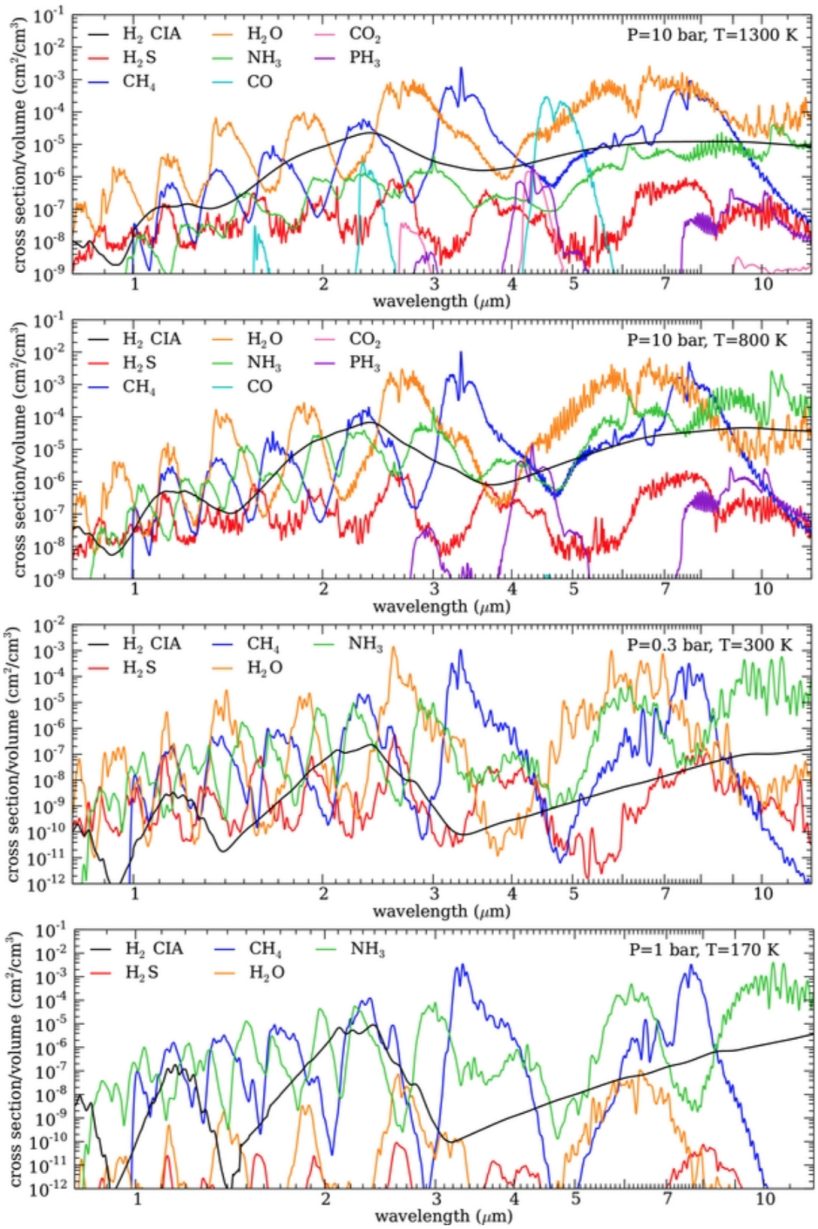

Figure 1.4: Opacities of the major molecular species in these cool atmosphere of exoplanets. In wavelength regions of lower net opacity enable observers to see deeper into the atmosphere. From Morley et al. (2014), Figure 7.

of performing integral field spectroscopy at thermal infrared that will be the topic of this thesis.

1.1 Overcoming the Challenges to Direct Imaging

At the most abstract level, detection of a companion to a star through high-contrast imaging is determined by the companion's brightness and the capacity to separate the companion light from its hosts' light. The brightness of the companion is tied deeply to its formation history, and is discussed in the next subsection. For the latter point, the point-spread function (PSF), which represents intensity impulse response of the optical system, has a shape set by the geometry of the entrance pupil and the wavelength of light (λ). The limit of an optical system to distinguish light from the companion and light from the host is set by the ability to distinguish their unaberrated point spread functions from one another, known as the diffraction limit or Rayleigh Criterion (typically $1.22\lambda/D$, where D is the diameter of the telescope).

While infrared interferometric imaging methods like aperture masking (Tuthill et al., 2000) and kernel-phase interferometry (Martinache, 2010) can probe within the typical diffraction limit, conventional imaging is constrained not only by this limit, but by photon noise due to the bright star near its diffraction core, effectively widening the minimum distance to distinguish between star and planet. In real

high-contrast imaging systems, coronagraphic optics, adaptive optics, and post-processing set the inner working angle (IWA), defined as the smallest angular separation at which the total energy throughput of an off-axis source reaches 50% of the maximum throughput, or where the contrast reaches a threshold value (Ruane et al., 2018).

Such high-contrast imaging systems comprise the collection of technologies that provide the spatial resolution required to separate stellar light from exoplanet light, suppress starlight and remove diffraction structure at the location of the planet, exploit the physics of light to enable characterization and enhance contrast, and record and process the information obtained.

In this section, we discuss giant planet formation theory in the context of high-contrast imaging, and the role of adaptive optics, coronagraphy, and differential imaging in high-contrast imaging systems.

1.1.1 Giant Planet Formation

With the lack of a sustainable source of internal energy from nuclear reactions, exoplanets are born at their hottest and evolve by gradually cooling and contracting. One way to *a priori* alleviate challenges is to observe younger planets that are still bright due to not having radiated away most of their primordial heat of formation. In fact, *all* of the currently known directly imaged exoplan-

ets beneath the deuterium burning limit (13 M_J) orbit young ($\lesssim$ 100 Myr) stars (Bowler, 2016). Consequently, we have unprecedented access to young and forming planetary system, but are less sensitive to mature systems beyond the water iceline.

Contrast describes the ratio of flux from the companion and the host star, with the terminology of high- or extreme-contrast referring to contrasts closer to zero than unity. Characteristic examples of contrasts with respect to a G2V star as a function of wavelength are shown in Figure 1.5 for two near-infrared (1-2.5 μm) bands (H and K_s) and two thermal infrared (2.5-5.2μm) bands (L' and M'). If the goal of direct imaging is to extend to mature, and typically cooler, exoplanets to bridge the gaps in parameter space, **the optimal method for direct characterization of these exoplanets is using thermal infrared integral field spectroscopy.** The rest of this subsection is devoted to explaining why this is the case.

The initial conditions for planet formation are set by the host star formation and cannot be understood independently. Stars form from large, cold clouds of molecular gas in the interstellar medium, in which small overdensities create gravitational instabilities that lead to local collapse into protostellar cores (McKee and Ostriker, 2007). With some initial angular momentum, the collapsing cloud will flatten and form a disk with the protostar at its center. The surrounding

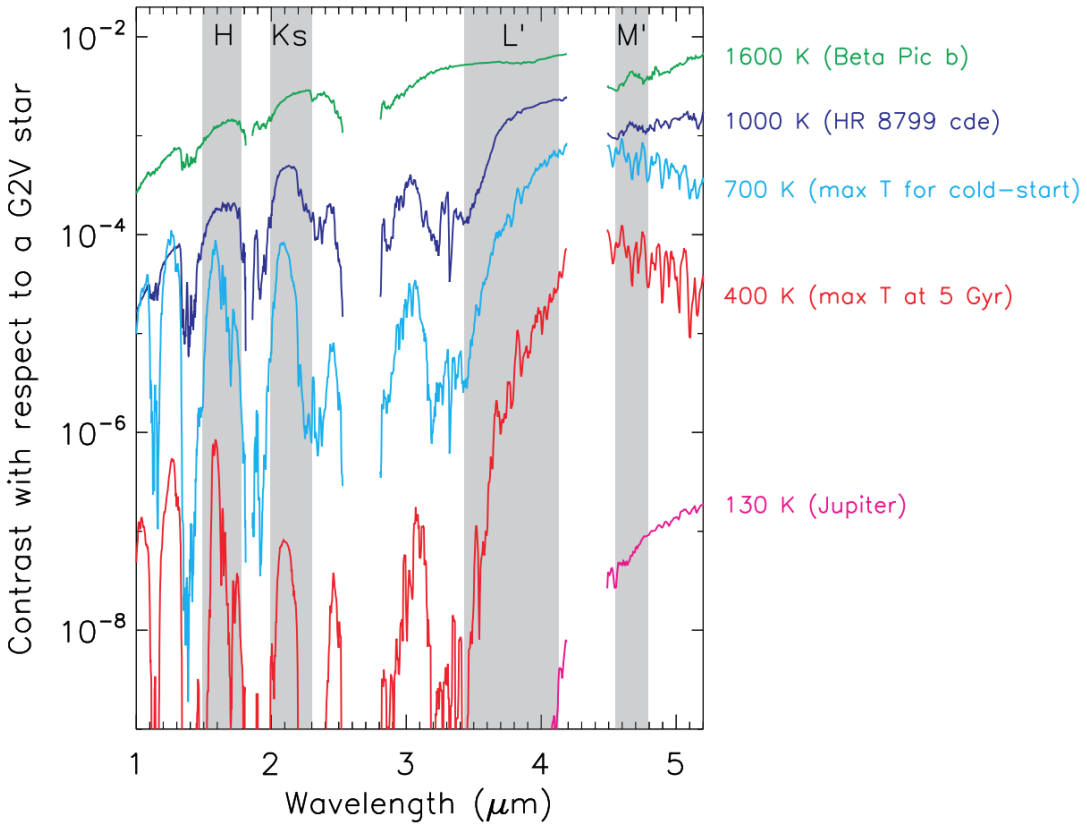

Figure 1.5: Characteristic examples of contrasts as a function of wavelength. The least contrast is apparent in the mid-infrared (3–5 micron) than in the near-infrared (1–2 micron), and this trend increases at lower temperatures. From Skemer et al. (2014), Figure 1.

dust and gas will gather into the circumstellar disk, which is thought to be the birth place of planets and is therefore also called a protoplanetary disk. There are several proposed mechanisms of planet formation that fall into three categories:

- Core accretion is a process where planets are formed from the bottom up, beginning with dust particles that gradually coagulate into a protoplanetary core (Pollack et al., 1996). If a planetary core reaches critical mass before the dissipation of the circumstellar disk, a gaseous envelope is runaway accreted resulting in a giant planet. The process is limited to the life time of the gaseous component of the protoplanetary disk, set by radiation pressure from the protostar. Gas-giant planet formation is thought to be most efficient near the water ice line (∼3-5 AU in solar-type systems), where an abrupt change in the drift speeds of grains with and without icy mantels causes increased surface density of solids enhancing core growth (Banzatti et al., 2015; Pinilla et al., 2016).

- Disk fragmentation are scenarios in which massive protoplanetary disks becomes unstable and fragments into self-gravitating clumps (Boss, 1997). However, ALMA observation revealed such massive disks are rare (Andrews et al., 2013). Magneto-rotational instabilities may also cause disk fragmentation leading to planet formation (Chiang and Youdin, 2010).

- During the collapse of the pre-stellar core the clump of gas and dust can

break up into seperate clumps, which continue to contract and form planets (Hennebelle and Chabrier, 2008).

The combined evidence, including planetary orbital distributions (e.g., Cumming et al., 2008), planet frequency correlations with host-star properties such as metallicity (e.g., Fischer and Valenti, 2005), and to some extent planetary atmospheric composition (e.g., Skemer et al., 2016b), and the planet mass-radius distribution (Thorngren and Fortney, 2016), suggests that planets dominantly form via core accretion, but it is possible that all three processes play a part in the formation of planets. High-contrast imaging surveys such as SHINE (Vigan et al., 2021) and GPIES (Nielsen et al., 2019) have found a smaller than expected number of planets at wide separations (where gravitational instability is more efficient), indicating that an even higher fraction might have formed via core accretion than previously expected.

Gravitational instability and core accretion mechanisms predicts distinct post-formation specific entropies for giant planets (Figure 1.6). Formation via gravitational instability (hot accretion) predicts characteristically high post-formation specific entropy, which increases with increasing planet mass (Figure 1.6). With increasing planet mass, an increasing amount of gravitational potential energy is converted to thermal energy during formation and stored in the planet. Formation via core accretion (cold accretion) predicts a decrease in post-formation specific

entropy with increasing planet mass, meaning with increasing planet mass, thermal energy is radiated away in efficient accretion shocks (Marley et al., 2007a). More realistic dissipative accretion shocks predict an intermediate regime (warm accretion; Marleau and Cumming, 2014).

Meanwhile, planet-disk interaction can influence the orbital distance of the planet. The more massive planets carve deep gaps in the disk, as they are able to sweep up a major part of the disk material in their orbit. The depletion of the dust and gas in the disk changes the pressure gradient and forces the planet to migrate (type-I migration; Kley, 2017; Nelson et al., 2000). Planets of a few Earth masses follow a type-II migration scenario (Nelson et al., 2000), where only a small shallow gap is created that is not completely cleared of dust and gas. The consequential distinction between the two types is the amount of mass accretion that occurs. Multiple planet systems inevitably complicate the dynamics involved, but the expected ubiquity of such situations undergoing type-III migration warranted the development of hydrodynamical simulations and semi-analytical relations between the migration rate, disk parameters and planet parameters (Dodson-Robinson and Salyk, 2011; Kley, 2017).

Planet-population synthesis codes attempt to replicate observed exoplanet populations by placing these semi-analytical relations in a single simulation environment to test theories of planet formation (Benz et al., 2014; Mulders et al.,

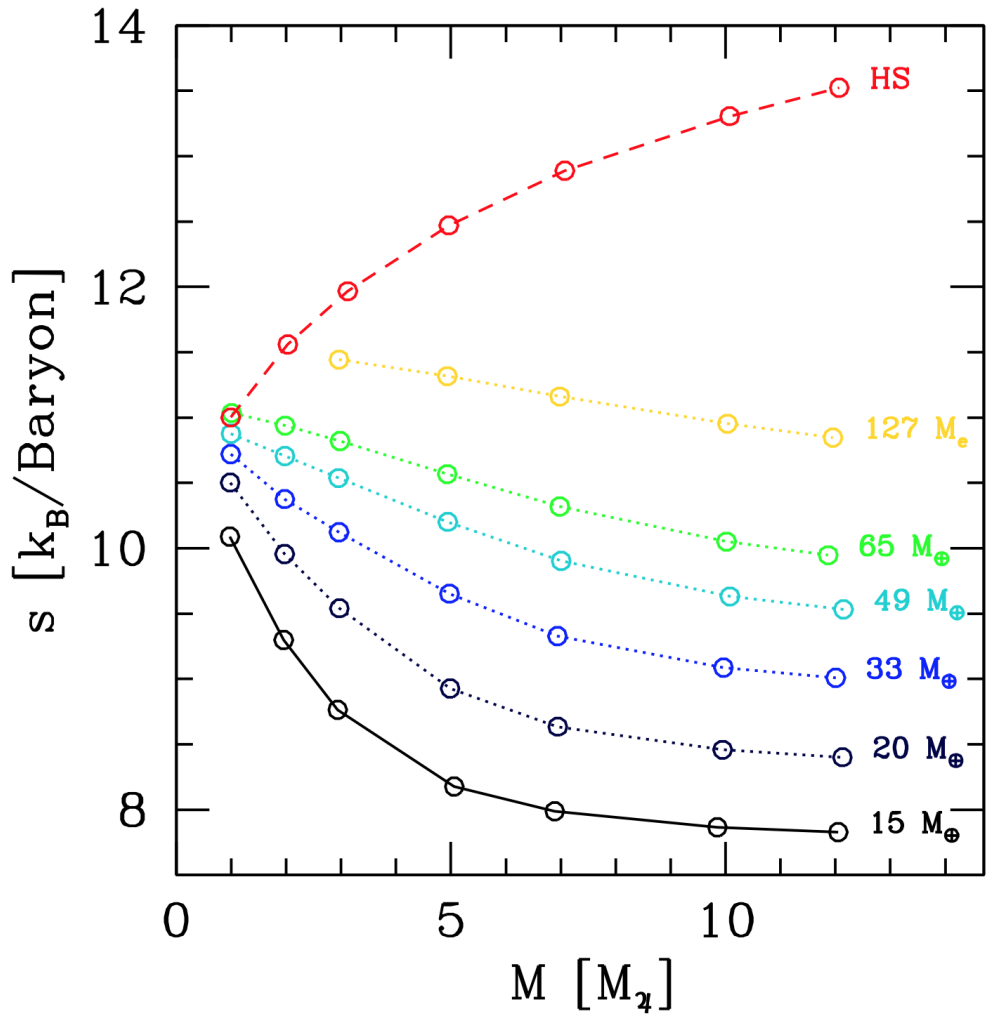

Figure 1.6: Post-formation specific entropy as a function of planet mass for giant planets formed via gravitational instability (HS, red line) and core accretion featuring different core masses (other lines) at cold- and warm-start regimes. From Mordasini (2013), Figure 2.

2018). The underlying bias is apparent: transit and radial velocity surveys eschew young stars with pathological astrophysical noise (star spots, circumstellar material, etc.) in favor of older, more well-behaved stars (Crockett et al., 2012; van Eyken et al., 2012; Yu et al., 2015). Presently, theories describing the details of how planets form are guided almost entirely by indirect constraints from the appearance and statistics of mature planets. While these simulations have been fruitful, we lack the verification of most of the physical mechanisms in these population codes (Morbidelli and Raymond, 2016).

Direct imaging is key to overcoming these observational limitations. By spatially resolving the disk and the embedded planets, we can witness their interaction. Another added benefit is the enhanced intrinsic contrast between the star and the planets. Reflected light detections are essentially the only option for Solar System-analogs. The contrast for analog-Earth and analog-Jupiter would be 10^{-10} – 10^{-9}, respectively (Traub and Oppenheimer, 2010), far beyond our current capabilities. But planets emerge from formation at their hottest. This increases the intrinsic contrast in the near-infrared to 10^{-5} – 10^{-6} making the detection of such exoplanets orders of magnitude easier, and even more so beyond 3 microns (Figure 1.7); direct imaging is the best technique to observe young planetary systems and their planet-disk interactions.

Planets formed via core-accretion are born with a distribution of initial en-

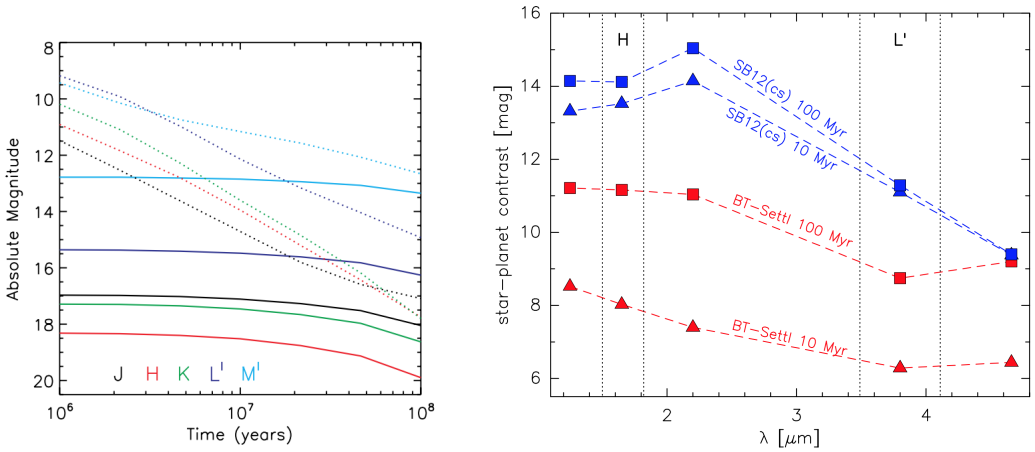

Figure 1.7: Left: The evolution of absolute magnitudes in five infrared bands for a 4 M_J planet. Solid lines show the core accretion start model, while dashed lines show the high initial-entropy start model. From Fortney et al. (2008), Figure 8. Right: Star-planet contrast for a 1 $M_\odot$ star and a 10 M_J planet as a function of wavelength for two different ages and two evolutionary models (blue: Spiegel and Burrows (2012), cold start; red: Allard (2014), hot start). From Launhardt et al. (2020), Figure 2.

tropies, resulting in a distribution of zero-age luminosities for planets of a given mass (e.g., Mordasini, 2013). In the near infrared (<2.5 micron), even the most massive low initial-entropy planets are typically too cool and faint to be detected. These planets are easier to detect in the thermal infrared (3-5 micron), but they cool and fade out of reach at mature ages (e.g., Marley et al., 2007b; Skemer et al., 2014). Therefore, thermal infrared observations of the youngest possible targets are necessary to directly image planets with the full range of expected initial entropies, and if there is any hope to image mature objects, it would be redward of 3 microns.

Since the youngest stars are typically at distances >100 pc, resolving the stellocentric radii where giant planet formation should be most efficient requires very high spatial resolution. Unambiguously separating stellar light from the light emitted by an exoplanet enables isolation of their thermal emission spectra, providing constraints on the chemical compositions, pressure–temperature profiles, and energy transport in exoplanetary atmospheres (e.g., Konopacky et al., 2013; Macintosh et al., 2015a; Miles et al., 2020). The instrument most capable of performing such observation would, in turn, be a thermal infrared-sensitive integral field spectrograph with high spatial resolution.

1.1.2 Adaptive Optics

A key obstacle to overcome is optical distortion caused by Earth's atmosphere. Atmospheric layers have temperature differences and potentially pressure differences that change the local refractive index of the air, and the difference in wind speed and direction generates turbulence between these layers. Turbulence changes the optical path and thus arrival times of light across the telescope pupil, distorting the wavefront temporally and spatially. The point-spread function (PSF), which represents intensity impulse response of the optical system becomes aberrated, degrading the spatial resolution of any uncorrected instrument. This phase distortion changes on the order of milliseconds, which results in long-exposure images appearing as smooth, extended seeing halos that contains little spatial information

Adaptive optics (AO) seeks to correct this atmospheric wavefront distortion in real time. AO systems actively measure the shape of the wavefront with a wavefront sensor (WFS), typically measures the wavefront by converting wavefront shape to an intensity modulation, like spot shifts or intensity variations. The signal from the WFS is converted by a control algorithm to shape a deformable mirror (DM), which takes the inverted shape of the wavefront with half the amplitude and thereby flattening it to approach the theoretical unaberrated PSF for the optical system. A DM placed before the wavefront sensor enables

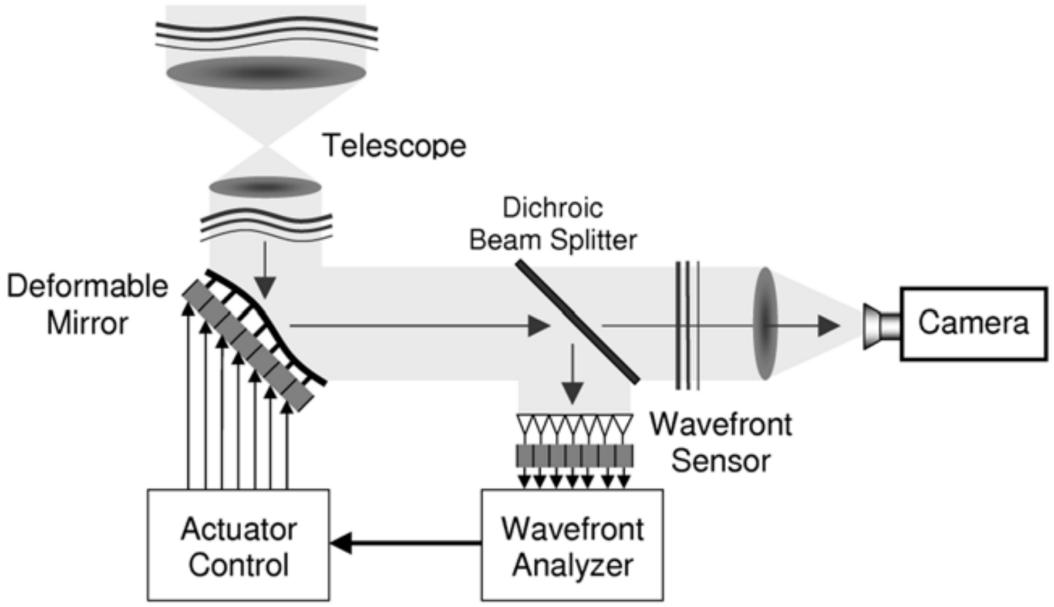

Figure 1.8: The principle components of an adaptive optics (AO) system. From Zhu et al. (2006), Figure 1.

closed loop activity to keep the wavefront stable (Figure 1.8). Aberrated PSFs have significant power exterior from their central core, causing both stellar and exoplanet light to be spread over a wider area. This decreases the localization of the exoplanet, decreases the number of photons we associate with the planet, and make already unfavorable contrasts even more untenable. The improvement by AO is two-fold: the spatial resolution *and* signal-to-noise is improved as the light becomes more centrally concentrated to the location of the source.

Temporal delays, atmospheric evolution (primarily wind), and other factors conspire to cause the DM to imperfectly correct the wavefront. Imperfect correc-

tion causes the PSF to exhibit modulations of the intensity with a size of λ/D that mimic planet signals called speckles. Speckles are coherent with the diffraction structure and are generated by many effects, dominated by non-common path errors between the WFS and science focal plane and temporal lag of updating the DM. These result in long-lived speckles resembling planets (Martinez et al., 2013), and wind-driven halos of unocculted stellar light (Cantalloube et al., 2018, 2020), respectively. Wavefront sensing at the science focal plane and predictive control by extrapolating wavefronts due to wind may be solutions to these respective problems (e.g., Marois et al., 2020; van Kooten et al., 2019).

While we focus here on ground-based instrumentation, it is important to note space-based instruments only escape the effects of Earth's atmosphere, and the other challenges remain. Their performance is also limited by wavefront control, albeit at a very different contrast level (Shi et al., 2017).

1.1.3 Coronography

After AO correction, the diffraction structure still dominates over planetary light. The fundamental purpose of a coronagraph is to act as an angular filter, suppressing on-axis light as much as possible with minimal disruption to the off-axis astrophysical light. Coronagraph are designed to suppress this diffraction structure at the location where planets are expected to be, and suppress photon

noise associated with stellar light. As such, coronagraphy significantly enhances the signal-to-noise ratio of the planet signal.

The archetypal coronagraph was developed by Bernard Lyot to image the solar corona by masking the disk of the sun and blocking the diffracted light in a consecutive pupil plane (Lyot, 1939). As an example of a focal-plane coronagraph, the Lyot coronagraph's suppression properties can be visualized in Figure 1.9, which has an opaque mask in the focal plane that blocks the starlight. An amplitude mask (or Lyot stop) in the following pupil plane blocks the stellar light that is diffracted around the opaque focal-plane mask. The Lyot coronagraph is a focal-plane coronagraph, as the opaque mask that blocks the star is in the focal plane. The field has expanded to several designs acting in either the focal or pupil planes (Ruane et al., 2018).

Focal-plane coronagraphs use an opaque focal-plane mask to block out the starlight in an intermediate image plane, and employ pupil stops upstream and downstream in order to optimally suppress diffraction effects. As the IWA becomes smaller, focal-plane coronagraphs become increasingly sensitive to errors in instrumental alignment, and any shift to the central star will cause it to move out of the nulling region and re-appear in the image, significantly degrading contrast. Pathological vibrations in the telescope conspire to undermine the effectiveness of high-precision focal-plane coronagraphs (Mawet et al., 2012).

Pupil-plane coronagraphs use apodising optics in the telescope pupil to modify the PSF of the telescope, creating regions of destructive interference where the natural diffraction pattern is suppressed. Since every PSF is modified the same way regardless of position, vibrations are no longer pathological. The trade-off is lower image quality, as the modified PSF is less centrally concentrated.

A more precise definition of contrast is the flux ratio with respect to the star where a point source can be significantly (5σ) detected (Jensen-Clem et al., 2018). For a coronagraph design, the contrast is the spatially variant suppression of the starlight divided by the coronagraphic throughput for a clear telescope aperture, measured in a circle with a diameter of approximately the diffraction limit.

1.1.4 Differential Imaging

The contrast improved through adaptive optics and coronography can be further enhanced through a variety of post-processing techniques. Imaging, spectroscopy, and polarimetry enable differential measurements that can be exploited to suppress residual stellar light and isolate exoplanetary light, including reference star differential imaging (RDI), angular differential imaging (ADI), spectral differential imaging (SDI), and polarimatric differential imaging (PDI).

ADI (Figure 1.10) relies on the pupil being stabilized as the sky rotates, fixing the stellar PSF diffraction structure with respect to the sky rotation (Marois

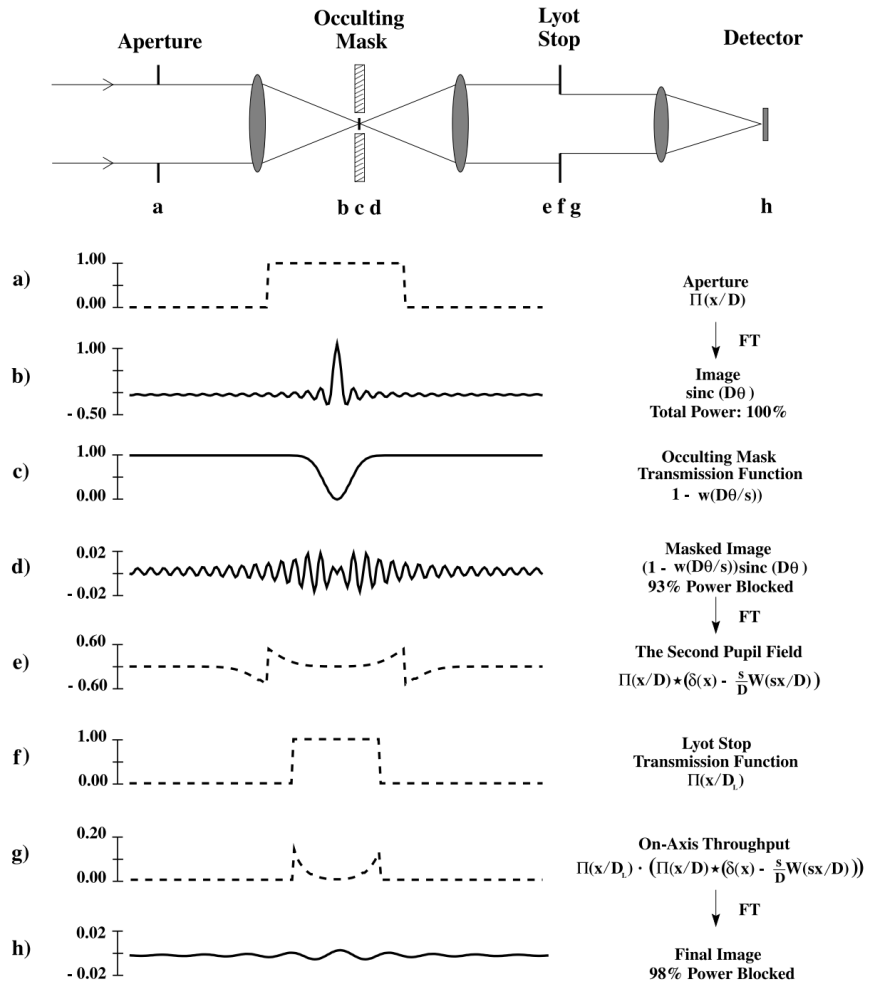

Figure 1.9: Schematic of Lyot coronography. The occulting spot, in the focal plane, occults the core of the target star PSF. In the re-imaged pupil plane, light from the spatially extended diffraction rings of the PSF is concentrated near the perimeter of the pupil. By adding a "Lyot stop" in this pupil plane, the diffraction rings are attenuated in the final image, thus boosting the overall dynamic range. From Sivaramakrishnan et al. (2001), Figure 1.

et al., 2006). This method relies on the angular diversity of off-axis object that rotate with the evolution of parallactic angle. The median image approximately removes all contribution of off-axis light, and when subsequent images are median-subtracted, derotated, and stacked, off-axis light is revealed. More advanced methods of combining the images to create a better reference PSF produce better results (Lafrenière et al., 2007; Soummer et al., 2012). Small angular diversity (typically small separation sources) appear more often near the same place in the mean image, resulting in self-subtraction that influences the interpreted spectrum.

RDI removes the stellar PSF component through subtraction of a PSF of another star (without companions, at least in the same location as the target), first used by (Smith and Terrile, 1984) to reveal the circumstellar disk around β Pictoris. RDI is severely limited by quasi-static speckles due to the time lag between data and reference image acquisitions.

SDI (Figure 1.11) takes advantage of spectral diversity of exoplanet and stellar light to suppress the stellar PSF component (Sparks et al., 2002). Images separated in wavelength can be scaled radially to fit and subtract away the PSF. Small spectral diversity results in radial self-subtraction, typically limiting the usefulness of narrow-band imaging and low-resolution integral field spectrographs with this method.

PDI exploits the fact that stellar light is highly unpolarized, while scattered

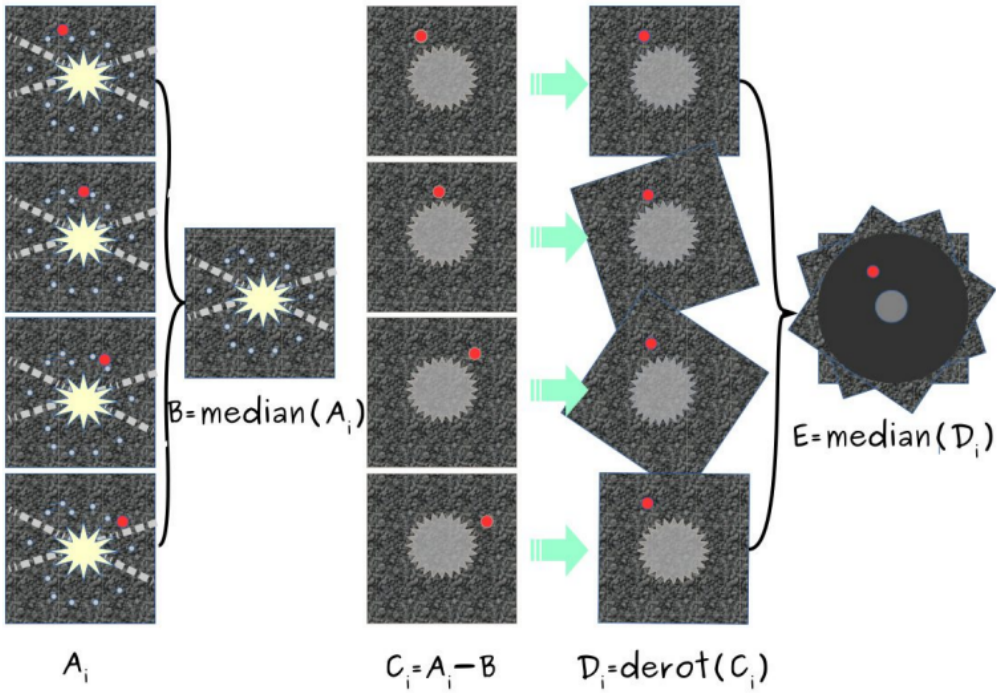

Figure 1.10: Schematic of Spectral Differential imaging. The median-subtracted, derotated, and stack images are then median combined to reveal off-axis light. The companion is marked as a red dot. From Carolo et al. (2016), Figure 1.

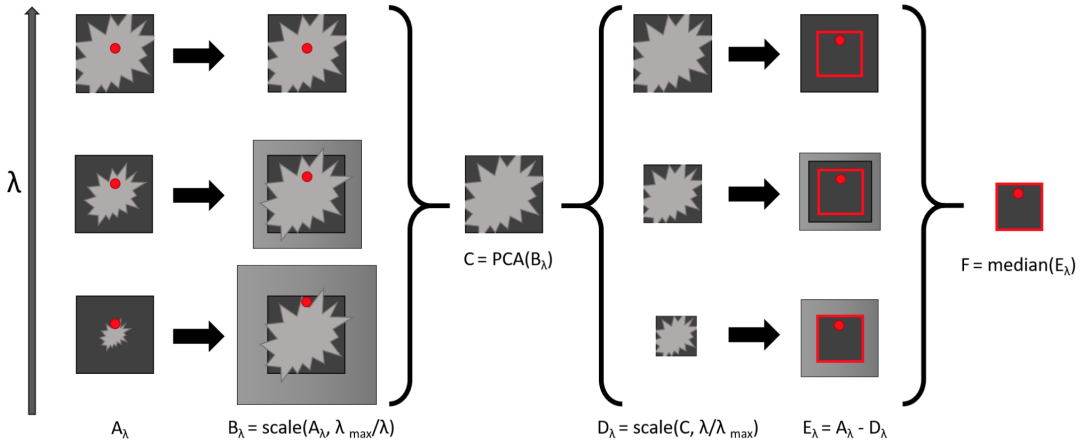

Figure 1.11: Schematic of Spectral Differential imaging. Images are scaled inversely proportional to their wavelength, stellar PSF model is then created using PCA analysis, stellar PSF model is rescaled for each wavelength channel proportional to its wavelength. The companion is marked as a red dot. From Kiefer et al. (2021), Figure 1.

light is linearly polarized. Circumstellar disks present large scattering surfaces and PDI has been widely used to discover them (de Boer et al., 2016; Avenhaus et al., 2018). Exoplanets scatter stellar light resulting in a significant degree of polarization, and thus PDI could be used to enhance the contrast. Moreover, it is expected that young gas giants also emit partially polarized light in the thermal infrared, yet the degree of polarization is low ($< 1\%$) (Stolker et al., 2017).

1.2 Integral Field Spectroscopy

Spectrophotometric information from an astrophysical source is inherently three-dimensional, which two spatial components and one component for the energy of the photon. The two-dimensional nature of detectors would otherwise preclude the capability of accessing one of the dimensions, wavelength in the case of an imager and a spatial dimension in the case of a slit spectrograph. Integral field spectrographs (IFS) instead reformat the bidimensional field into a pseudoslit which are then dispersed into spectra and detected at the focal plane. The resolving power $\mathrm{R} = \frac{\lambda}{\Delta\lambda}$ of a spectrograph describes the spectral scale $\Delta\lambda$ that can be resolved in a spectrom at wavelength λ.

Lenslet-based IFSs employ a microlens array as a spatial sampler (Figure 1.12). This enables retrieval of the three-dimensional information on two-dimensional detector without loss of sensitivity or spatial resolution. For exoplanet imaging,

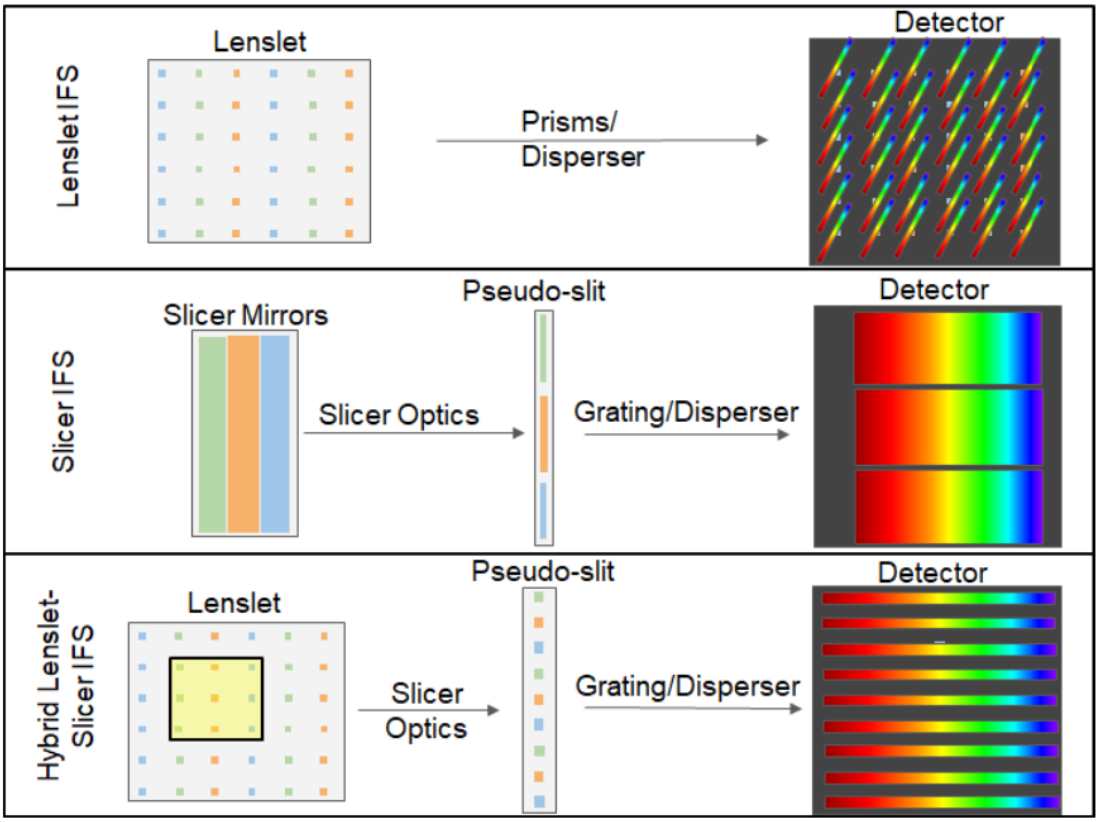

Figure 1.12: Schematic of lenslet, slicer and hybrid lenslet-slicer IFS. Image courtesy of R.D. Stelter.

lenslet-based IFSs are preferable to slicer IFSs because the lenslet array samples the field before any optical aberrations are imparted by downstream spectroscopic optics. For most IFSs, field-of-view is limited by the availability of large format detectors, rather than optics. For a given detector, lenslet-based IFSs trade between number of spaxels, spectrum length, and spectrum spacing.

Until this thesis, lenslet-based integral field spectroscopy has not ventured redward of K-band for high-contrast imaging, and the central theme of this thesis

is to demonstrate the effectiveness of integral field spectroscopy beyond K-band to the field of direct imaging and characterization. Specifically, the central focus of this thesis is in two thermal infrared integral field spectrographs, LBT/ALES (Skemer et al., 2015) and Keck/SCALES (Skemer et al., 2018c).

ALES

Arizona Lenslets for Exoplanet Spectroscopy (ALES; Skemer et al., 2015) is the world's first adaptive optics-fed thermal infrared IFS, and exists as a mode of LMIRcam (Skrutskie et al., 2010; Leisenring et al., 2012), the 1–5 μm adaptive optics (AO) imager for the Large Binocular Telescope Interferometer (LBTI; Hinz et al., 2008a, 2012, 2014).

Figure 1.13 contains schematic of the optical path for ALES after the Universal Beam Combiner, in which visible light is directed towards the LBTI wavefront sensors for adaptive optics correction (Bailey et al., 2014) performed with the deformable secondary mirror (Esposito et al., 2011), and wavefront-corrected, diffraction-limited, infrared light is directed into the cryogenic universal beam combiner (UBC) and then into the Nulling and Imaging Camera (NIC; Hinz et al., 2008b) where LMIRcam (Skrutskie et al., 2010; Leisenring et al., 2012) resides.

For early ALES operations, an 8× Keplerian magnifier, a silicon lenslet array with a pinhole grid to suppress diffraction, a blocking filter and disperser (direct-

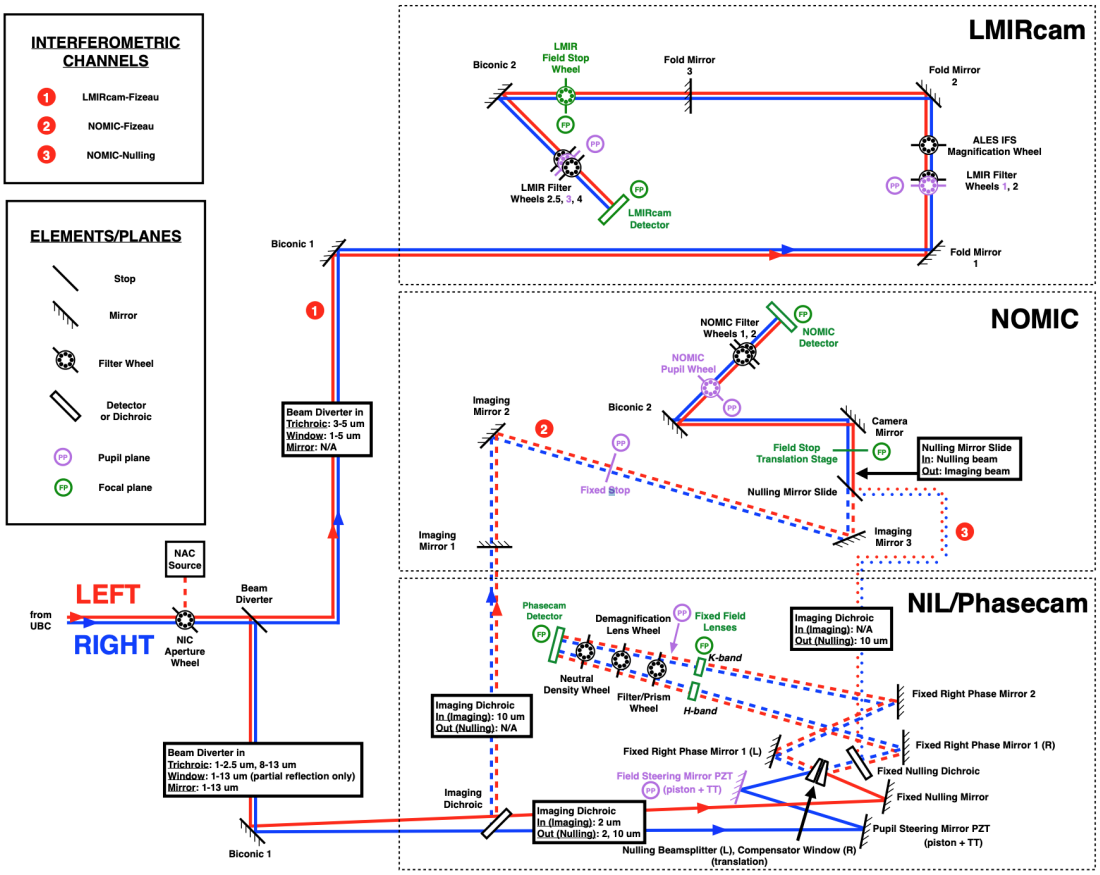

Figure 1.13: A schematic of the Nulling Infrared Camera (NIC) cryostat, which is downstream of the Universal Beam Combiner (UBC), as of Spring 2018. ALES is contained in LMIRcam in the top right. From Spalding et al. (2018a), Figure 3.

vision prism assembly) are introduced into the light path via LMIRcam filter wheels. The light incident on the spatial extent of each lenslet is focused through the diffraction-suppressing pinhole grid. Each lenslet sub-image is then dispersed by the direct-vision prism assembly. These dispersed sub-images are imaged onto a 5.2 micron-cutoff Teledyne HAWAII-2RG (H2RG; Beletic et al., 2008) as a grid of thermal infrared spectra.

In 2018, the ALES design was upgraded to address the lessons learned with the ALES prototype (Hinz et al., 2018). In particular, the upgrade included reflective magnifiers, aberration compensation in the lenslet array design, and higher dispersion prism dispersers.

The thesis work described in Chapter 2 enabled the thesis work in Chapter 3 (Briesemeister et al., 2019), Stone et al. (2020), Doelman et al. (2021), and Doelman et al. (2022), each including Z. Briesemeister as co-author (Figure 1.14). Stone et al. (2020) describes the first L-band (2.8-4.1 μm) spectroscopy of κ Andromedae b, a $\sim$20 M_J companion orbiting at 1" projected separation from its B9-type stellar host. Doelman et al. (2021) tests the novel vortex Apodizing Phase Plate (vAPP) coronagraph with ALES used to verify the transmissive properties of the optic. Doelman et al. (2022) presents vAPP coronagraphic integral field spectroscopy with ALES for HR 8799 cde.

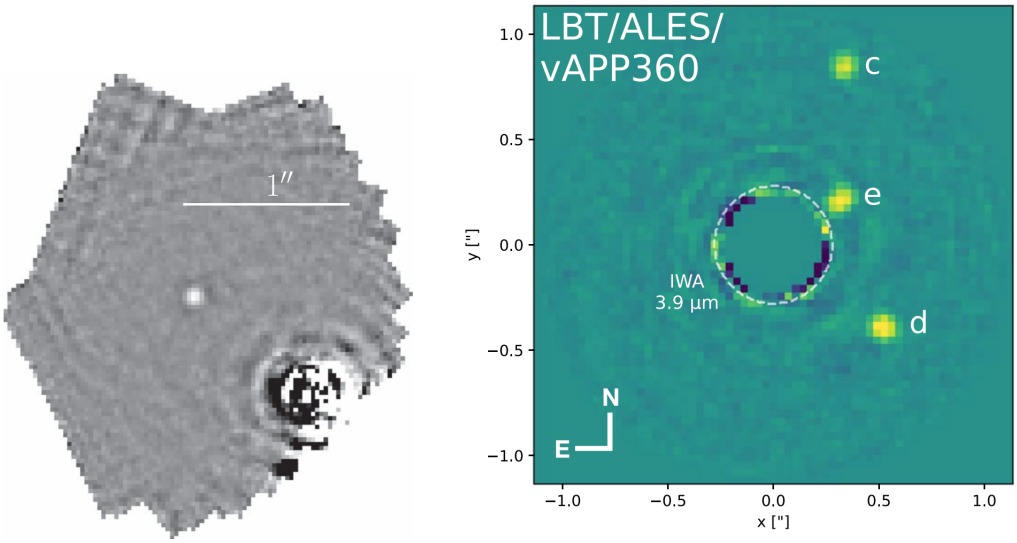

Figure 1.14: Left: ALES wavelength slice of κ Andromedae b. From Stone et al. (2020), Figure 1. Right: ALES wavelength slice of HR 8799 cde. From Doelman et al. (2022), Figure 4.

SCALES

While ALES bridges a technological and scientific gap, the dedicated instrument SCALES (Santa Cruz Array of Lenslets for Exoplanet Spectroscopy; Skemer et al., 2018c) vastly improves upon stability and sensitivity of ALES, providing 10-m class diffraction-limited thermal infrared low-/med-resolution spectra and imaging for the characterization of exoplanets. SCALES comprises a low-resolution integral field spectrograph and a medium resolution integral field spectrograph that share coronagraphic foreoptics transmissive from 2-5 μm, and a 1-5 μm imager.

The low-resolution IFS is lenslet-based, and the medium-resolution uses a hybrid lenslet-slicer (bottom, Figure 1.12). This hybrid takes advantage of the lenslet spatially sampling the field before any optical aberrations are imparted by downstream spectroscopic optics, while also reformatting the slit to enable higher dispersion. A complete description of the current optomechanics of SCALES is presented in Stelter et al. (2020), and recurring descriptions appear in Chapters 4 and 5 of this thesis, to avoid repetition here.

Figure 1.15 presents the SCALES optical system, which performs the following functions:

1. Relaying light from the AO system into the instrument.

2. Passing the optical beam through a cold stop placed at an image of the telescope+AO exit pupil to minimize infrared background from the observatory

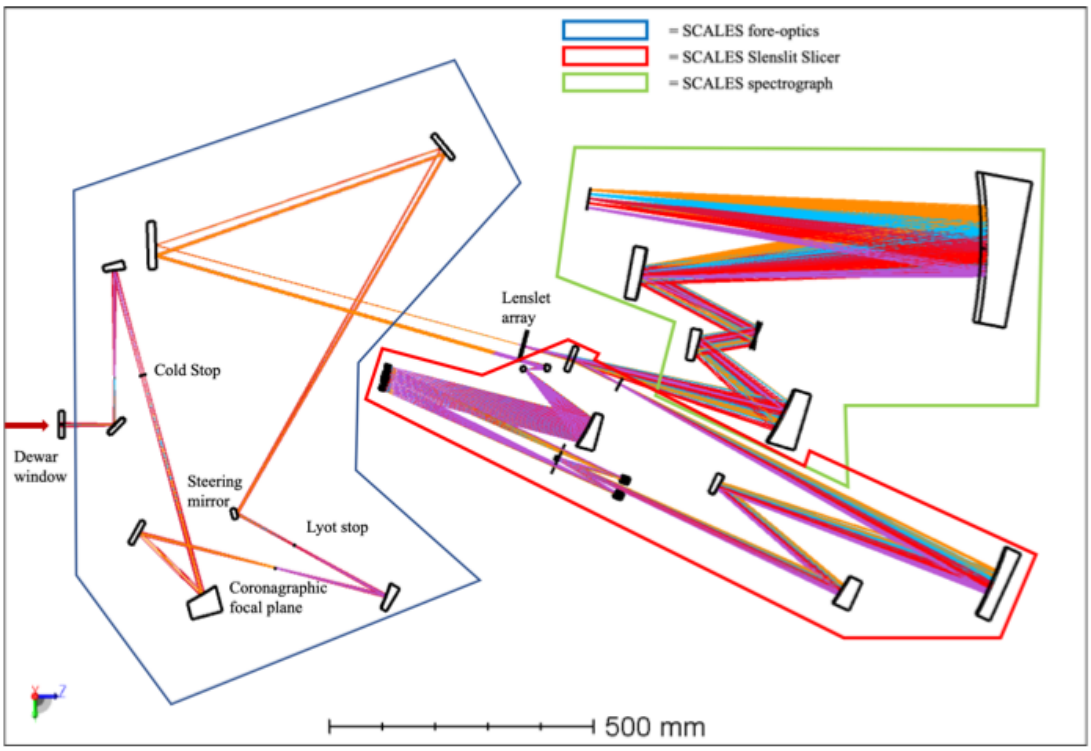

Figure 1.15: SCALES includes 3 major optical subsystems: a set of fore-optics feeding a lenslet array, a low-resolution lenslet-based integral field spectrograph, and a medium-resolution "slenslit" spectrograph that sends the lenslet light through an image slicer and back into the main spectrograph as a pseudoslit of lenslet spots.

and atmosphere.

3. Providing a collimated space for bandpass filters.

4. Producing a focal plane suitable for coronagraphic masking, which must not vignette the larger field of view of the imager upgrade. A linear mechanism holds several masks as well as a pupil imaging lens used for aligning the cold stop to the telescope.

5. Passing the optical beam through a pupil plane placed at an image of the cold stop for pupil apodization masking via a rotary mechanism. This mechanism also carries a fold mirror with which to feed the imaging system.

6. Steering the optical beam via a piezo tip-tilt mirror onto either the low-resolution or mid-resolution subarrays of the silicon lenslet array.

7. Reformat the beam for proper spatial sampling at the lenslet array.

8. Sampling the field of view with the lenslet array, the pitch of which determines the spatial sampling.

9. Passing the optical beam into the spectrograph, which has two pathways:

   (a) the slenslit which re-formats the optical beam from a regular grid of lenslet pupil images into a pseudoslit; it has three focal plane to focal plane relays.

(b) the low-resolution pathway continues on to the spectrograph.

10. Selecting which portion of the lenslet array to block via a linear stage, which also carries the slenslit return fold mirror.

11. Dispersing the light at a pupil plane via selectable prisms (low-resolution spectroscopy) or gratings (medium-resolution spectroscopy).

12. Passing the light through order-selecting infrared filters appropriate to the desired scientific bandpass.

13. Finally, recording the spectrum (or lenslet images) onto an infrared detector array.

The thesis work in Chapter 4 comprises a simulation of each of these functions. These simulations are used in Chapter 5 to measure tolerances of the instrument set by fiducial science cases (Figure 1.16) using information content theory.

1.3 This Thesis

If astronomers want to fully understand and characterize exoplanets, astronomical observations must overcome extreme contrasts and reliably measure the intensity over large ranges of the electromagnetic spectrum at high spatial resolution. The work presented in this thesis aims to contribute to this endeavour by applying and developing new ways to perform and analyse exoplanet observations.

Target Type	SCALES Modes			Anticipated Science Outcomes
Exoplanets	2.0-5.2 μm (L)	2.9-4.2 μm (L)	4.5-5.2 μm (L)	Measure planet luminosity, pressure-temperature profile, molecular abundances, metallicity
		2.9-4.2 μm (M)	4.5-5.2 μm (M)	
Protoplanets	2.0-5.2 μm (L)	2.9-4.2 μm (L)	4.5-5.2 μm (L)	Constrain IR slope, Hydrogen line fluxes, disentangle disk and protoplanet signals
		2.9-4.2 μm (M)	4.5-5.2 μm (M)	
Protoplanetary Disks	3.1-3.5 μm (L)			Constrain complex disk morphology as a function of wavelength, map H_2O and PAH grains
Solar System	2.0-5.2 μm (L)	2.9-4.2 μm (L)	4.5-5.2 μm (L)	Constrain volcano temperatures, measure IR fluxes, extents, and variability of clouds
Supernova Remnants	4.5-5.2 μm (M)			Map dust distribution and content
Active Galactic Nuclei	3.1-3.5 μm (L)			Trace hot dust and small grains, map PAH emission

Figure 1.16: Table of fiducial science cases with SCALES. Image courtesy of S. Sallum.

In Chapter 2, we explore the methods needed to treat the data produced by ALES. Before post-processing techniques can work, it is necessary to extract a data cube from each spectrograph focal plane. The spectrum produced for each spatial element is coarsely-sampled, and confined to a tiny fraction of the detector area, so that even small distortions in the geometric pattern of the focal plane will corrupt the data extraction unless those effects are accounted for.

In Chapter 3, we present ALES L-band integral field spectroscopy of the brown dwarf binary HD 130948BC. The HD 130948 system is a hierarchical triple system, in which the G2V primary is joined by two co-orbiting brown dwarfs.

In Chapter 4, we present end-to-end simulations of SCALES, and place it in context with detection and characterization of a wide variety of exoplanets, including exoplanets detected through long-baseline astrometry, radial-velocity

planets on wide orbits, and accreting protoplanets in nearby star-forming regions. The simulation goal is to generate high-fidelity mock data to assess the scientific capabilities of the SCALES instrument at current and future design stages.

In Chapter 5, we quantify optomechanical tolerance and detector electronic requirements set by the fiducial science cases for SCALES using information content analysis, and test the consequences of updates to the design of the instrument on meeting these requirements.

In Chapter 6, we place SCALES in context with the broader direct imaging field around 2025, discuss the synergy between astrometric detection of exoplanets and high-contrast imaging, and discuss the infrared interferometric imaging with SCALES.

Chapter 2

ALES Data Reduction Pipeline

Adapted from

MEAD: Data Reduction Pipeline for ALES Integral Field Spectrograph and LBTI Thermal Infrared Calibration Unit

Z. W. Briesemeister, A. I. J. Skemer, J. M. Stone, R. D. Stelter, P. Hinz, J. Leisenring, M. F. Skrutskie, C. E. Woodward, and T. S. Barman

Proceedings of the SPIE, Volume 10702, id. 107022Q 12 pp. (2018)

DOI: 10.1117/12.2312859,

Abstract

We present the data reduction pipeline, `MEAD`, for Arizona Lenslets for Exoplanet Spectroscopy (ALES), the first thermal infrared integral field spectrograph designed for high-contrast imaging. ALES is an upgrade of LMIRCam, the $1-5\,\mu$m imaging camera for the Large Binocular Telescope, capable of observing astronomical objects in the thermal infrared ($3-5\,\mu$m) to produce simultaneous spatial and spectral data cubes. The pipeline is currently designed to perform L-band ($2.8-4.2\,\mu$m) data cube reconstruction, relying on methods used extensively by current near-infrared integral field spectrographs. ALES data cube reconstruction on each spectra uses an optimal extraction method. The calibration unit comprises a thermal infrared source, a monochromator and an optical diffuser designed to inject specific wavelengths of light into LBTI to evenly illuminate the pupil plane and ALES lenslet array with monochromatic light. Not only does the calibration unit facilitate wavelength calibration for ALES and LBTI, but it also provides images of monochromatic point spread functions (PSFs). A linear combination of these monochromatic PSFs can be optimized to fit each spectrum in the least-square sense via χ^2 fitting.

2.1 Introduction

Arizona Lenslets for Exoplanet Spectroscopy (ALES; Skemer et al., 2015) is a project designed to extend the functionality of the Large Binocular Telescope Interferometer's (LBTI; Hinz et al., 2008b,a, 2012, 2014) $1-5\,\mu$m imager LMIRCam (Skrutskie et al., 2010; Leisenring et al., 2012). ALES is the first integral field spectrograph (IFS) capable of high-contrast imaging in the thermal infrared. A current scientific goal utilizing ALES on a single aperture of LBT is to deliver low-resolution LM-band spectra of young, gas giant exoplanets and substellar companions in order to supplement existing near-infrared JHK spectra for a broader spectroscopic characterization of these bodies. This goal can be accomplished by exploiting the unique properties of IFS data cubes, which comprise photometrically accurate stacks of simultaneous narrowband images spanning multiple wavelength channels. The spatial and spectral information within the IFS cubes enables unambiguous separation of the light from substellar companions and their host star.

The success of near-infrared lenslet-based IFSs has been due in large part to the development of robust techniques for automating the construction of wavelength-calibrated spectral data cubes from the thousands of closely-packed spectra in raw frames (e.g. GPI, (Macintosh et al., 2008; Perrin et al., 2014); SPHERE, (Claudi et al., 2008; Pavlov et al., 2008); Project 1640, (Hinkley et al., 2011; Zimmerman

et al., 2011); CHARIS, (McElwain et al., 2012; Brandt et al., 2017); OSIRIS, (Larkin et al., 2006)). These pipelines are critical for the homogenization of data products and the accessibility for other observers.

The Methods for Extracting ALES Data (`MEAD`) package is the Python-language data reduction pipeline for ALES that has leveraged the insights gained during the operations of the near-infrared IFSs in order to orchestrate the construction of ALES data cubes. After a brief overview of the instrument, this paper begins by presenting `MEAD` in a linear fashion, following a recipe with which most observations will be reduced. Then the paper focuses on the thermal infrared calibration unit for LBTI and how the unit will affect ALES operations. Section 2.4 summarizes basic processing of raw data frames to remove detector artifacts. Section 2.5 addresses the extent and characterization of flexure in the instrument, as well as the calibration process. Section 2.6 briefly states how the cubes are reconstructed. Section 2.7 cover the thermal infrared calibration unit for LBTI. We finish by discussing the immediate future for ALES and `MEAD` in Section 2.8.

2.2 Instrument Overview

ALES is a low resolution, thermal infrared, lenslet-based integral field spectrograph inside LBTI/LMIRCam. Unlike the near-infrared analogues, LMIRCam is not solely dedicated to science performed with ALES; the ALES optics are

set inside filter wheels in order to allow LMIRCam operations to remain undisturbed. ALES itself comprises an 8× Keplerian magnifier, a silicon lenslet array, a diffraction suppressing pinhole grid, direct-vision prism and blocking filter inside LBTI/LMIRCam.

LBTI is situated at the combined bent Gregorian focus of the LBT's twin 8.4 meter mirrors, each equipped with deformable secondary mirrors (Esposito et al., 2011), LBTI adaptive optics (AO) systems (Bailey et al., 2014), and flat tertiaries that redirect wavefront-corrected, diffraction-limited, infrared light into the cryogenic universal beam combiner (UBC). The initial mode of ALES was designed to operate behind a single aperture of LBT, so the UBC redirects the light without any pathlength correction into the science instrument dewar (Nulling Infrared Camera, NIC) and the cryogenic science camera, LMIRcam.

At the focal plane of each lenslet, an image of the exit sub-pupil will form, comprising of all the light from the image incident on the spatial extent of the lenslet. The subpupils are then dispersed without spatial or spectral overlap, forming images of dispersed subpupils on LMIRCam's Teledyne HAWAII-2RG (H2RG; Beletic et al., 2008). Each subpupil becomes a spatial pixel element (spaxel) with an associated spectrum in the final spectral data cubes. At the focal plane, the light is dispersed at a fiducial angle of $\theta = tan^{-1}\frac{1}{2} \approx 26.56°$ with respect to the detector columns. For its inital mode for which this paper is most

relevant, ALES observes L-band ($2.8 - 4.2\,\mu$m) spectral data cubes. In detector coordinates, the L-band spectra are expected extend 35.6 pixels in the spectral direction and 4-5 pixels FWHM in the spatial direction (Skemer et al., 2015).

ALES first light, design, data processing, operations, and upcoming upgrades are discussed in the following:

- First Light with ALES: A 2-5 Micron Adaptive Optics Integral Field Spectrograph for the LBT (Skemer et al. 2015 (Skemer et al., 2015))
- Design of ALES: a broad wavelength integral field unit for LBTI/LMIRCam (Hinz et al., 2018)
- MEAD: Data Reduction Pipeline for ALES Integral Field Spectrograph and LBTI Thermal Infrared Calibration Unit (This work)
- On-sky operations with the ALES integral field spectrograph (Stone et al., 2018b)
- ALES: Overview and Upgrades (Stone et al., 2018b)

Looking towards the future of ALES observations, we also encourage readers to consult (Spalding et al., 2018b) and (Leisenring et al., 2014) for a discussion of Fizeau interferometry using dual aperture mode of LBT with LBTI. This will allow ALES to observe at the diffraction limit with the entire 23.4m effective aperture of the LBT.

2.3 Data Reduction Overview

While ALES has unique science capabilities, ALES science can only be as good as its data reduction pipeline. As operations have matured, `MEAD` has been developed to approach the problem of extracting the science data from raw frames with the goal of user-friendliness and flexibility. While the main focus of the pipeline is to produce photometrically accurate and calibrated data cubes for scientific analysis, we also require quick reductions to guide ALES operations. This will also include guiding on the occulted point spread function from one of LMIRCam's coronagraphs, following its recent alignment with ALES optics.

Ultimately, `MEAD` will exist as a software package to cover all stages of data reduction and post-processing for ALES. However, the complete automation and the integration with LBTI/LMIRCam software remains to be implemented. `MEAD` has endured rapid development in order to address the expected updates to ALES for 2018B (Skemer et al., 2018) and will soon be critical to controlling ALES operations.

The full science data reduction is organized into five main components as follows:

Data Parser – The data parsing tool is designed to reconstruct the progression of an observation run from metadata and organize a data set into their associated sequences. This can be performed naïvely with just the FITS header

information in each science exposure. However, ancillary information regarding the pointing pattern and well-documented observing logs are necessary to intelligently organize the data and exclude bad frames, respectively. Changes to the pointing pattern should be updated manually in the configuration files.

Basic Processing – User-discretion methods for bias subtraction, dark subtraction, pixel flat-fielding, frame combination, bad pixel identification and removal, linearity correction, and microphonic noise suppression. The merits and downsides of certain corrections are addressed in Section 2.4.

Focal Plane Geometry Calculation – ALES is a filter wheel instrument, so the lenslet array, dispersing element (prism) and detector are not absolutely static with respect to one another; mechanical flexure that distorts the focal plane geometry manifests with strong field dependence. In order to extract each spectrum as homogeneously as possible, this stage develops of a piecewise focal plane model, in which each spectrum is calibrated independently. Every light-sensitive pixel is then mapped to a weight in a wavelength-calibrated data cube. See Section 2.5 for further explanation.

Cube Construction – `MEAD` orchestrates the construction of data cubes. For optimal or aperture extraction methods, the focal plane solution is used to map every light-sensitive pixel to a weight in a data cube, and the flux extraction method defines the magnitude of these weights. See Section 2.6 for further expla-

nation. For the χ^2 extraction method described in Section 2.8.1, cubes can be built from the linear combination of position- and wavelength-dependent monochromatic point spread functions that fit each spectrum.

Post-Processing – For high-contrast imaging, PSF subtraction using Angular Differential Imaging (KLIP (Soummer et al., 2012)) is currently implemented. We will expand to other PSF subtraction methods when relevant. ALES-specific wrappers for the Vortex Image Processing (VIP (Gonzalez et al., 2017)) package implementation of other post-processing methods are also available.

Quicklook reductions require far less robust calculation, especially because the coronagraph can effectively be guided with any individual wavelength channel image or even the wavelength-collapsed cube. The relative aggressiveness of reduction can be controlled manually, but are also associated with longer runtime. The optimization of realtime reduction and post-processing remains an open investigation.

2.4 Basic Processing

The science detector for ALES is the 2048×2048 pixel H2RG of LMIRCam. Early observations were performed with FORCAST (Leisenring et al., 2010) readout electronics, which limited the detector readout to a 1024×1024 pixel sub-array. This sub-array has 50×50 spatial pixel elements (spaxels) with a field of view of

1.3"×1.3". The readout electronics have since been replaced with Teledyne SIDECAR ASIC (Loose et al., 2005) electronics to read out the entire detector. This section will give an overview of corrections for detector artifacts performed during a standard reduction.

2.4.1 Detector Artifacts

2.4.1.1 Residual Channel Bias

Each of the 64-pixel-wide channels has its own analog-to-digital converter set an unique bias levels. This poses a problem for spaxels that overlap two readout channels, particularly because the offset would propagate to the reduced cube as a striping pattern that affects different spaxels at different wavelengths.

The residual channel bias offsets are corrected using the median of each channel's reference pixels, which are then subtracted off from their respective channels. Residual channel bias is not observed to be constant or repeatable in successive frames, so this correction must occur after dark- or thermal background-subtraction.

2.4.1.2 Flatfielding

Integral field spectrographs have two types of flatfielding: pixel and lenslet flatfields. The traditional pixel flatfielding adjusts for variable detector gain, while

lenslet flats are a characterization of variable lenslet throughput as a function of wavelength. Pixel flatfields are a correction in detector coordinates, while lenslet flatfields are a correction in spaxel coordinates. Lenslet flatfields will be discussed in Section 2.6.

Without intervention, the pipeline defaults to building and using a pixel flatfield if the data parser flags such data to exist. This functionality can be toggled in the configuration file. The thermal background (thermal telescope and sky emission) is imaged without ALES optics on LMIRCam, which are then dark-subtracted, median-combined, and divided by the mode to create a master flat. Pixels with a correction greater than 1.5 or less than .5 are flagged to be bad pixels.

2.4.1.3 Dark Subtraction

Median dark frames are subtracted from thermal background frames for cube reconstruction of the lenslet flatfield (See Section 2.6). Narrowband calibration data must also be dark-subtracted in order to remove detector artifacts. In both of these cases, the residual channel bias correction is necessary.

2.4.1.4 Bad Pixel Correction

`MEAD` comes with a reference bad pixel mask, which can be updated, remade, or completely disregarded. The reference bad pixel mask was made from LMIRCam

data from 2016 with the same method in which the pipeline would remake the mask upon request. We calculated the standard deviation of a stack of dedicated dark frames. Since the distribution was asymmetric, we chose to flag the top 2% and bottom 1% as bad pixels. If pixels were flagged during pixel flatfield creation, they are also flagged here. Bad pixels are corrected by replacing them with the average of the nearest four good neighboring pixels. Cosmic rays are not a significant noise source, as the H2RG is substrate-removed. Existing cosmic rays are nominally removed when median combining frames.

2.4.1.5 Linearity

`MEAD` also comes with reference linearity correction, which can be used, remade or ignored. Ten dark-subtracted flatfield frames are imaged at each exposure time possible between .03 and 2.33 seconds. For a uniform correction across the entire array, a linear fit to the linear part of the medians of the ten frames for each exposure time is used to define the linearity correction. For the field-dependent correction, a linear fit to every pixel in the time-series frames defines the linearity correction. The correction is set to only apply near where the fit begins to diverge .1% from the observed linearity data.

2.4.1.6 Microphonic Noise Suppression

Microphonic noise induced by vibrations from an undetermined source manifest as horizontal sinusoidal patterns on the detector. Although microphonic noise is only observed for short exposure times, the thermal background limits going to longer exposure times. We remove the microphonics artifact in a similar fashion to GPI by diminishing the intensity of frequencies corresponding to the noise in the image proportionately to the dot product of the image with a noise model built from short exposure time dark frames (Maire et al., 2010; Perrin et al., 2014).

2.5 Focal Plane Geometry

The initial mode of ALES is designed to deliver to the focal plane 2,500 equally-spaced $2.8 - 4.2\,\mu$m spectra, each spanning 35.6 pixels in the dispersion direction at an angle $\theta = tan^{-1}\frac{1}{2} \approx 26.56°$. Mechanical flexure distorts the geometry of the spectrograph focal plane, changing the position and dispersion angle of science spectra with respect to calibration spectra. The deviation from the fiducial dispersion angle, the shift along the dispersion axis and the shift perpendicular to the dispersion axis are the three parameters necessary to describe and calibrate the distortion from flexure. These three parameters for each spectrum also have field dependence (Figure 2.2). This requires a joint characterization of these deviations in order to have calibrate the spectra in the cube.

The focal plane geometry differed on a night-to-night basis by almost 3 pixels because the alignment of the ALES optics within filter wheels is not perfectly reproduced on this timescale (Figure 2.1). Instead of favoring some smooth distortion to calibration data, we prefer to simply take a complete set of calibration data for every night.

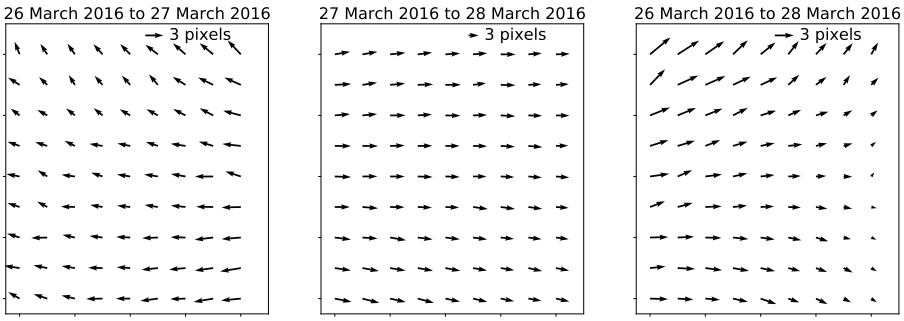

Figure 2.1: The evolution of the spectrograph focal plane geometry over a three night period. Each arrow represents the median deviation between the spaxel position of two nights in a 5×5 spaxel region. The spaxel position is defined by the position of the 3.950 μm narrowband filter spot associated with the spaxel.

2.5.1 Crosstalk

ALES is designed such that the separation of the spectra is maximized, which minimizes the crosstalk between adjacent spaxels. However, astigmatism induced by the second biconic mirror inside LMIRCam manifest in ALES raw data as a

decay in the sharpness of spatial profiles near the edge of the detector, and these spectra have nontrivial crosstalk with one another. As part of ALES upgrades in 2018, the lenslet array is being replaced with a lenslet array that reverses the astigmatism induced by the mirror and should successfully suppress the crosstalk effect near the edges. Apart from using more appropriate weights in the optimal extraction (Section 2.6), we will wait for the new lenslet array upgrade prior to developing a more robust correction.

The χ^2 extraction method described in Section 2.8.1 is ideal for addressing crosstalk, as the monochromatic PSFs would also experience the same optical distortions that cause the spatial and spectral resolution to decay across the field. The spectra are first fit naïvely, and the resulting model 2D spectra are subtracted from the data. The individual model spectra overlap with neighboring spectra, resulting in negative residuals. An iterative approach to minimizing the magnitude of the negative residuals is then applied to remove the effects of crosstalk.

2.5.2 Isolating the Spectra

ALES has access to four narrowband filters with central wavelengths 2.925, 3.375, 3.555, 3.950 μm for L-band calibrations. ALES observes the thermal background with the narrowband filters. Since the thermal background is almost two orders of magnitude brighter in the red end of L-band compared to the blue end,

the 3.950 μm is the brightest narrowband filter imaged with ALES. Each spectrum is coarsely located using the pixel location of the peak of the associated 3.950 μm narrowband filter data. A 60×40 pixel rectangular slice is defined around each spectrum, with enough room such than the extraction region for the spectrum would remain populated with data given shifts parallel and perpendicular to the dispersion axis. The small rectangular slice reduces computational cost of interpolation.

The 3.950 μm narrowband filter data peak is located by centroiding, which would, in principle, give an origin with which to rotate the extraction region. However, for calibration data taken at a different gravity vector than the target pointings, the narrowband filter data might not be coincident with the science data.

2.5.3 Solution for Offsets

We have since adjusted the observing pattern for ALES to include calibrations taken without slewing the telescope away from the science target. Under the same gravity vector, the perpendicular and parallel shifts with respect to the dispersion axis are minimized to subpixel magnitudes. However, calculating deviations from the fiducial dispersion angle is still required for the rectification process.

The deviation from the fiducial dispersion angle, along with perpendicular and

parallel shifts along the dispersion axis from the calibration data become three offset parameters for every spectrum. The flexure between target pointings and sky pointings were empirically determined to be negligible under normal observing conditions, so the even illumination of the thermal background during sky pointings is ideal for calibration.

The sky spectrum in L-band, modulated by filter transmission, has features that can be used to calculate parallel shifts. Cross-correlation between the ALES sky spectral cubes with an ALES-resolution model spectra of the thermal background allows for wavelength shifts to be calibrated. Perpendicular shifts are derived by differencing the centroids of the spatial profiles of the sky spectra and all narrowband filter data.

The deviation from the dispersion angle is calculated using a Radon transform, performed via a grid search of rotation angles to populate a sinogram with the spatial profiles of rotated, mean-subtracted 2D spectra. The dispersion angle can be identified using one of two methods: the angle that minimizes the root-mean-square of the mean-subtracted average spatial profile or the angle that minimizes the absolute magnitude of the slope of the line of best fit of the centroids of the spatial profiles. The resulting field dependent deviations are then Gaussian smoothed with FWHM of one spaxel (Figure 2.2).

The wavelength solution is built from fitting an empirical dispersion relation

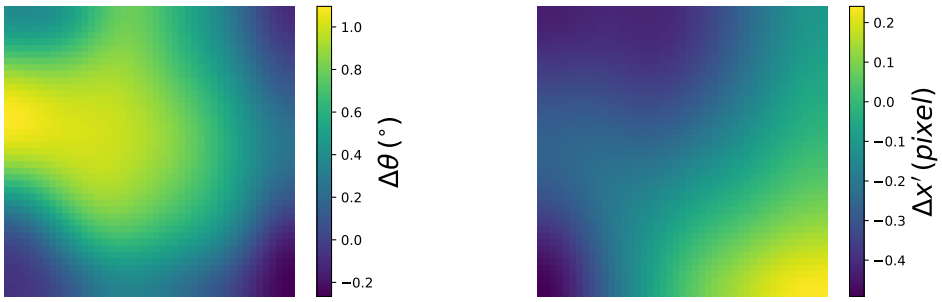

Figure 2.2: Left: The field dependent deviation of the dispersion angle from $\theta = tan^{-1}\frac{1}{2}$. The average angle excess on 27 March 2016 is 0.55°. Right: The field dependent perpendicular shift from the dispersion axis. The average spatial offset of calibration data from science data on 27 March 2016 was -0.17 pixels. Not shown: the field dependent parallel shift along the dispersion axis of the calibration data from the science data. The magnitude was determined to be consistent with no shift.

to the peaks of the narrowband filter data. By default, the pipeline chooses the wavelength solution of the central spaxel to be the wavelength solution for the final data cube. The solver works by updating the coordinates for an affine transformation; after all the calibration, only one interpolation per spectrum will be necessary for both flux extraction and wavelength calibrate on a common wavelength grid such that the data cube can be easily visualized and manipulated. The single interpolation minimizes distortion of the data and homogenizes the cube construction across all spectra.

The pipeline can build as many calibration data files as there are thermal background realizations. However, there is not significant flexure between pointing patterns, and it is enough to calibrate on one or two thermal background observations for a whole night.

2.6 Cube Construction

With the data products from the focal plane geometry calculation, `MEAD` constructs the data cubes from the raw frames using the same coordinate transformations derived during the calibration step. This cube construction, as well as the calibration step, act on subsections of the entire frame completely independent from one another. This makes these steps ideal for parallelization, and they have been implemented as such. The user can also toggle the parallelization and number of processors in the configuration file.

The current preferred method for performing spectral extraction for cube construction is optimal extraction (Horne, 1986). This method combines empirical information about the spatial profiles and errors to provide informed weights for a weighted-average. The field dependent astigmatism causes spatial profiles to vary across an ALES field that would otherwise be ignored under a unity-weighted scheme, and optimal extraction is not computationally more expensive. The optimal extraction method uses the empirical spatial profiles derived from the thermal

background frames.

2.6.1 Data Products

The analyzable data products include science target data cubes, spectrophotometric calibration data cubes, astrometric calibration data cubes, lenslet flatfields and the wavelength solution for the data cubes. All data cubes are also accompanied by their variance data cube, which have been propagated from the variance image of raw frames. Slices of an example science target data cube can be seen in Figure 2.3.

The lenslet flatfield is built from constructing cubes from dark-subtracted thermal background frames that are then normalized at each wavelength channel by the median of the slice. The lenslet flatfield is then a data cube with each wavelength channel being the field dependent throughput of each lenslet. Typical values in the lenslet flatfield are between .95 and 1.05, with extrema at .90 and 1.10.

For high-contrast imaging datasets, these data products are prepared for post-processing. `MEAD` contains limited post-processing tools in its current state, namely Karhunen-Loeve Image Projection (KLIP (Soummer et al., 2012)) for Angular Differential Imaging. The science goals of ALES are currently guiding the implementation of more post-processing tools. `MEAD` also contains ALES-specific wrappers

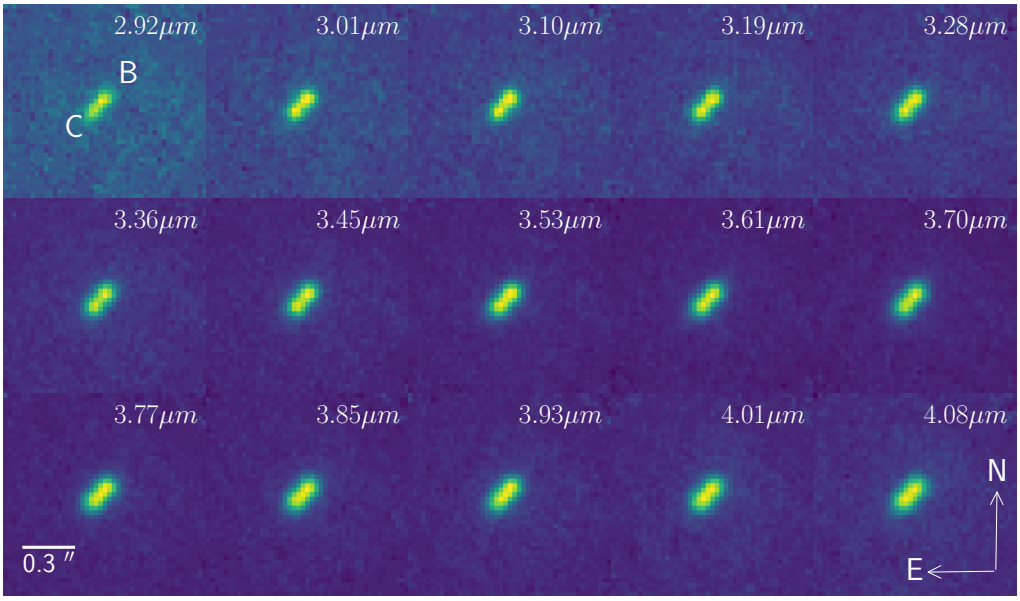

Figure 2.3: An example of an ALES data cube, with 15 representative wavelength slices of the data cube for HD 130948 BC, a L4+L4 benchmark brown dwarf binary orbiting as Sun-like primary star in a hierarchical system. The pair of brown dwarfs are separated by .104", and are resolved in L-band with ALES.

for the Vortex Image Processing (VIP (Gonzalez et al., 2017)) package implementation of Locally optimized Combination of Images (LOCI (Lafrenière et al., 2007)) and LLSG (Gomez Gonzalez et al., 2016), but has not been extensively tested with all of the available functionality of the package.

2.7 Thermal Infrared Calibration Unit

Robust calibration in the thermal infrared is tricky because the highly-variable and bright thermal background. Internally, LMIRCam contains the four narrowband filters, which are used to image narrowband flats using their transmission of the thermal background. This is sufficient for constraining the wavelength solution for the optimal extraction method, but the four narrowband filters do not provide a full coverage of monochromatic PSFs necessary to perform the χ^2 extraction. External calibration sources would need to produce monochromatic flats that are both bright and stable with respect to the thermal background. The calibration unit also needs to be tunable in order to image the position- and wavelength-dependent monochromatic PSFs.

A new calibration method has been designed for LMIRCam/ALES with the goal to select wavelengths from a blackbody continuum to image monochromatic light on the detector. The calibration unit (Figure 2.4) comprises a thermal infrared source (a), a Czerny-Turner monochromator (b) and an optical diffuser (e).

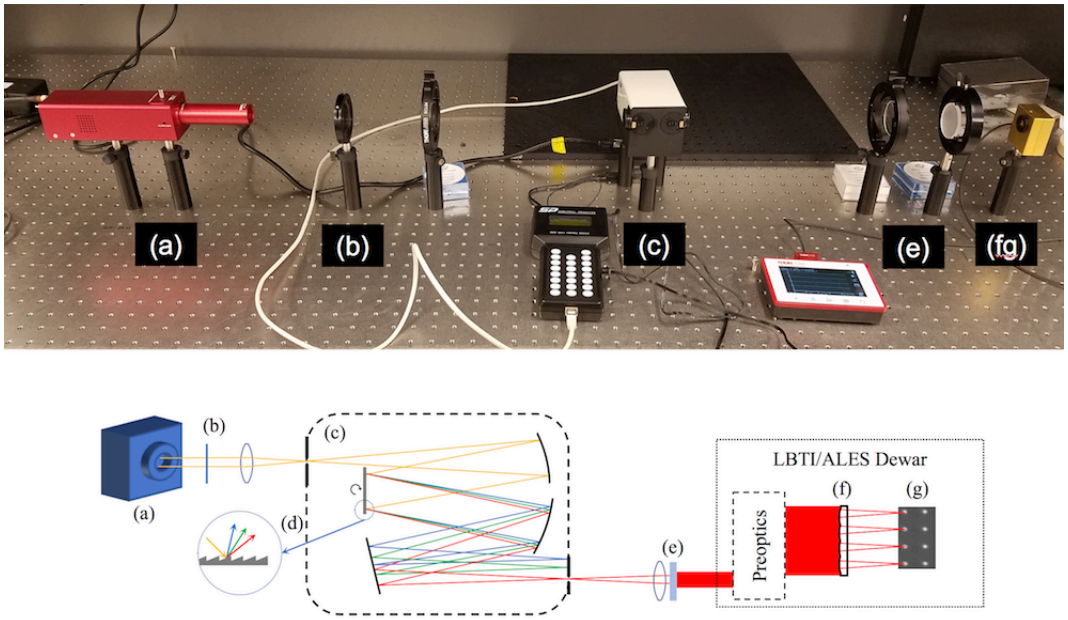

Figure 2.4: Schematic and Lab image of the thermal infrared calibration unit for LBTI. The unit comprises the thermal infrared source (a), shutters and baffling (b; not depicted in image), a Czerny-Turner monochromator (cd) and the optical diffuser (e). An integrating sphere (fg) substitutes for LBTI in the lab.

The light from the thermal infrared source is focused onto the entrance slit of the monochromator, which has an rotatable grating (d) that disperses the light onto an exit slit. A specific wavelength of light is selected by rotating the grating, which translates the spectrum across the exit slit. This monochromatic light passes through an optical diffuser in order to evenly illuminate the pupil plane of ALES (fg).

The design of the thermal infrared calibration unit (Figure 2.4) is distinct from

near-infrared implementations for imaging monochromatic PSFs because common optical materials are opaque at these wavelengths and thermal infrared photons increase the temperature of elements in the unit. Optics closer to the thermal infrared source are more likely to be heated and contribute to the background, requiring calibrations to be taken at steady state. This steady state may not be reachable in the time allotted for calibrations, requiring background frames to be taken more often.

The monochromator has two gratings designed for 400-1500 nm and 1500-6000 nm, respectively. A HeNe laser (632.8 nm) was used to confirm the wavelength calibration and design specifications of the first grating. However, there remains no independent confirmation of the wavelength calibration of the relevant 1500-6000 nm grating, but manufacturer supplied data suggests good conformity. Thermal infrared sources do not stop emitting thermal infrared photons when they are turned off for obtaining background frames in between calibrations frames; a system of shutters is necessary to block the light from entering LBTI as well as block the heat from previous shutters that will begin to glow from the incident radiation. Baffling and the shutter system (b) is not accurately represented in the lab setup in Figure 2.4 in order to show the rest of the unit.

It would be particularly difficult to illuminate the dome or a screen with monochromatic thermal photons in order to fill the primary with monochromatic

light, so this calibration light will not be experiencing aberration from the three warm optics associated with each aperture. Instead, the calibration unit light will be incident on the entrance window of LBTI/NIC, and will still experience the astigmatism caused by the biconic mirror inside LMIRCam. It is key to determine the frequency of which a full coverage of monochromatic PSF data would need to be taken.

2.8 Future Work

The data reduction pipeline is also accommodating the multitude of upgrades to the instrument coming in 2018B. Apart from the thermal infrared calibration unit, the extent of these upgrades are described in (Skemer et al., 2018a).

2.8.1 Chi Square Extraction

The least-square inversion flux (χ^2) extraction method Brandt et al. (2017); Draper et al. (2014) performs spectral deconvolution by proposing a linear combination of empirical monochromatic PSFs to fit each spectrum in the least-square sense. This method would be particularly powerful to implement for ALES because the field dependent astigmatism distorts the monochromatic PSFs in the same way it distorts the spectra.

The method is advantageous because it circumvents artifacts associated with

the optimal extraction method: it performs no interpolations that would induce spectral correlation and it uncouples the spectrum from systematic noise. It trivially fits the undispersed background, and avoids final interpolation onto a common wavelength grid, which is a source of spectral correlation induced by current methods of flux extraction.

The thermal calibration unit facilitates imaging a full coverage of the position- and wavelength-dependent monochromatic point spread functions that would make the χ^2 extraction method possible for ALES. The implementation currently exists using singular value decomposition in `MEAD` and has been tested on simulated data, but extensive testing with real data from the calibration unit will be required before ALES operations use this method of extraction.

2.8.2 Coronagraph Alignment and Guiding

ALES operations have as of yet not included the use of a coronagraph, which will eventually become key to probing higher contrasts. ALES is aligned with LBTI's L' annular groove phase mask coronagraph Defrère et al. (2014) inside LMIRCam's filter wheel, but guiding on an obstructed PSF from raw integral field spectrograph frames presents an obstacle that will need to be overcome for 2018B. The extent at which the full data reduction procedure can be pared down in favor of expediency and accuracy for guiding the coronagraph will need to be

tested, largely dependent on the magnitude of flexure. This quick-look version of data reduction would forgo rigorous calibration, and simply takes in narrowband filter data or uses an old focal plane model. This remains to be integrated with LBTI/LMIRCam software.

Acknowledgments

The LBT is an international collaboration among institutions in the United States, Italy and Germany. LBT Corporation partners are: The University of Arizona on behalf of the Arizona university system; Istituto Nazionale di Astrofisica, Italy; LBT Beteiligungsgesellschaft, Germany, representing the Max-Planck Society, the Astrophysical Institute Potsdam, and Heidelberg University; The Ohio State University, and The Research Corporation, on behalf of The University of Notre Dame, University of Minnesota and University of Virginia. This paper is based on work funded by NSF Grants 1608834 and 1614320.

Chapter 3

ALES *L*-band Spectroscopy of HD 130948BC

Adapted from

High Spatial Resolution Thermal Infrared Spectroscopy with ALES: Resolved Spectra of the Benchmark Brown Dwarf Binary HD 130948BC

Z. W. Briesemeister, A. I. J. Skemer, J. M. Stone, J. M. Stone, T. S. Barman, P. Hinz, J. Leisenring, M. F. Skrutskie, C. E. Woodward, and E. Spalding

The Astronomical Journal, Volume 157, Issue 6, article id. 244, 13 pp. (2019)

DOI: 10.3847/1538-3881/ab1901,

Abstract

We present 2.9–4.1 μm integral field spectroscopy of the L4+L4 brown dwarf binary HD 130948BC, obtained with the Arizona Lenslets for Exoplanet Spectroscopy (ALES) mode of the Large Binocular Telescope Interferometer (LBTI). The HD 130948 system is a hierarchical triple system, in which the G2V primary is joined by two co-orbiting brown dwarfs. By combining the age of the system with the dynamical masses and luminosities of the substellar companions, we can test evolutionary models of cool brown dwarfs and extra-solar giant planets. Previous near-infrared studies suggest a disagreement between HD 130948BC luminosities and those derived from evolutionary models. We obtained spatially-resolved, low-resolution (R$\sim$20) L-band spectra of HD 130948B and C to extend the wavelength coverage into the thermal infrared. Jointly using JHK photometry and ALES L-band spectra for HD 130948BC, we derive atmospheric parameters that are consistent with parameters derived from evolutionary models. We leverage the consistency of these atmospheric quantities to favor a younger age (0.50 ± 0.07 Gyr) of the system compared to the older age ($0.79^{+0.22}_{-0.15}$ Gyr) determined with gyrochronology in order to address the luminosity discrepancy.

3.1 Introduction

Near-infrared (1–2.5 μm) adaptive optics-fed integral field spectrographs (OSIRIS, (Larkin et al., 2006); GPI, (Macintosh et al., 2008); SPHERE, (Claudi et al., 2008); Project 1640, (Hinkley et al., 2011); CHARIS, (McElwain et al., 2012)) have been detecting and characterizing exoplanets in high-contrast regimes for nearly a decade (e.g., (Bowler et al., 2010; Barman et al., 2011)). Since each wavelength slice of a data cube from an integral field spectrograph (IFS) can be analyzed using techniques for high-contrast image processing, integral field spectrographs are uniquely suited for high-contrast spectroscopy. Furthermore, planet-star spectral diversity can be harnessed to deliver better high-contrast imaging performance and sensitivity to planets compared to more traditional imagers (e.g., Zurlo et al., 2014).

While IFSs are uniquely capable for obtaining spatially-resolved spectra of exoplanets, adaptive optics-fed IFSs have been confined to the optical and near-infrared ($< 3\mu$m). Near-infrared spectra alone are insufficient for precise atmospheric constraints of brown dwarfs and exoplanets due to degeneracies between effective temperature, cloud coverage, convection and non-equilibrium carbon chemistry (e.g., Stephens et al., 2009; Skemer et al., 2014; Barman et al., 2015). Previous works have exploited broad wavelength spectrophotometry extending into the thermal infrared in order to constrain the thermal profiles, compositions, cloud

properties and bolometric luminosities of gas-giant planets (e.g., Currie et al., 2011; Barman et al., 2011; Madhusudhan et al., 2011; Marley et al., 2012; Skemer et al., 2012, 2014; Ingraham et al., 2014; Morzinski et al., 2015; Rajan et al., 2017).

In the thermal infrared (3–5 μm), the spectral energy distribution (SED) of gas-giant planets contains a low-opacity atmospheric window that emits a large fraction of a planet's flux (Low and Davidson, 1969; Bjoraker et al., 1986b; Burrows et al., 1997), especially at cool temperatures (see Figure 3.1). Major atmospheric absorbers, such as CH_4, CO and H_2O, have strong absorption features at $\sim$ 3.3μm, $\sim$ 4.7μm and $\sim$4–5 μm, respectively (Morley et al., 2014). Additionally, the thermal infrared continuum shape is sensitive to cloud thickness and patchiness (Madhusudhan et al., 2011; Currie et al., 2011; Skemer et al., 2014).

We built the Arizona Lenslets for Exoplanet Spectroscopy (ALES; Skemer et al., 2015) to extend the spectroscopic wavelength coverage available for directly imaged planets in order to better understand their atmospheric processes. ALES is the world's first adaptive optics-fed thermal infrared integral field spectrograph (IFS), and exists as a mode of LMIRcam (Skrutskie et al., 2010; Leisenring et al., 2012) — the 1–5 μm adaptive optics (AO) imager for the Large Binocular Telescope Interferometer (LBTI; Hinz et al., 2008a, 2012, 2014). With ALES, we can exploit these tools developed for high-contrast imaging to probe longer wavelengths and cooler effective temperatures (Figure 3.1).

In this work, we present a commissioning data set for ALES: the HD 130948 hierarchical triple system comprised of an L4+L4 brown dwarf binary — separated by $\lesssim 110$ mas — on a wide orbit ($\sim 2.''6$) around a sun-like primary star (G2V, [M/H] = 0.0, (Potter et al., 2002)). The HD 130948 system offers a rare laboratory to test substellar evolutionary models due to the independent measurements of age (from gyrochronology and chromospheric activity of the primary star), luminosity (from photometry and spectroscopy of the brown dwarfs themselves), and total mass of the brown dwarf pair (from orbital motion) (Dupuy et al., 2009). While HD 130948B and C are distinct from exoplanets, tests of substellar evolutionary models are key to calibrating models and improving our ability to understand exoplanet observations. Previous comparisons with evolutionary models suggest HD 130948B and HD 130948C are 2 to 3 times more luminous than predicted (Dupuy et al., 2009, 2014; Dupuy and Liu, 2017). In this work, we extend the spatially resolved flux constraints to longer wavelengths, providing a 2.9 to 4.1 μm spectrum of each component.

In Sections 3.2 and 3.3, we present our ALES observations of HD 130948 along with our reductions. We extract and calibrate spatially resolved spectra in Section 3.4. We fit custom model atmospheres to our spectra, and perform evolutionary model fitting with the derived bolometric luminosities and dynamical mass constraints to determine their individual masses in Section 3.5. In Section 3.6, we

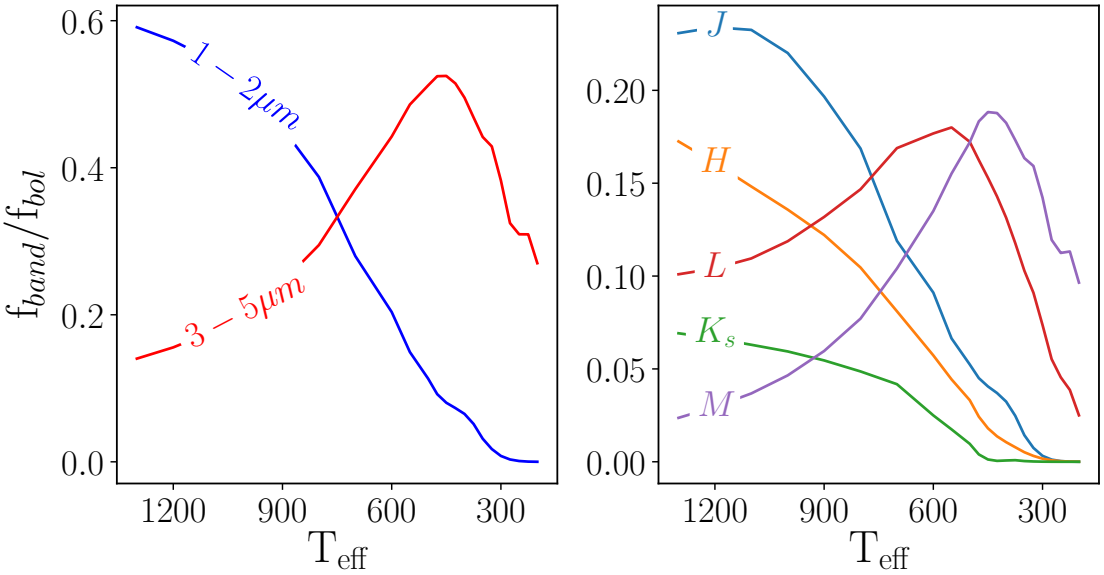

Figure 3.1: Left: Thermal emission with respect to bolometric flux in 1–2 μm and 3–5 μm for cold exoplanets. Right: Thermal emission with respect to bolometric flux in each band for cold exoplanets. The 1–2 μm contribution to the bolometric flux is negligible for the coldest objects. Models from (Morley et al., 2012, 2014).

discuss the implications of our results. We derive bolometric luminosities for each brown dwarf using a combination of near-infrared photometry and ALES L-band spectroscopy. The measured bolometric luminosity for each source is brighter than predicted by evolutionary models given the gyro-age of the primary star. We also check the consistency of the evolutionary models with the atmosphere parameters derived in the spectral fitting. We summarize our conclusions in Section 3.7.

3.2 Observations

We observed HD 130948 on 2016 March 26–28 UT as part of early commissioning activities with ALES. We used the left (SX) primary mirror of the two 8.4 meter primary mirrors of the LBT during photometric conditions and subarcsecond seeing. Visible light is directed towards the LBTI wavefront sensors for adaptive optics correction (Bailey et al., 2014) performed with the deformable secondary mirror (Esposito et al., 2011). Wavefront-corrected, diffraction-limited, infrared light is directed into the cryogenic universal beam combiner (UBC) and then into the Nulling and Imaging Camera (NIC; Hinz et al., 2008b) where LMIRcam (Skrutskie et al., 2010; Leisenring et al., 2012) resides.

For ALES operations, an 8× Keplerian magnifier, a silicon lenslet array with a pinhole grid to suppress diffraction, a blocking filter and disperser (direct-vision prism assembly) are introduced into the light path via LMIRcam filter wheels. The light incident on the spatial extent of each lenslet is focused through the diffraction-suppressing pinhole grid. Each lenslet sub-image is then dispersed by the direct-vision prism assembly. These dispersed sub-images are imaged onto a 5.2 micron-cutoff Teledyne HAWAII-2RG (H2RG, (Beletic et al., 2008)) as a grid of thermal infrared spectra.

At the time of observation, the FORCAST readout electronics (Leisenring et al., 2010) limited the detector readout to 1024×1024 pixels, instead of the

complete 2048×2048 pixels of the H2RG. This subarray contains 50×50 L-band spectra with spectral resolution R∼20, covering a field of view of $1.''\times 1.''3$. (Skemer et al., 2015) present a description of the design of the version of ALES used in this paper. Subsequent upgrades to ALES, available for current and future use, are described by (Hinz et al., 2018) and (Skemer et al., 2018a).

Table 3.1: HD 130948 Observations for 2016 March 28

Observation	$N_{pointings}$	N_{frames}	N_{coadds}	DIT[1]
HD 130948A	24	5	2	1s
HD 130948BC	24	30	2	1s
Sky	24	30	2	1s
Darks	24	9	1	1s

For this dataset, we took natural guide star AO observations of the hierarchical triple system, HD 130948, using HD 130948A as the reference star. The spatial scale of the HD 130948 system is larger than the field of view of ALES (the binary is separated by $2.''6$ from the primary). Therefore, the data were obtained in a three point pattern consisting of HD 130948A, sky, and HD 130948BC. Dark frames were obtained between each nod position while the telescope was in motion. A detailed description of this strategy can be found in (Stone et al., 2018a). Overall, we obtained the data described in Table 3.1. Four of the 24 pointings were discarded: two had the binary positioned close to the edge of the lenslet array and two had poor AO correction.

Wavelength calibration of the low-resolution spectra is performed using dome

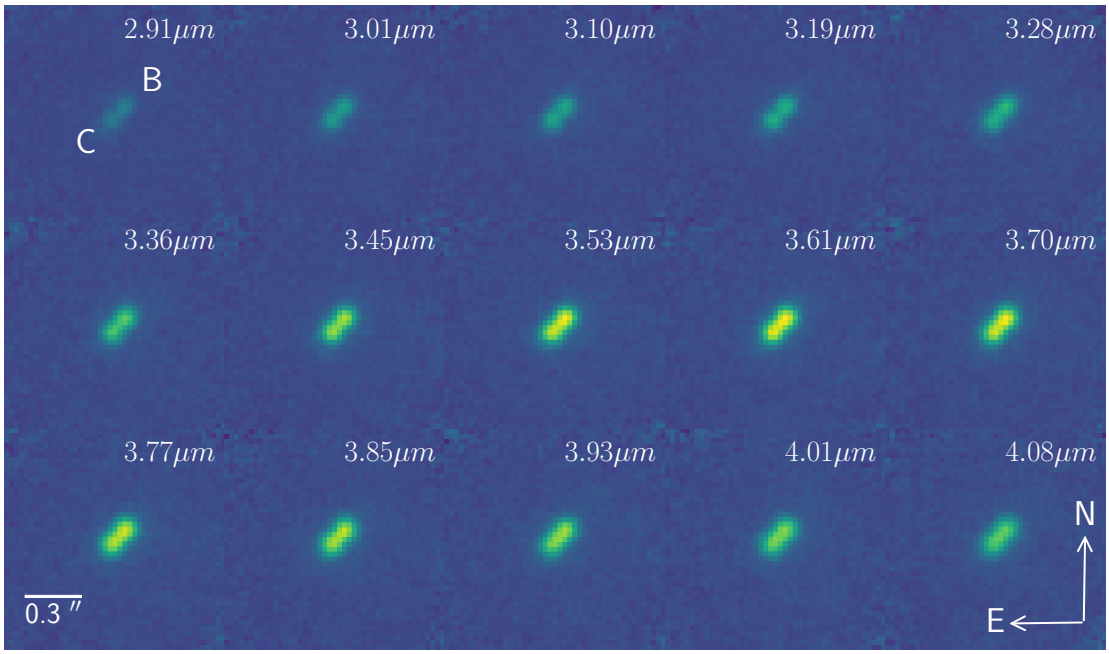

Figure 3.2: ALES data cube of HD 130948BC, where each image is a slice of the cube at the wavelengths specified in the upper right. These are a representative 15 wavelength slices of the 35 wavelength slices in each data cube.

flats at four spectrally unresolved narrowband (R∼100) filters spanning 2.9–3.9 μm (Stone et al., 2018a). An empirical dispersion relation is used to propagate the wavelength solution between the four data points for each spectrum.

3.3 Reduction

A raw ALES L-band frame consists of a grid of 2,500 spectra, each spanning $\sim 37 \times 7$ pixels, dispersed in a grid at a fiducial angle $\theta = \tan^{-1}(\frac{1}{2})$ with respect

to detector rows and columns. Raw ALES data were reduced using the ALES Python pipeline (`MEAD`, (Briesemeister et al., 2018)), with the steps performed as follows.

The first step performed by the pipeline is removal of detector artifacts, including the removal of residual detector channel bias, pixel flatfielding, background subtraction, and bad pixel correction.

For non-linearity correction, we constructed fluence-to-count curves for each pixel by taking sky flats of varying integration times without ALES optics in the light path. The sky flats were bias-subtracted and flatfielded. Outlier pixels were flagged as bad pixels. The linearity correction was applied to all frames. Frames of HD 130948BC had flux corrections $< 0.01\%$, sky frames had flux corrections of $< 0.5\%$ and frames of HD 130948A had flux corrections of $\sim 2\%$.

The 3.9 μm narrowband filter calibration data are used to coarsely locate the spectra on the detector. However, the calibration data for observations of HD 130948 on 2016 March 28 were taken at the end of the night; the telescope was set to zenith and the telescope experienced a different gravity vector. The irreproducibility of the multiple filter wheel positions, flexure, and the use of a distinct pupil stop for the calibration data resulted in a field dependent ($\lesssim 1$ pixel) shift between the calibration data and the science data. The deviations of the calibration data from science data, as well as the deviation of dispersion

direction from the fiducial angle, are calculated for each spaxel to parameterize a mapping of every light-sensitive pixel to a wavelength calibrated (λ, y, x) data cube. In order to turn the raw data into wavelength calibrated data cubes, we apply optimal extraction (Horne, 1986) to each spectrum, which becomes the associated spaxel in the data cube.

In a lenslet-based IFS, each lenslet has a slightly different throughput as a function of wavelength. To address this effect, a lenslet flat field is constructed from the normalized, dark-subtracted sky data cube. This is necessary because, by design, LBTI runs in pupil tracking mode only and does not rotate with the sky; astrophysical light of a binary system is incident on different lenslets over the course of observation due to sky rotation.

The cubes containing HD 130948BC and the cubes containing HD 130948A were derotated by the median parallactic angle during each HD 130948BC pointing. Each wavelength slice of every cube was registered with respect to the appropriate wavelength slice of the highest signal-to-noise data cube using the single step Discrete Fourier Transform (DFT) approach outlined in (Guizar-Sicairos et al., 2008). This registration technique calculates pixel-accuracy translations using DFT phase correlation and then upsamples the cross correlation by a factor of 1000 in a 1.5 $\times$1.5 pixel neighborhood of the estimated pixel shift for subpixel-accuracy translation.

Once the translations of the derotated cubes are determined, the registered, derotated cubes are made with a final interpolation of the original cubes that performs the derotation and registration simultaneously in order to avoid multiple interpolations. The sum of the science and sky variance images undergo the same optimal extraction process to be turned into data cubes, and the respective registration and derotation in a single step. The average of the group of data cubes, weighted by their respective inverse variance cubes, are the final (λ, y, x) data cubes of HD 130948BC and HD 130948A. The final (λ, y, x) variance cubes are the mean of all the propagated variance cubes. These final cubes and associated propagated variance cubes are then used for point-spread function (PSF) photometry.

The final cube for HD 130948BC is shown in Figure 3.2, in which the binary is centered in each wavelength frame denoted by their respective wavelengths. The $\sim$ 110 mas binary is resolved in L-band by ALES. Each image is 50 $\times$ 50 pixels, with one pixel corresponding to 26.1 mas. The binary appears brightest in the middle of the band because the sky transmission of L-band peaks at $\sim$ 3.6μm. The noise appears worse near the edges of each frame because fewer data cubes overlap in these regions.

3.4 PSF Photometry

We used PSF fitting to measure the flux from each component at each wavelength slice, explicitly allowing for spatial covariance in the images (See Appendix 3.7 for more details). We took a two-step approach, first fitting for binary separation and position angle, and then extracting flux with the respective priors of those two parameters. A two-step process is required because the position angle θ and separation ρ of the two brown dwarfs are expected to be constant across all wavelengths, while the position of the binary in the data cube can shift as a function of wavelength due to chromatic optics and atmospheric dispersion. The first step performs PSF subtraction at each wavelength slice completely independently. The second step repeats PSF fitting at each wavelength slice, including Gaussian priors for position angle θ and separation ρ, with hyperparameters derived from the first step.

Due to the adaptive optics correction, the HD 130948BC pair is far enough away from the primary star such that high-contrast post-processing algorithms for PSF subtraction are not used, so PSF subtraction does not dominate the correlation of noise in our data. However, interpolation and diffraction still induce spatial and spectral correlations for the HD 130948BC dataset. We extended the Bayesian framework used in (Wang et al., 2016), which coupled Bayesian parameter estimation for astrometry with a Gaussian process, to apply to a binary system

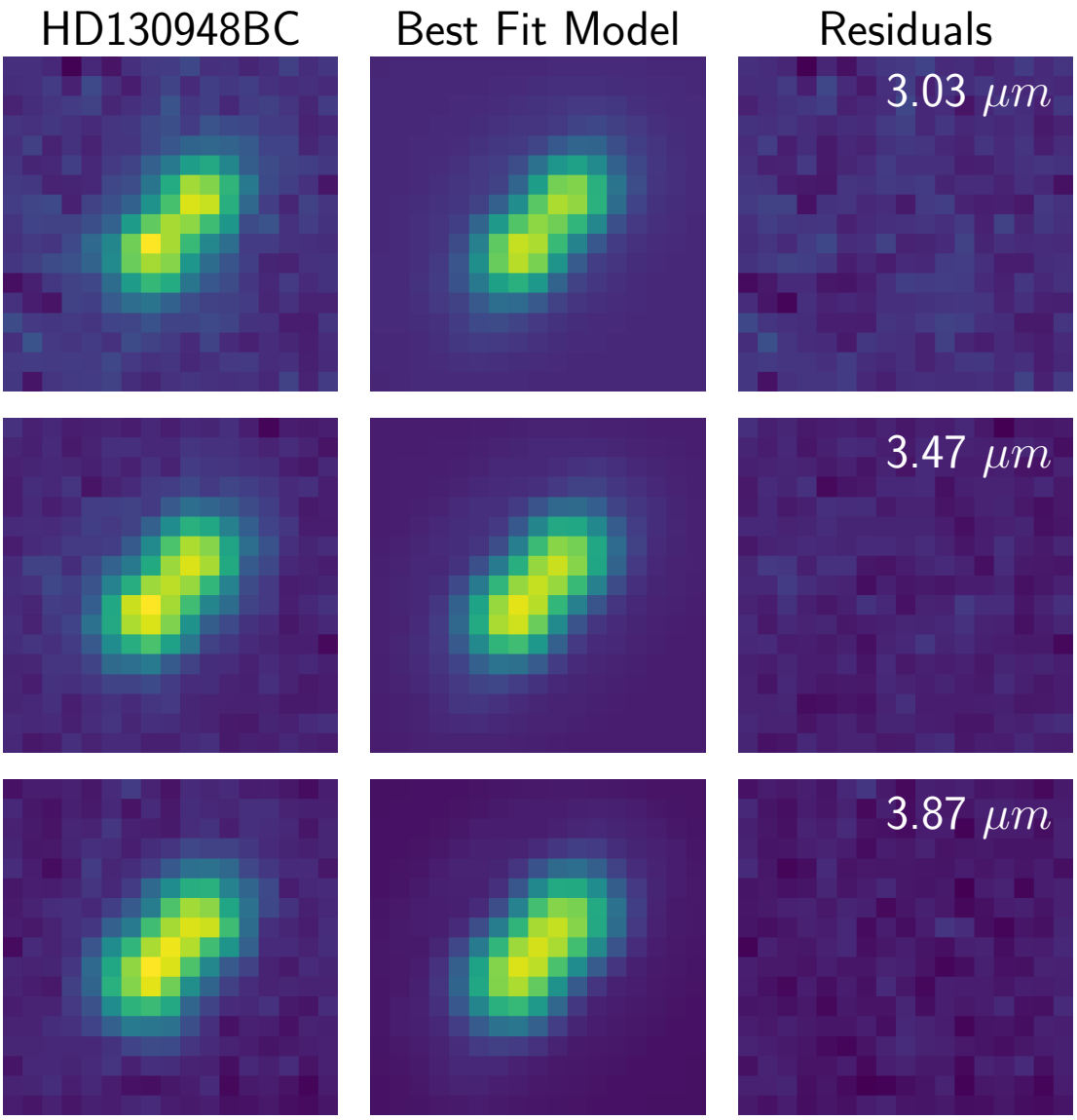

Figure 3.3: The first image in each row is a representative data cube slice of HD 130948BC at the wavelength denoted in the upper right corner of the row. The middle image in each row is the best fit model of two scaled PSFs that fit the binary. The right image depicts their residuals. Each wavelength of the cube produced quantitatively similar results. The color stretch is linear.

in order to account for the spatial noise covariance caused by interpolation during data reduction and forming data cubes. Since the squared exponential covariance function would produce improbably smooth noise realizations, we parameterized the spatial noise covariance by the Matérn ($\nu = 3/2$) covariance function

$$C_{\ell,ij} = \sigma_i \sigma_j \left(1 + \frac{\sqrt{3} r_{ij}}{\ell}\right) \exp\left(\frac{-\sqrt{3} r_{ij}}{\ell}\right) \tag{3.1}$$

where ℓ is the spatial correlation length of noise, r_{ij} is the Euclidean distance between i, j spaxels, and σ_i is the standard deviation associated with spaxel i. The spatial correlation length ℓ represents the strength of correlation between two spaxels averaged across the entire wavelength slice.

We remain agnostic to spectral correlation when each wavelength slice is treated independently from one another. However, imposing Gaussian priors on θ and ρ during the second step does introduce correlation between all wavelength slices. Interpolation and finite spectral resolution also contribute to spectral correlation. The characterization and treatment of spectral correlation is discussed in Section 3.5.1.

The details of the PSF fitting procedure are available in Appendix 3.7. We evaluated convergence with acceptance rates and the Gelman-Rubin convergence diagnostic (Gelman and Rubin, 1992; Brooks and Gelman, 1998). The best fit model at each wavelength was identified as the median of the marginalized posteriors, with 68%–credible regions of the marginalized posteriors as their uncer-

tainty. Representative best fit models and residuals at the 3.03, 3.47, and 3.87 μm wavelength slices of the data cube are shown in Figure 3.3, and the marginalized posteriors following the second PSF fitting step for the 3.47 μm wavelength slice is shown in Figure 3.4. The medians of the marginalized posterior distributions from the second step remained within the corresponding 68%–credible regions of the marginalized posteriors from the first step, with the exception of the far red end (>4 μm) of the band, where the PSF is larger and the binary is less resolved.

The spatial correlation lengths $\ell(\lambda)$ were determined empirically to trend linearly with wavelength with the form $\ell(\lambda) = (0.115 \pm 0.008 \frac{\text{px}}{\mu\text{m}})\lambda + (0.236 \pm 0.006\,\text{px})$. The amplitude of the spatial correlation is not consistent with the diffraction limit of the telescope ($\sim$4 px), suggesting interpolation from data cube construction and PSF fitting is contributing to small scale correlation, the ALES data cubes of HD 130948BC are not speckle limited, and the mean photon noise is background dominated. The PSF fitting procedure was repeated for data cubes and registration performed by strictly linear, cubic and quintic interpolation, and permutations thereof, and the spatial correlation lengths remained between 0.5 px and 0.9 px. The Bayesian parameter estimation of the other model parameters were unchanged with the different interpolation schemes.

The contrast spectrum for each brown dwarf is derived with respect to the primary star HD 130948, a G2V star with solar metallicity (Valenti and Fischer,

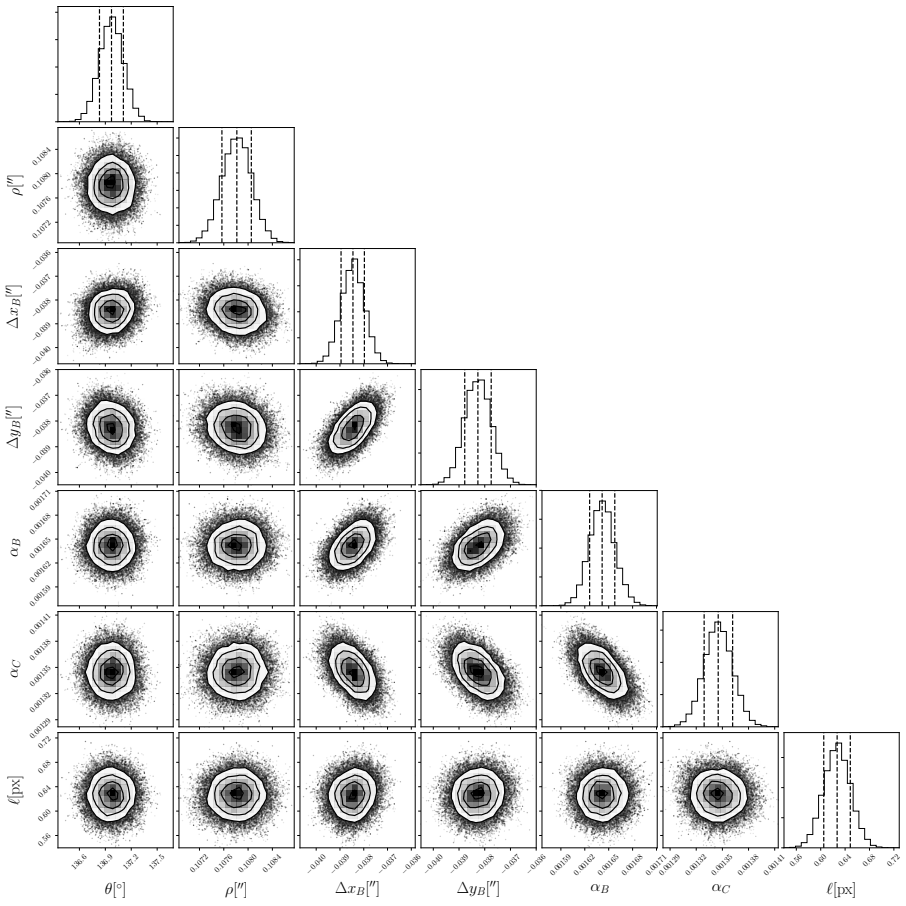

Figure 3.4: Posterior distributions for the position of HD 130948B and flux ratios of HD 130948BC with respect to HD 130948A in the representative 3.47μm wavelength slice. The posteriors are calculated at each wavelength, and the flux ratios are used to derive the spectrum of HD 130948BC by multiplying with the spectrum of HD 130948A. The contour levels are set to intervals of 0.5-σ.

2005). A model G2V spectrum (Hauschildt et al., 1999) was smoothed to the spectral resolution of ALES, and scaled by the WISE W1 (3.3526 μm; (Wright et al., 2010)) photometry data point of HD 130948A of 5.17 $\pm$ 0.40 Jy (Eiroa et al., 2013). HD 130948BC do not contribute significantly to the WISE W1 photometry of HD 130948A, as they are 7 magnitudes dimmer. The spatially-resolved contrast spectra of HD 130948B and C were then multiplied by the scaled model to get the absolute flux calibrated spectra for HD 130948BC with uncertainties propagated.

3.5 Analysis

3.5.1 Physical Parameters from Atmospheric Models

With the goal of providing a consistent description of the atmospheres of HD 130948BC using JHK photometry and L-band spectra, we will explore atmospheric model fitting of solely L-band spectra, solely NIR photometry, and joint NIR photometry plus L-band spectra.

The PHOENIX atmospheric code outlined in (Barman et al., 2011) was used to calculate the synthetic model spectra for this analysis. We chose to interpolate over a pre-synthesized library of model spectra calculated between 1500K and 2500K and $\log g = 4.5$ and $\log g = 5.5$, with resolutions of $\Delta T_{\rm eff} = 100K$, $\Delta \log g =$ 0.5 dex. The grid of spectra were log-linear interpolated at the native resolution of

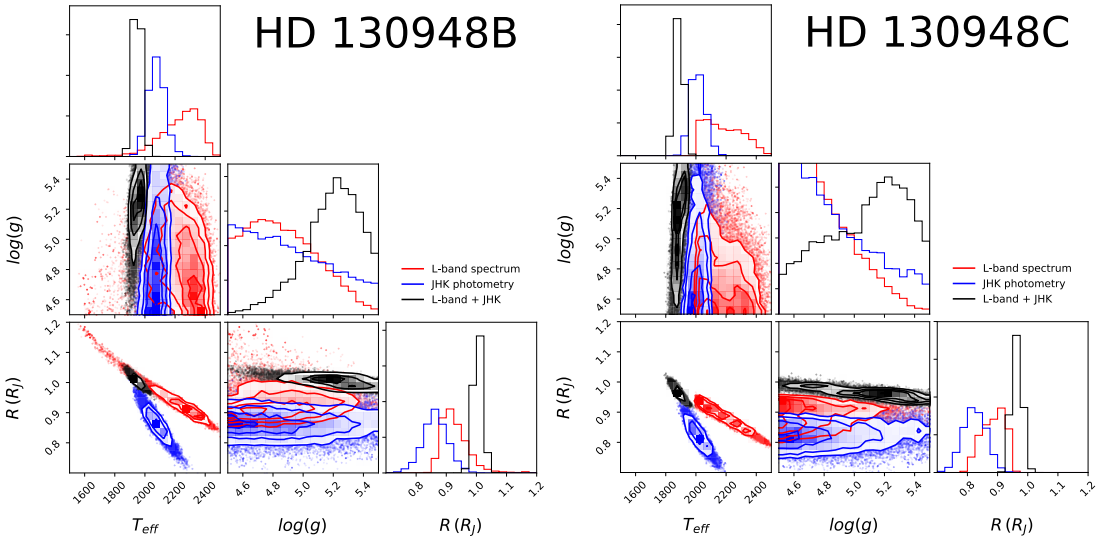

Figure 3.5: Posterior distributions for the near-infrared photometry fits in blue, L-band spectral fits in red and near-infrared photometry + L-band spectral fits in black for the atmosphere model derived quantities of HD 130948B and C. The contour levels are set to intervals of 0.5-σ. The medians and credible regions of these quantities are available in Tables 3.2 and 3.3, respectively. Note that these quantities are heavily correlated; the position of the joint marginalized posteriors not being intermediate between the individual marginalized posteriors is a projection effect, and a result of JHK photometry having limited sensitivity to surface gravity, while L-band spectra have limited sensitivity to temperature for hot substellar atmospheres.

the spectra to obtain flux density for arbitrary $k = [T_{\rm eff}, \log g]$. More sophisticated methods of spectral interpolation, such as Starfish ((Czekala et al., 2015)), were not used because the spectral resolution of ALES cubes requires convolution and downsampling that washes out the noding phenomenon described therein.

3.5.1.1 Modelling of ALES L-band spectra

Most integral field spectograph datasets are prone to spectral and spatial correlation. The ALES HD 130948 dataset is no different. In Section 3.4, we showed there is a non-negligible spatial correlation on subpixel scale. In (Greco and Brandt, 2016), a procedure for modelling spectral correlation is outlined, in which a three component model is proposed to characterize contributions of speckle noise, correlation induced by interpolation during reduction, and uncorrelated noise. With the formalism from Greco & Brandt, we estimated the correlation ψ_{ij} between pixel values at wavelengths λ_i and λ_j within a annulus of width 1.5 λ_c/D in the binary data with the binary masked out ($\lambda_c = 3.50 \mu m$). The correlation was fit with a three-component model, comprising an uncorrelated term with amplitude A_δ, spatially-independent Gaussian term with amplitude A_λ and correlation length σ_λ, and a spatially-dependent Gaussian term with amplitude A_ρ and correlation length σ_ρ. The respective amplitudes were fit such that $A_\delta = 0.55$, $A_\lambda = 0.27$, and $A_\rho = 0.18$. The noise components were characterized by correlation lengths $\sigma_\rho = 0.81$ and $\sigma_\lambda = 0.015$. The spectra are correlated to ~ 2 channels,

supporting our assumption we have $N_\lambda/2$ resolution elements for critical Nyquist sampling in Appendix 3.7. This method is not sensitive to the subpixel spatial correlation measured in Section 3.4 because there are no appropriate annuli to measure these lengths.

Bayes' Theorem is used to write the posterior probability for $k = [T_{\rm eff}, \log(g)]$ given observed spectrum f as, $\mathcal{P}(k \,|\, f) \propto \mathcal{L}(f \,|\, k)\, \mathcal{P}(k)$. To quantify the probability of the data conditioned on the model, $\mathcal{L}(f \,|\, k)$, we adopted the following multivariate Gaussian likelihood function (ignoring constants).

$$-\,2 \ln \mathcal{L}(f \,|\, k) = (f \,-\, \alpha F_k)^T\, \Sigma^{-1}\, (f \,-\, \alpha F_k) \tag{3.2}$$

where F_k is the synthetic spectrum for model k, $\Sigma_{ij} = \sigma_i \sigma_j \psi_{ij}$ for flux errors σ, and $\alpha = (R/D)^2$ for brown dwarf radius R and distance D to the system.

The prior on surface gravity and temperature are defined by the domain limits: $\mathcal{P}(\log(g)[cgs]) = \mathcal{U}[4.5, 5.5]$, $\mathcal{P}(T_{\rm eff}[K]) = \mathcal{U}[1500, 2500]$. Realistic priors from evolutionary models could be applicable here. However, (Dupuy et al., 2010) discuss the existence of a systematic discrepancy between atmosphere and evolutionary model-derived quantities and evolutionary model-predicted quantities from data. It is for this reason that we avoid using the evolutionary models as realistic priors in the atmospheric model fitting suggested in (Greco and Brandt, 2016).

Gaia DR2 provides revised parallax measurements of HD 130948A of $\pi = 54.91 \pm .07$ mas (*Gaia*; Gaia Collaboration et al., 2016, 2018). The presence

of the brown dwarf companions will cause deviations from parallactic trajectory with linear proper motion due to stellar reflex motion, but the lower bound on the orbital period is 155 yr (Ginski et al., 2013); only a fraction of the orbit is traversed during the *Gaia* baseline, suppressing the reflex motion signal. Moreover, HD 130948 is a bright star (G = 5.715) in the *Gaia* catalog, in which stars with G $\lesssim$ 6 have weaker positional accuracy due to saturation of the detector, placing reflex motion signal below the noise floor associated with the parallax uncertainty. We proposed Gaussian priors for parallax π to estimate the prior on distance as follows, $\mathcal{P}(D[pc]) = |\frac{\partial \pi}{\partial D}| \cdot \mathcal{N}[\pi; \pi, \sigma_\pi^2] = D^{-2}\mathcal{N}[1/D; \pi, \sigma_\pi^2]$. The prior for brown dwarf radius was set to $\mathcal{P}(R[R_J]) = \mathcal{LU}[0.5, 1.5]$, with physically motivated limits from evolutionary models and a lack of high insolation.

We used the (Goodman and Weare, 2010) affine-invariant MCMC sampler implemented in the `emcee` Python package (Foreman-Mackey et al., 2013) to sample the posterior distribution of $[T_{\rm eff}, \log g, R, D]$ for HD 130948B and HD 130948C independently. We initialized 50 walkers with a guess k vector plus Gaussian noise at an amplitude of $k \times 10^{-4}$. Each MCMC sampler was run for 400 steps after 400 burn-in steps. We evaluated convergence of the chains with the Gelman-Rubin convergence diagnostic. The resulting marginalized posteriors can be seen in red in Figure 3.5. Median and credible regions of these posteriors are reported in Tables 3.2 and 3.3. The best fit L-band spectra of HD 130948B and HD 130948C

have $\chi^2_B = 13.7$ and $\chi^2_C = 21.1$. For 31 spectral bins and free parameters of $k = [T_{\rm eff}, \log g, R]$, these appear to be anomalously low χ^2 values. However, the spectral correlation length of ~ 2 channels reduces the effective number of degrees of freedom by roughly half.

3.5.1.2 Modelling of Near-infrared Photometry

(Dupuy et al., 2009) measured the MKO JHK photometry of HD 130948BC, which was updated with progressively homogenized analyses in (Dupuy et al., 2014) and (Dupuy and Liu, 2017). (Crossfield, 2014) presents 2MASS JHK_s photometry that is consistent with the MKO photometry for both brown dwarfs. We chose to use the MKO photometry due to the smaller uncertainty in the photometry. We did not include any covariance in the JHK photometry.

We approach atmospheric modelling of near-infrared photometry using χ^2-fitting. Synthetic photometry F_k was calculated for each model k using MKO filter curves (Tokunaga et al., 2002). We used identical priors from Section 3.5.1.1, with the same motivations. To quantify the probability of the data conditioned on the model, we used Equation 3.2 in the regime where Σ is diagonal. We sampled the posterior distribution of $[T_{\rm eff}, \log g, R, D]$ for HD 130948B and HD 130948C independently with `emcee` under the same conditions as Section 3.5.1.1, satisfying the same convergence testing, and the resulting marginalized posteriors can be seen in blue in Figure 3.5. Median and credible regions of these posteriors are

reported in Tables 3.2 and 3.3. The best fit JHK photometry of HD 130948B and HD 130948C have $\chi^2_B = 6.4$ and $\chi^2_C = 10.6$.

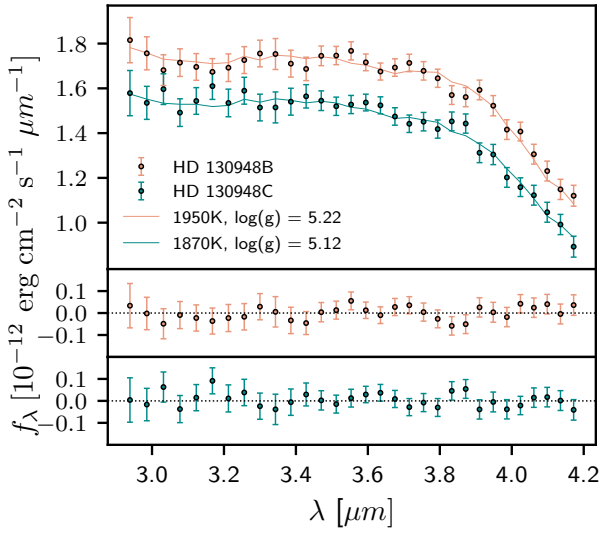

Figure 3.6: Spectra of HD 130948BC with best fit models from (Barman et al., 2011) using the near-infrared plus L-band fit. The residuals for each fit are plotted below with the color corresponding to the same object in the spectrum.

3.5.1.3 Modelling of Photometry and Spectra

Combining photometry and spectroscopy to back out meaningful atmospheric properties can unintentionally be driven by weighting schemes. The goodness-of-fit statistic G_k from (Cushing et al., 2008) is a commonly used statistic with weights proportional to the wavelength interval associated with the data points. While the G_k allows for heteroskedasticity, it implicitly assumes no correlation between spectral channels.

We approached this problem with two methods: apply no objective weighting scheme and use the covariance measured in L-band or apply objective weights according to (Cushing et al., 2008) and ignore the covariance in L-band. We chose to avoid extending the definition of the goodness-of-fit statistic G_k to include covariance because it is not obvious whether the weighting scheme applies to off-diagonal covariance terms when correlation ψ_{ij} is measured in this manner.

We determined empirically that the posterior derived when applying no objective weights and using the covariance matrix completely contained the posterior when applying objective weights and ignoring the covariance. Therefore, we chose to ignore weights and favor including the covariance matrix. In principle, this means that near-infrared photometry are contributing less to the likelihood function.

We used identical priors from Section 3.5.1.1, with the same motivations. We also used the same functional form of the likelihood (Equation 3.2), with $\psi_{i \neq j} = 0$ for the three photometry points. We sampled the posterior distribution of $[T_{\rm eff}, \log g, R, D]$ for HD 130948B and HD 130948C independently with `emcee` under the same conditions as Section 3.5.1.1, satisfying the same convergence testing, and the resulting marginalized posteriors can be seen in black in Figure 3.5. Median and credible regions of these posteriors are reported in Tables 3.2 and 3.3. The best fit JHK photometry and L-band spectra of HD 130948B and

HD 130948C have $\chi^2_B = 20.1$ and $\chi^2_C = 31.8$.

Composite spectral energy distributions (SED) of B and C were built using JHK photometry data over their respective bandpasses, the L-band spectra of B and C, and filling in the rest of the SED with the best fit model spectra for each suite of fitting procedures (e.g., Morzinski et al., 2015). The bolometric luminosities were calculated by integrating these composite spectra. The uncertainty in the bolometric luminosities is derived using a Monte Carlo simulation, taking composite spectra drawn from both a multivariate Gaussian with the mean set to the spectrophotometry and covariance set to Σ and model spectra from the respective posteriors, and estimating the standard deviation of their bolometric luminosities. We also performed a Monte Carlo simulation with spectral energy distributions associated with the best fit model spectra of B and C, excluding $JHKL$ data. The median remained unchanged, and the composite spectra method resulted in larger uncertainty. We report the composite SED bolometric luminosity uncertainty in Tables 3.2 and 3.3.

Figure 3.6 contains the ALES L-band spectra of HD 130948B and C, along with the model fits with parameters set to the medians of the marginalized posteriors from spectral fits for $JHK + L$ spectrophotometry. All following analysis is performed using these median and credible regions, reported in column $JHK + L$ in Tables 3.2 and 3.3.

Table 3.2: Atmosphere Model Inferred Properties of HD 130948B

Property	JHK	L	JHK+L
$T_{\rm eff}$ [K]	2060 ± 60	2260^{+100}_{-150}	1950 ± 30
Radius [R_J]	0.87 ± 0.04	$0.92^{+0.04}_{-0.03}$	1.00 ± 0.01
log(g) [cm s^{-2}]	$4.5^{+0.7}_{-0.5}$	$4.7^{+0.3}_{-0.4}$	5.2 ± 0.3
log(L_{bol}) [$L_\odot$]	-3.88 ± 0.02	-3.87 ± 0.02	-3.87 ± 0.01

Table 3.3: Atmosphere Model Inferred Properties of HD 130948C

Property	JHK	L	JHK+L
$T_{\rm eff}$ [K]	2000 ± 60	2200^{+150}_{-180}	1870 ± 30
Radius [R_J]	0.83 ± 0.04	$0.87^{+0.06}_{-0.03}$	0.98 ± 0.02
log(g) [cm s^{-2}]	$4.4^{+0.5}_{-0.4}$	$4.3^{+0.4}_{-0.3}$	5.1 ± 0.3
log(L_{bol}) [$L_\odot$]	-3.97 ± 0.02	-3.97 ± 0.02	-3.96 ± 0.01

3.5.2 Individual Masses of HD 130948B and C

Benchmark systems like HD 130948BC provide the rare laboratory necessary to obtain individual masses of brown dwarfs, a measurement that is crucial to tests of evolutionary models. For most directly imaged planets, we must rely on evolutionary models to convert luminosity to mass given an age estimate (and potentially information on formation and initial entropy), so putting such models to the test is essential. In order to do this test, we need to isolate the mass of each object using the total mass constraint from orbital monitoring and our measurements of bolometric luminosity.

Substellar objects will tend to radiatively cool with time (Stevenson, 1991; Burrows and Liebert, 1993); evolutionary models of substellar objects propose

Table 3.4: Evolutionary Model Inferred Properties of HD 130948BC

Property	HD 130948B	HD 130948C
Input Observed Properties		
Mass [M_J]	$116.2^{+0.9}_{-0.8}$	
log(L_{bol}) [$L_\odot$]	-3.87 ± 0.01	-3.96 ± 0.01
(Saumon and Marley, 2008) Hybrid Models		
Mass [M_J]	59.8 ± 0.6	56.4 ± 0.6
log(L_{bol}) [$L_\odot$]	-3.87 ± 0.01	-3.96 ± 0.01
q [M_C/M_B]	0.94 ± 0.01	
Age [Gyr]	0.45 ± 0.01	
$T_{\rm eff}$ [K]	1900 ± 20	1800 ± 20
Radius [R_J]	$1.037 \pm .002$	$1.037 \pm .002$
log(g) [cm s^{-2}]	5.14 ± 0.01	5.11 ± 0.01
(Baraffe et al., 2015) Models		
Mass [M_J]	59.8 ± 0.6	56.3 ± 0.5
log(L_{bol}) [$L_\odot$]	-3.86 ± 0.01	-3.97 ± 0.01
q [M_C/M_B]	0.94 ± 0.01	
Age [Gyr]	$0.51^{+0.01}_{-0.02}$	
$T_{\rm eff}$ [K]	1960 ± 20	1840 ± 20
Radius [R_J]	$0.991^{+0.005}_{-0.002}$	$0.990^{+0.005}_{-0.002}$
log(g) [cm s^{-2}]	5.18 ± 0.01	5.16 ± 0.01

a luminosity-age-mass relationship, owing to a lack of a sustainable source of internal energy from nuclear reactions, with more massive objects starting hotter and more luminous. We exploit this relationship with evolutionary models from (Baraffe et al., 2015) and (Saumon and Marley, 2008) to isolate the masses and age of HD 130948BC. Since the measured luminosities are nearly equal, extreme mass ratios can be ruled out. Therefore, breaking the mass degeneracy is primarily driven by the tight dynamical mass and bolometric luminosity constraints instead of the evolutionary models themselves.

For individual ages between 1 Myr and 1 Gyr, we calculate two masses with the prior that their sum is distributed according to the dynamical mass posterior. With revised parallax from *Gaia* DR2, the total dynamical mass of HD 130948BC derived from astrometric analysis reported in (Dupuy and Liu, 2017) of $M_{dyn} = 115.4^{+2.2}_{-2.1}\,M_J$ is updated to $M_{dyn} = 116.2^{+0.9}_{-0.8}\,M_J$. The model bolometric luminosity is calculated by log-linearly interpolating the evolutionary model grids. The log-likelihood is calculated from the residuals of model luminosities and measured luminosities of HD 130948BC and their respective errors. Uniform bounded priors were used for the age of the system. The posterior distribution of masses of each component and the age of the system was sampled using `emcee`. The credible regions from the resulting marginalized posteriors are reported for both sets of models in Table 3.4. The apparent bolometric fluxes from HD 130948B and C at best fit are $(1.31 \pm 0.03) \times 10^{-11}$erg s^{-1} cm^{-2} and $(1.07 \pm 0.03) \times 10^{-11}$erg s^{-1} cm^{-2}, respectively.

3.6 Discussion

Independent validation of atmospheric and evolutionary models is critical for characterizing the atmospheres of directly imaged extrasolar planets and brown dwarfs. The masses of directly imaged exoplanets and brown dwarfs are generally poorly constrained owing to the difficulty in independently measuring masses, and

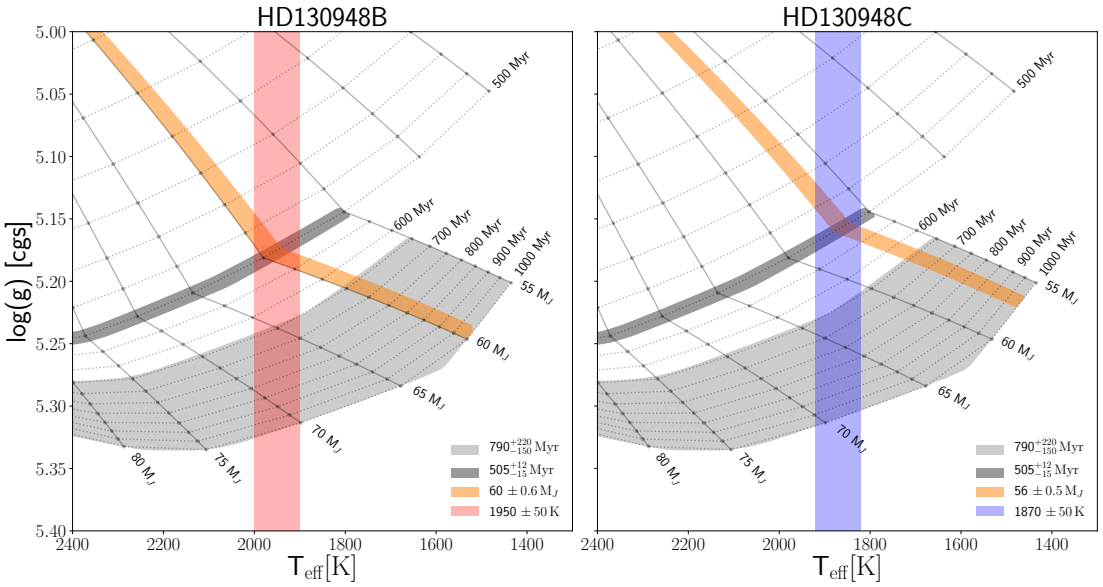

Figure 3.7: Isomass lines in solid black and isochrones in dashed black lines from (Baraffe et al., 2015). The light gray region corresponds to the gyrochronology constraint from the primary star. The dark gray region corresponds to the 68%–credible regions of age derived from the evolutionary model fitting of HD 130948BC according to Section 3.5.2. The orange regions correspond to the credible regions of mass derived from the evolutionary model fitting of HD 130948BC. The red and blue regions correspond to the credible regions of temperature derived from the atmospheric model fitting of HD 130948BC.

inferences being extremely model-dependent. Yet mass is fundamentally important to test models of giant planet formation and empirically calibrate substellar evolutionary models. HD 130948B and C are some of the only brown dwarfs with independently measured mass, age, and luminosity to probe these models (Dupuy et al., 2009; Konopacky et al., 2010; Dupuy et al., 2014; Dupuy and Liu, 2017).

3.6.1 Evolutionary and Atmospheric Models

The atmosphere model fitting is independent of the evolutionary models (apart from physically motivated bounds on the radius prior). The evolutionary model fits are only informed by the modeled bolometric luminosities of HD 130948B and C, which is driven by the data, and independent dynamical mass measurements. The different models are not strictly expected to derive consistent atmosphere quantities. Specifically, near-infrared spectroscopy has been shown to produce atmospheric model fits that are discrepant by 250K from evolutionary model fits to the same data set (Dupuy et al., 2010).

Our fits to L-band spectra have similarly derived temperatures $\sim$ 250 K warmer than the other two methods (Tables 3.2 and 3.3). The coarse sampling of atmospheric parameters for the atmospheric model grid also limits what can be determined from the surface gravity measurement. At ALES spectral resolution and this temperature regime, L-band does not vary significantly with surface

gravity, and there are no prominent features that are highly gravity dependent. While L-band is not particularly diagnostic of atmospheric parameters for hotter objects, L-band becomes critical at lower temperatures (e.g., Skemer et al., 2014; Barman et al., 2015).

However, atmospheric model fitting to the combination of JHK photometry and L-band spectra for HD 130948B and C has resulted in posteriors that are completely consistent with evolutionary model-derived quantities, illustrating the importance of extended wavelength coverage for substellar objects. Figure 3.7 depicts isomass lines and isochrones in effective temperature-surface gravity space with evolutionary models from (Baraffe et al., 2015). The red and blue regions denote the credible regions of effective temperature (and surface gravity) from atmosphere model fitting, including the grid spacing errors set to half the grid spacings ($\sigma_{T_{\rm eff}} = 50K$, $\sigma_{\log g} = 0.25$ dex). The publicly available evolutionary models did not continue past 1 Gyr in this mass regime.

3.6.2 Age of HD 130948

We assume coevolution of the binary brown dwarfs with the primary star for the following discussion. With the method described in Section 3.5.2, the Baraffe et al. 2015 (BHAC15) and hybrid Saumon & Marley 2008 (SM08) evolutionary models were used to derive an age of $0.51^{+0.01}_{-0.02}$ Gyr and 0.45 ± 0.01 Gyr for

HD 130948BC, respectively. Both evolutionary model-derived ages are consistent with the age of HD 130948A as traced by the Ca II HK emission of 0.5 ± 0.3 Gyr (Dupuy et al., 2009), the previous evolutionary model-derived age of 0.44 ± 0.04 (Dupuy and Liu, 2017), and the (Barnes, 2007) relationship for gyrochronological age of $0.65^{+0.13}_{-0.10}$ Gyr.

The gyrochronology relation from (Mamajek and Hillenbrand, 2008) results in an age of $0.79^{+0.22}_{-0.15}$ Gyr does remain an outstanding topic of discussion, due to its adoption as the age of the system in (Dupuy et al., 2009).

One factor in this adoption is the observation that the $B-V$ color of HD 130948A suggests an age marginally consistent with, if not older than, the Hyades cluster. The Hyades cluster was believed to have a tight age constraint of 625 $\pm$ 50 Myr (Perryman et al., 1998). However, (Brandt and Huang, 2015b,a) have fit rotating stellar models to main-sequence turnoff Hyads to measure the age of the Hyades cluster to be older and with wider spread (750 $\pm$ 100 Myr). If the Hyades are systematically older, gyrochronology relations would need to be re-calibrated to ameliorate the updated age (Douglas et al., 2016). It should also be noted that (Gossage et al., 2018) used a different prescription of rotating stellar models and derived an age $\sim$ 680 Myr, which is roughly consistent with the canonical age of the cluster. For HD 130948A to be strictly older than the Hyades, the bolometric luminosities of HD 130948B and C would be considerably overluminous compared

to the predictions from evolutionary models.

Several possible explanations exist for the age discrepancy, including (1) the treatment of clouds, metallicities, atmospheric opacities plays a major role evolutionary models (Burrows et al., 2011), (2) evolutionary models systematically overpredict cooling rates of substellar objects (Dupuy et al., 2011), (3) very strong, interior magnetic fields inhibit the onset of convection in HD 130948BC (Mullan and MacDonald, 2010), (4) the efficiency of convection that decreases for fast-rotating, highly magnetic low-mass stars extends to substellar evolution (Chabrier et al., 2007), (5) atypical stellar rotation can be induced from formation via gravitational instability in a long-lived, massive circumstellar disk (Dupuy et al., 2014), and (6) systematic offsets in gyrochronology relations for field G stars (Mamajek and Hillenbrand, 2008). Probing these explanations is beyond the scope of this paper, but will become critical to investigate cooler objects with any precision.

Luminosity evolution for the HD 130948B and C are depicted in Figure 3.8. The individual lines and linewidth correspond to the median and 68%–credible regions of mass of best-fit as derived in Section 3.5.2, propagated from 100 Myr to 1 Gyr using the two evolutionary models. This plot is qualitatively identical to Figure 10. of (Dupuy et al., 2009).

The consistency of atmospheric quantities derived from evolutionary model fitting and atmospheric model fitting for HD 130948BC provides complementary

evidence to support the age derived from the evolutionary model fits. We chose to focus on BHAC15 evolutionary models. A Monte Carlo simulation was performed using draws of the atmosphere model-derived ($JHK + L$) effective temperature posteriors and the individual mass posteriors derived in the evolutionary model fitting, and propagated through the evolutionary model grid to obtain an average age for each draw of an effective temperature and mass for B and C. The age derived using BHAC15 models was 0.50 ± 0.07 Gyr, which is consistent with the age traced by Ca II HK emission and the (Barnes, 2007) gyrochronology age.

The derived age of HD 130948BC is younger than age estimates of the Hyades, while the $B - V$ color and rotational period of HD 130948A lie in parameter space beyond the 625 Myr isochrone of the Hyades (Perryman et al., 1997; Gaidos et al., 2000; Mamajek and Hillenbrand, 2008). Leveraging the consistency of atmospheric and evolutionary models for HD 130948BC and assuming the binary and primary are coeval, we invoke anomalous stellar angular momentum loss as an explanation of the systematically older age estimates from gyrochronology relationships (Barnes, 2007; Mamajek and Hillenbrand, 2008) from evolutionary model-derived ages for HD 130948.

This explanation, however, is not sufficient to describe the behavior of other over-luminous substellar objects, such as Gl 417BC. The Gl 417 system is a hierarchical triple system similar to HD 130948, with the Gl 417BC brown dwarf

binary separated 90 arcseconds from their primary star Gl 417A, and therefore ineffective at driving anomalous stellar angular momentum loss (Dupuy et al., 2014).

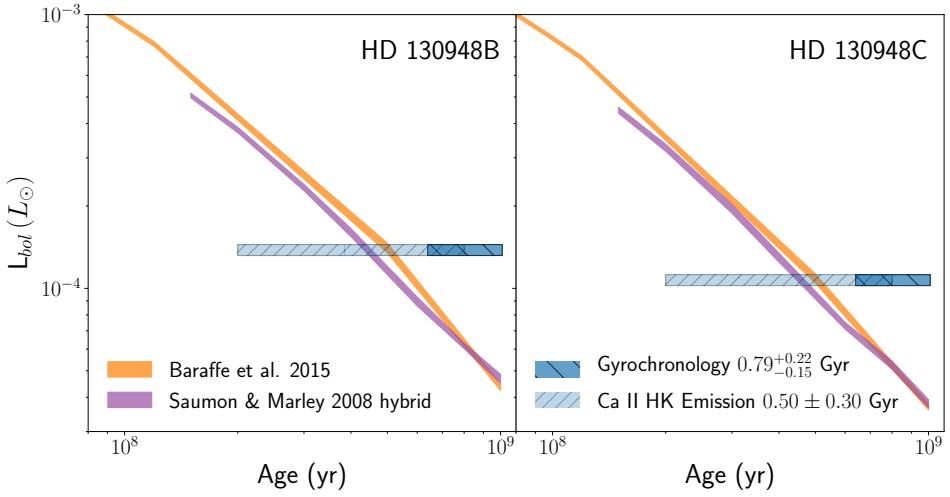

Figure 3.8: Isomass lines from (Baraffe et al., 2015) and (Saumon and Marley, 2008) evolutionary models for the best fit masses of HD 130948BC with the thickness of the line corresponding to the 68%–credible region in mass. The two blue boxes correspond to the two age constraints derived in (Dupuy et al., 2009) for the age of the primary HD 130948A through gyrochronology and chromospheric activity.

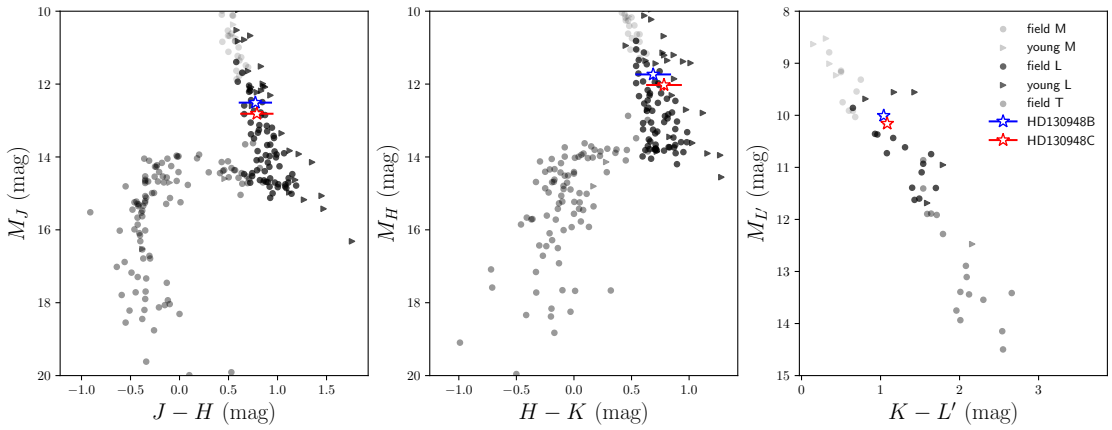

Figure 3.9: Color magnitude diagram for field M, L and T brown dwarfs with HD 130498 BC. The data for the field brown dwarfs and the JHK magnitudes of HD 130948BC are from the Database of Ultracool Parallaxes (Dupuy and Liu, 2012; Dupuy and Kraus, 2013; Liu et al., 2016) and (Dupuy and Liu, 2017), respectively.

3.6.3 Spectrophotometric Characterization of HD 130948BC

Section 3.5.1 presents fitting the spectral energy density with three distinct methods, each of which produce broadly consistent atmosphere parameters for two L4 brown dwarfs. Around 1800-2000K brown dwarfs, the spectral features in L-band are dominated by the H_2O pseudo-continuum (Barman et al., 2015). At ALES resolution, cooler temperature brown dwarfs ($<$1800K) begin to exhibit CH_4 PQR-branch absorption that suppress the water pseudo-continuum near 3.3 μm. No significant methane absorption is evident in the L-band spectra of HD 130948BC, placing the pair earlier than L5 spectral type. Due to the lack of spectroscopic standards in L-band, we defer to the spectral type determination of

L4 ± 1 from the literature (Goto et al., 2002).

The color magnitude diagram with field brown dwarfs and HD 130948BC is plotted in Figure 3.9. Synthetic $L'/W1$ photometry was calculated by using the MKO-L'/WISE-$W1$ filter curve and the ALES spectra of HD 130948BC. Synthetic L' magnitudes of HD 130948BC are 11.308 ± 0.034 mag and 11.461 ± 0.039 mag, respectively. The delta L' magnitude between HD 130948B and HD 130948C is 0.153 ± 0.034. The calculated $K - L'$ for HD 130948BC are 1.040 ± 0.042 mag and 1.080 ± 0.042 mag, respectively. The synthetic $W1$ magnitudes of HD 130948BC are 11.727 ± 0.036 mag and 11.856 ± 0.043 mag, respectively. The delta $W1$ magnitude between HD 130948B and HD 130948C is 0.129 ± 0.037. The calculated $K - W1$ for HD 130948BC are 0.622 ± 0.042 mag and 0.689 ± 0.042 mag, respectively.

Near-infrared spectra of HD 130948BC exist, but the observation suffered from differential slit loss (Goto et al., 2002). The continuum contains the temperature and gravity information, so we chose not to include this dataset for spectral fitting. However, Goto et al. did identify 2MASSW J00361617+1821104 (L4) as being the best-matched template spectrum for both the observed HD 130948BC medium resolution HK spectra. Photometry of the 2MASSW J00361617+1821104 was used to calculated $K - L'$ of 0.96 ± 0.058 (Leggett et al., 2002; Knapp et al., 2004). Comparing the three L4 brown dwarfs, both HD 130948BC are slightly

redder, perhaps due to adolescence.

There also exists resolved optical photometry of the binary from HST/ACS-HRC (Dupuy et al., 2009). These data comprise flux ratios of HD 130948BC in four red-optical bandpasses. In order to simultaneously fit red-optical photometry, NIR photometry and L-band spectroscopy, our model grid would need to be expanded considerably to cover a much broader range of parameters (e.g., abundances, cloud properties, non-equilibrium chemistry). An extensive parameter search is beyond the intended scope of this paper. The synthetic flux ratios calculated for the JHK+L best fit for $F850LP$, $FR914M$ (8626 Å), $FR914M$ (9402 Å), and $FR914M$ (10248 Å) are 0.10 ± 0.03, 0.31 ± 0.03, 0.40 ± 0.03, and 0.44 ± 0.02 mag, respectively.

3.7 Conclusion

We obtained 2.9–4.1 micron spectra of HD 130948BC with the ALES integral field spectrograph. This is the first time an adaptive optics-fed integral field spectrograph has been used at these wavelengths. We demonstrated that atmospheric models are able to reproduce the spectral energy distributions of these benchmark brown dwarfs. The JHK photometry and L-band spectra become potent constraints when used in tandem, recovering parameters consistent with the evolutionary model fits. Our results suggest low-resolution L-band spectra

can ameliorate the discrepancy of atmosphere fits and evolutionary model fits for objects with only JHK photometry, making ALES a powerful tool in aiding our understanding of evolutionary and atmosphere models.

Our determination that the ALES spectra can aid near-infrared measurements in characterizing the atmospheres of HD 130498BC has been the culmination of the development of a versatile pipeline and observation strategy that sets ALES as a new instrument capable of characterizing the thermal spectral properties of directly imaged planets and brown dwarfs. When JWST launches, there will be enormous scientific opportunity for studying exoplanets in the thermal infrared. ALES will be complementary to JWST. While ALES is less sensitive, it probes smaller inner working angles, especially in the context of spectroscopy. Both JWST and ALES will increase the wavelength range over which we study directly-imaged planets, which will be especially important as we begin to study colder exoplanets.

Acknowledgements

The LBT is an international collaboration among institutions in the United States, Italy and Germany. LBT Corporation partners are: The University of Arizona on behalf of the Arizona university system; Istituto Nazionale di Astrofisica, Italy; LBT Beteiligungsgesellschaft, Germany, representing the Max-Planck So-

ciety, the Astrophysical Institute Potsdam, and Heidelberg University; The Ohio State University, and The Research Corporation, on behalf of The University of Notre Dame, University of Minnesota and University of Virginia. This paper is based on work funded by NSF Grants 1608834 and 1614320.

JMS is supported by NASA through Hubble Fellowship grant HST-HF2-51398.001-A awarded by the Space Telescope Science Institute, which is operated by the Association of Universities for Research in Astronomy, Inc., for NASA, under contract NAS4-26555. Barman is supported by NSF AAG awards 1405505 and 1614492 and NASA XRP award NNX17AB63G. ZWB is supported by the National Science Foundation Graduate Research Fellowship under Grant No. 1842400.

Appendix A: Bayesian Parameter Estimation for PSF Fitting

In the following procedure, the subscript λ will be dropped for clarity; the procedure implicitly applies to each wavelength slice in the data cube. For each wavelength slice of the PSF and binary, there are six parameters ϕ defining a model of the two brown dwarfs with two shifted PSFs: the position (y_B, x_B) of HD 130948B, the position angle θ and the projected separation of the brown dwarfs ρ, the contrast ratios α_B and α_C of HD 130948BC with respect to the

PSF, HD 130948A, and a hyperparameter ℓ corresponding to a spatial correlation length. An additive factor to quantify sky background offsets was determined empirically to be consistent with zero, and therefore not included.

The binary $\mathcal{D}$ is modeled by shifting and scaling the PSF, $\mathcal{A}$, to each object. The unscaled model for HD 130948B is $\mathcal{A}_B(\phi) = \mathcal{A}[y_B, x_B]$ and the unscaled model for HD 130948C is $\mathcal{A}_C(\phi) = \mathcal{A}[y_B + \rho \sin\theta,\, x_B + \rho\cos\theta]$, where $[\cdot,\,\cdot]$ denotes the translation function of an image. The binary was coarsely centered in a 17×17 pixel fitting region that defines the reference origin. The PSF was centered in a square fitting region of area that was ten pixels larger on all sides to ensure that any plausible shift of the PSF would populate the entire fitting region with data. The residuals between the data and the model is $R \equiv \mathcal{D} - \alpha_B\mathcal{A}_B(\phi) - \alpha_C\mathcal{A}_C(\phi)$.

The variance images of $\mathcal{A}_B$, $\mathcal{A}_C$, and $\mathcal{D}$ are propagated similarly, and are denoted σ_B^2, σ_C^2, and $\sigma_\mathcal{D}^2$. The uncorrelated uncertainty vector is $\sigma^2(\phi) = \sigma_\mathcal{D}^2 + \alpha_B^2\sigma_B^2 + \alpha_C^2\sigma_C^2$, which is converted into the covariance matrix C_ℓ using Equation 3.1. In principle, variance is not linear and therefore σ_B^2 and σ_C^2 cannot be interpolated simply by this translation function. However, the contribution of the PSF variance scaled by the square of the flux ratio already acts as a small perturbation of the variance image of the binary data. At the measured spatial correlation lengths, ℓ, the contribution of the covariance terms is even higher order and therefore neglected. That being said, C_ℓ is still highly nonlinear in ϕ and therefore this

problem is not ideal for generalized least square estimators.

Bayes' Theorem is used to write the posterior probability for ϕ and ℓ given $\mathcal{D}$ as, $\mathcal{P}(\phi, \ell|\mathcal{D}) \propto \mathcal{L}(\mathcal{D}|\phi, \ell)\mathcal{P}(\phi, \ell)$. To quantify the probability of the data conditioned on the model, we adopted a multivariate Gaussian likelihood function.

$$-2\ln\mathcal{L}(\mathcal{D}|\phi,\ell) = R^T\, C_\ell^{-1}\, R + \ln|C_\ell| + N_{\rm pix}\ln 2\pi \tag{3.3}$$

We employ a uniform, bounded priors $\mathcal{P}(\phi, \ell)$. The bounds exclude PSF shifts off the fitting region, negative separations ρ of the PSFs or $\theta \pm \pi$ (corresponding to y_B, x_B instead describing the position of HD 130948C), and extremely large or small α_B and α_C. Spatial correlation lengths are positive-definite and bounded above by the size of the fitting region.

We used `emcee` to sample the posterior distribution for each wavelength slice independently. We initialized 100 walkers with a guess ϕ vector plus Gaussian noise at an amplitude of $\phi \times 10^{-4}$. The MCMC sampler was run for 1000 steps after 1000 burn-in steps for each wavelength. The matrix inversion, multiplication and determinant of the Hermitian, positive-definite covariance matrix was calculated using the Cholesky decomposition to take advantage of numerical stability.

The resulting posterior distributions at each wavelength were marginalized over position, contrast and spatial correlation length terms, and combined jointly to calculate the median values for position angle and separation across all wavelengths, denoted θ^* and ρ^*. The plate scale error of 0.1 mas/spaxel was prop-

agated with Monte Carlo when converting the separation in spaxels to angular separation in mas. The standard deviations σ_{θ^*} and σ_{ρ^*} were calculated from the joint distribution assuming critical Nyquist sampling. This assumption is supported in Section 3.5.1.1. The values adopted for position angle and separation are $\theta^* = 137.0 \pm 0.2°$ and $\rho^* = 107.8 \pm 0.3$ mas, respectively.

The second step uses the same uniform, bounded priors $\mathcal{P}(\phi)$ from the first step, except for position angle and separation. The prior for position angle and separation are updated to be $\mathcal{P}(\theta) = \mathcal{N}[\theta; \theta^*, \sigma^2_{\theta^*}]$ and $\mathcal{P}(\rho) = \mathcal{N}[\rho; \rho^*, \sigma^2_{\rho^*}]$. The posterior distribution was sampled again for each wavelength under the same conditions stated before.

The correlations evident in Figure 3.4 manifest as a weak degeneracy between position of the brown dwarfs and flux ratios with respect to the PSF: the model binary built from two shifted PSFs will "exchange" flux when they are mislocated. A precision astrometric solution or L-band flux ratios of the brown dwarfs would be necessary to break this degeneracy (with more assumptions). Without such information, we do not probe this degeneracy further.

Chapter 4

End-to-end Simulation of SCALES

Adapted from

End-to-end Simulation of the SCALES Integral Field Spectrograph

Z. W. Briesemeister, S. Sallum, A. I. J. Skemer, R. D. Stelter, P. Hinz,

and T. D. Brandt

Proceedings of the SPIE, Volume 11447, id. 114474Z 13 pp. (2020)

DOI: 10.1117/12.2562143,

Abstract

We present end-to-end simulations of SCALES, the third generation thermal-infrared diffraction limited imager and low/med-resolution integral field spectrograph (IFS) being designed for Keck. The 2-5 micron sensitivity of SCALES enables detection and characterization of a wide variety of exoplanets, including exoplanets detected through long-baseline astrometry, radial-velocity planets on wide orbits, accreting protoplanets in nearby star-forming regions, and reflected-light planets around the nearest stars. The simulation goal is to generate high-fidelity mock data to assess the scientific capabilities of the SCALES instrument at current and future design stages. The simulation processes arbitrary-resolution input intensity fields with a proposed observation pattern into an entire mock dataset of raw detector read-out lenslet-based IFS frames with calibrations and metadata, which are then reduced by the IFS data reduction pipeline to be analyzed by the user.

4.1 Introduction

The current generation of high-contrast coronagraph-assisted imagers and (integral field) spectrometers have succeeded in identifying and characterizing a population of massive, wide-period exoplanets by bulk, chemical, and atmospheric

properties in exceptional detail. While this limited population has been an excellent probe of this specific region of parameter space, an extended exploration would access the outcomes of various planet formation and migration scenarios. The goal of accessing a larger region of parameter space of possible exoplanets motivates the development of new instruments that improve on previous designs. This includes use of advanced adaptive optics combined with coronagraphic integral field spectroscopy mounted on large/extremely-large telescopes that extends to longer wavelengths (2-5 μm), where self-luminous exoplanets have greatest contrast with their host star. These longer wavelengths have been otherwise inaccessible given the high background radiation, detector sensitivity and instrument design.

The precursor instrument Arizona Lenslets for Exoplanet Spectroscopy (Skemer et al., 2015) (ALES) in the Large Binocular Telescope Interferometer (LBTI) (Hinz et al., 2008a, 2012, 2014) has provided the first spatially-resolved thermal-infrared spectral characterization of substellar companions (Briesemeister et al., 2019; Stone et al., 2020), and Santa Cruz Array of Lenslets for Exoplanet Spectroscopy (SCALES) will improve on ALES in optomechanical design and sensitivity. While ALES bridges this technological (Hinz et al., 2018; Stone et al., 2018b; Skemer et al., 2018b) and scientific gap, the dedicated instrument SCALES vastly improves upon stability and sensitivity of the nascent technology in order to pro-

vide 10-m class diffraction-limited thermal infrared low-/med-resolution spectra and imaging. This paper describes the end-to-end simulation of SCALES, accompanied by the implementation of the data reduction and analysis tools repurposed and improved upon from the ALES data reduction pipeline (Briesemeister et al., 2018).

4.2 SCALES at a Glance

SCALES comprises a low-resolution integral field spectrograph and a medium resolution integral field spectrograph that share coronagraphic foreoptics transmissive from 2-5 μm, and a 1-5 μm imager. A complete description of the current optomechanics of SCALES is presented in these proceedings by Stelter et al. in paper #11447-110. Figure 4.1 depicts the schematic of the SCALES optical layout for the three modes.

For the low-resolution mode, f/15 light from Keck AO enters the cryogenic dewar through a CaFl entrance window and is relayed through a fixed cold-stop followed by a linear slide containing focal plane vector-vortex coronagraphs optimized for K, L, and M bands. The light is magnified by 22.8 by an off-axis-ellipse with an intermediate pupil plane that contains Lyot stops, pupil apodizers and non-redundant pupil masks. The light is relayed to the 108×108 square lenslet array, where the 341 micron, f/8 square lenslets sample the $2.15'' \times 2.15''$ field

with a lenslet pitch of $0.02'' \times 0.02''$ to Nyquist sample at 2.0 μm. A two-element collimator produces a pupil plane at the disperser wheel, which contains reflective double-pass LiF prism with gold coating on the second surface for each band-pass. A two-element camera images the spectra onto the Teledyne HAWAII-2RG (Beletic et al., 2008) detector.

For the med-resolution mode, a piezo-controlled tip-tilt stage directs the astrophysical scene to a subarray of 18×18 spaxels on the side of the lenslet array at the same magnification ($0.36'' \times 0.36''$ field of view with a lenslet pitch of $0.02'' \times 0.02''$). The slicer system rearranges the lenslet pupil images back into the spectrograph as a single pseudo-slit where a pupil forms at gratings designed to disperse the spectra without order overlap, and imaged onto the detector similarly.

The imager will pick light off from the Lyot stop wheel towards a dedicated camera and detector system with a field of view of $20'' \times 20''$ at a plate scale of $0.01'' \times 0.01''$. The imager has NIRC2-like filters.

4.3 Simulation Architecture

SCALES is currently in the preliminary design stage. The simulation tool is tailored towards investigating the impact of optomechanical design choices on the fiducial science cases for SCALES, enumerated in paper #11447-110. Simulation of the outputs from instruments is necessary to predict their performance.

SCALES Spectral Summary			
	Wavelengths	Band	Resolution
Low-Resolution Spectroscopy	2.0-3.7 μm	water ice	~ 60
	2.0-2.4 μm	K Band	~ 200
	2.0-5.0 μm	SEDs	~ 35
	2.9-4.15 μm	L band	~ 80
	3.1-3.5 μm	CH_4 + PAH	~ 250
	4.5-5.2 μm	M band	~ 140
Medium-Resolution Spectroscopy	2.0-2.4 μm	K band	~ 5000
	2.9-4.15 μm	L band	~ 3500
	4.5-5.2 μm	M band	~ 7000

Table 4.1: Wavelength bands with filters in SCALES for the low-resolution and medium-resolution integral field spectrographs.

The fidelity of such simulations is limited by the reproduction of the physics and astrophysics of the observation process, optomechanical design, and reduction prescription that can be interpreted in finite computation time.

For these SCALES simulations, astrophysical fields are provided by the user in the form of a spatiospectral data cube in mJy/px/λ at higher spatial and spectral resolution than the instrument, along with metadata, including sampling rate, position, date/time of observation, duration, and atmospheric conditions. The simulation will generate a mock dataset from an entire low-/med-resolution IFU observation in detector readout units and/or file facsimiles. The simulations for the imager are not currently included. This tool was written in Python. In this section, we describe the models used to reproduce the physical processes of

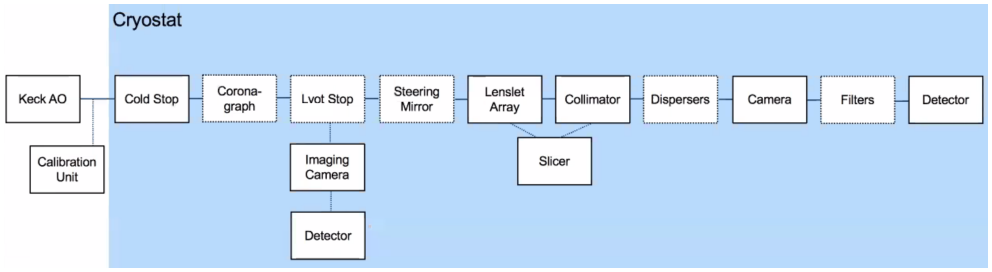

Figure 4.1: Schematic of the SCALES optical layout. Keck AO delivers f/15 light through the entrance window. For the imager, light is relayed to a dedicated detector. For the spectrograph, the light passes through the focal plane coronagraph and Lyot stop, forming an image at the lenslet array. The low-resolution mode comprises the lenslet array, collimator, disperser and camera. The med-resolution mode selects a 18×18 spaxel region from the lenslet array and relays the light through an image slicer that reorients the spectra in a pseudoslit that is then dispersed and imaged on the detector. The calibration unit is described here (Briesemeister et al., 2018).

imaging spectroscopy in SCALES. Figure 4.2 depicts how the optomechanics from Figure 4.1 are translated into software.

4.3.1 Adaptive Optics Simulation

While the point-spread function of the instrument is an important component to reproduce with fidelity, the nature of the point-spread function at the focal planes of the imager and lenslet-array remains a point of active development.

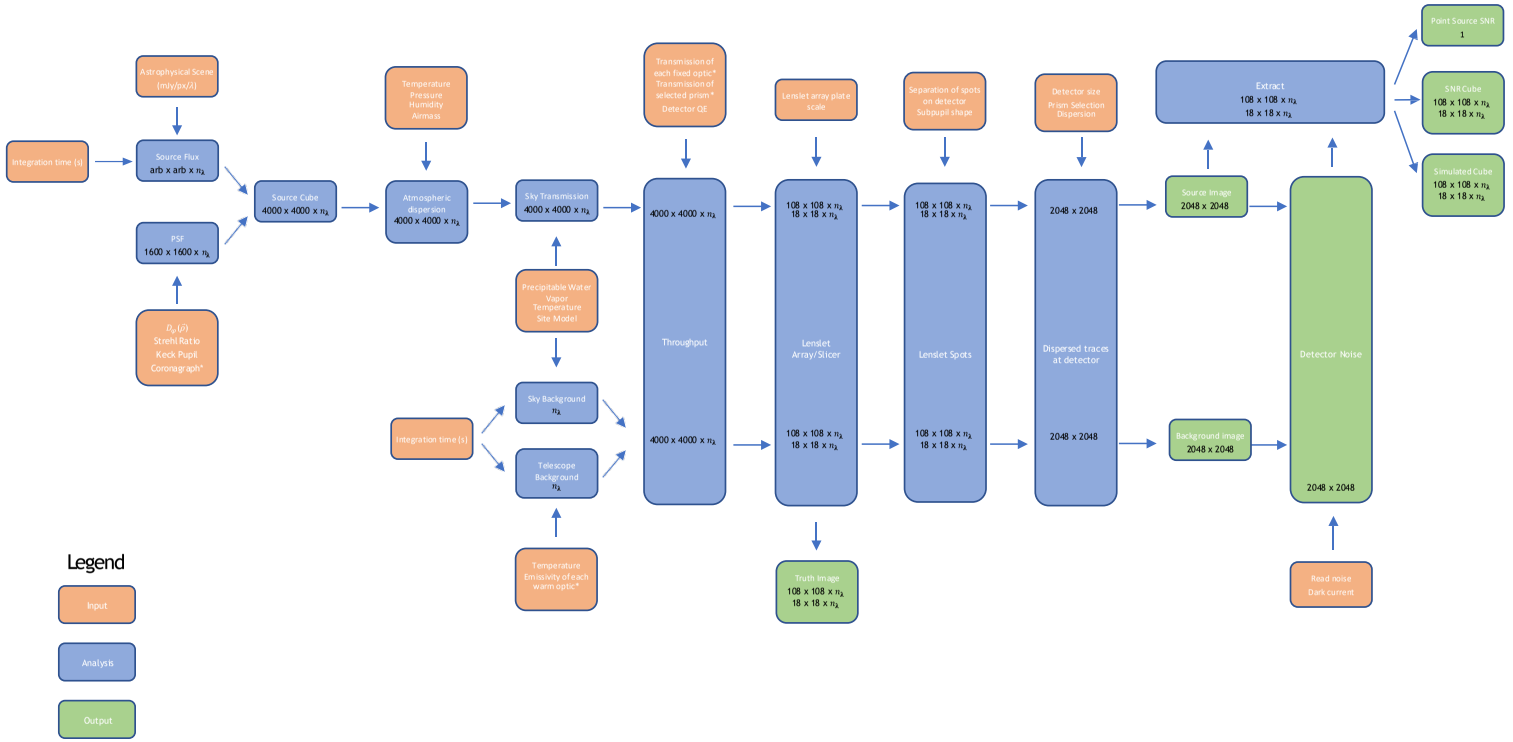

Figure 4.2: A schematic of the forward-direction of the simulation necessary to reproduce the astrophysics, tellurics and hardware of SCALES observations.

The large wavelength sensitivity merits having three focal plane coronagraphs optimized to K, L, and M bands, respectively, which are also being developed and are not implemented in the simulation yet.

Any astrophysical intensity field observed from the ground is modulated by the Earth's atmosphere and can be partially spatiotemporally corrected by an adaptive optics system. Simulating one long exposure sampling thousands of correlated phase screens is computationally prohibitive. Our approach is to use a simple analytical model to express images of finite exposure times, eschewing the time-correlation of phase screens in favor of faster computation. Given a user-chosen (default von-Kármán, $L_0 = 8$ m) structure function of residual phase, $D_\phi(\vec{\rho})$, a point spread function averaged over exposure-time T for turbulence lifetime τ will have intensity $\langle I \rangle_T = \mathbb{E}(I) + \sigma$, such that $var(\sigma) = \frac{\tau}{T}(\mathbb{E}(I^2) - \mathbb{E}(I)^2)$. The intensity term I is expressed in terms of the associated optical transfer function (OTF), $\hat{h}(\vec{\rho}/\lambda) = \hat{h}_A(\vec{\rho}/\lambda)\hat{h}_T(\vec{\rho}/\lambda)$, for atmosphere OTF $\hat{h}_T(\vec{\rho}/\lambda) = exp(-\frac{1}{2}D_\phi(\vec{\rho}))$, telescope OTF $\hat{h}_T(\vec{\rho}/\lambda) \propto \iint P(\vec{r})P(\vec{r}+\vec{\rho})d\vec{r}$, and P entrance pupil transmission function. Individual point spread functions are drawn from this model for each frame.

The final PSF is obtained by multiplying the OTF due to high order effects with ideal correction on low order modes, from low order wavefront errors, and due to uncertainties from the optical system and instrument set by design requirements

of SCALES. The final OTF is tuned such that the Strehl ratio at 3.7 μm is 0.85 to reproduce Keck AO-like optical quality.

Given the extended wavelength coverage of SCALES, departure from zenith will result in atmospheric deflection of the position of a point-source as a function of wavelength. This uncorrected deflection is simulated by affine transformation along the direction perpendicular to the horizon with magnitude associated with a given temperature, pressure, relative humidity and airmass (Mathar, 2007). While the effect of relative astrometry is suppressed by the integral field spectrograph, the offset has important implications on the hardware and observation modes we employ.

4.3.2 Transmission and Background

The column of atmosphere in the direction of the source region will modulate the transmission of astrophysical photons from the source, modeled by the theoretical sky background available from the Gemini observatory calculated with the atmospheric model ATRAN (Lord, 1992).

We use the theoretical sky background available from the Gemini Observatory, which includes the sky transmission calculated from with the atmospheric model ATRAN (Lord, 1992), a 273 K continuum to simulate the sky. The telescope background and AO system background are modeled as blackbodies at 273 K and

their emissivity in the thermal infrared is currently roughly estimated at $\sim 35\%$.

Each gold-coated mirror and transmissive optic is modelled using emissivities and transmission profiles from the manufacturer, respectively. The lenslet array is photolithography-etched silicon with imperfections on the sub-micrometer scale, which is ignored. The transmission of the lenslet array is estimated at 98%.

4.3.3 Simulating the Spectrographs

At the focal plane of each lenslet, an image of the exit lenslet pupil will form, comprising of all the light from the image incident to the spatial extent of the lenslet. In the optical design we place a pinhole grid of circles at a distance optimized by Zemax Physical Optics from the lens to suppress the square diffraction effects of each lenslet (Figure 4.3). We determined with Zemax that the pinhole grid is preferred over not having one due to the dispersion direction and spectral resolution. The lenslet/pinhole PSF is calculated at each wavelength, and is scaled in amplitude by the input intensity.

In the case of the low-resolution spectrograph, the lenslet pupil images are then dispersed without spatial and spectral overlap, which forms images of dispersed lenslet pupils. For the med-resolution spectrograph, an 18×18 subset of lenslets are picked off and the lenslet pupil images are reordered by offset flat mirrors to the reflective disperser and relayed onto the detector.

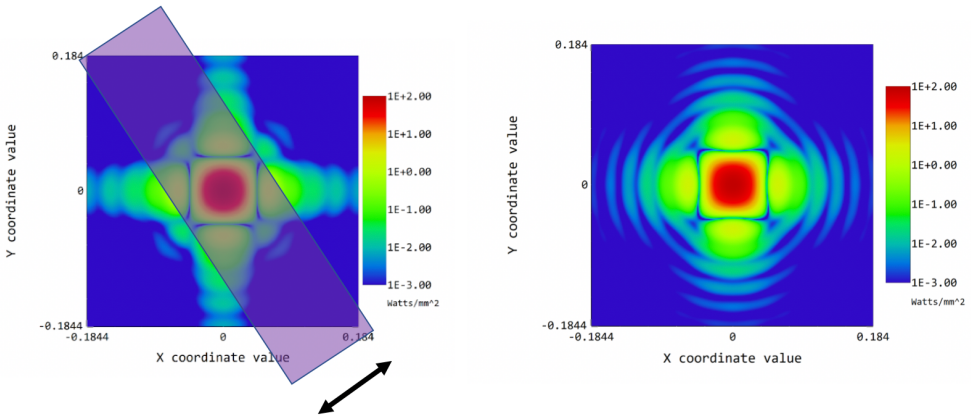

Figure 4.3: Left: An image of the 5.0 micron lenslet pupil caused by diffraction comprising the flux incident on f/8 lenslet of the lenslet array. The purple box denotes the direction of dispersion for low-resolution mode. Right: An image of the 5.0 micron lenslet pupil caused by diffraction of the square f/8 lenslet and the pinhole placed at the geometric focus of the lens. The pinhole throughput is $\sim 83\%$ at 5 microns.

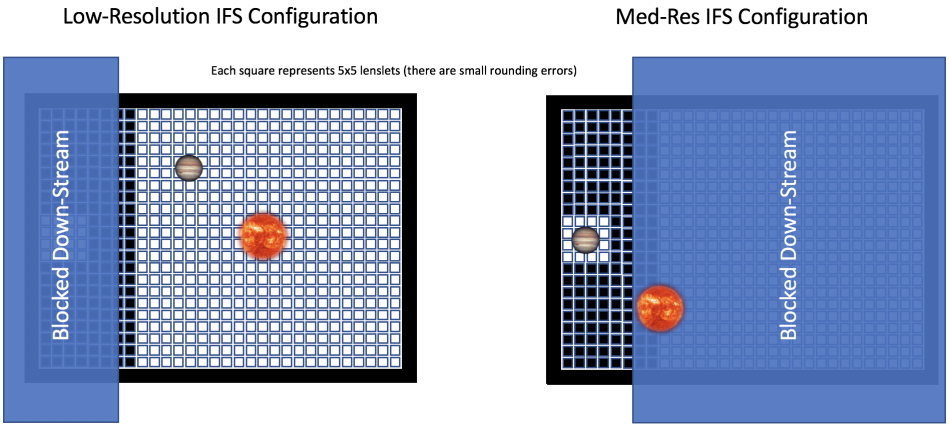

Figure 4.4: Left: A cartoon for a star/exoplanet scene incident on SCALES at the low-resolution integral field spectrograph mode. The region of lenslets relayed to the disperser and detector are white in this image and decimated at a rate of 5 pixels. Right: A piezo-controlled mirror translates the star/exoplanet system in the med-resolution integral field spectograph mode, such that the exoplanet is incident on the active spaxels and the star is obstructed. The active spaxels are dispersed following the slicer pseudoslit to the detector in an array of 18×18 spectra containing spatiospectral information.

The mechanical distinction of the med-resolution mode compared to the low-resolution mode is depicted in Figure 4.4. In low-resolution mode, the deviations of the grid of lenslet pupil images from rectilinear are characterized in the optomechanical design, and are applied as a 2D-polynomial shift that the data reduction pipeline is agnostic to. In med-resolution mode, predetermined shifts, set by the optomechanical design of the slicer, are applied to each spectrum.

Dispersion for low-resolution mode is performed by reflective double-pass LiF prism with gold-coated back and anti-reflection coated front tuned for each band pass. These prisms haven't been designed yet, so a linear dispersion profile is used to calculate the position at which monochromatic PSFs are imaged onto the detector. The final science image without noise comprises contributions of propagated monochromatic light at each wavelength, summed and binned at the detector pixel rate.

Dispersion for med-resolution mode is performed by gratings tuned for K, L, and M bands. The position of monochromatic light is determined by the image slicer and a linear dispersion profile of the grating (as the gratings also have not been designed yet). The final science image without noise is then the contributions of propagated monochromatic light at each wavelength, summed and binned at the detector pixel rate.

4.3.4 Detector Noise

The detector for SCALES is a 2048×2048 pixel Teledyne HAWAII-2RG detector tuned to 5.3 micron cutoff. Generating high-fidelity realizations of detector noise requires complex modelling of correlated stationary and non-stationary noise components caused by solid-state physics. In order to approach fidelity, we modified the noise generator from (Rausher 2015) (Rauscher, 2015) to apply to various readout methods and digitization processes. These modifications have been tested to reproduce the LBT/LMIRCam (Skrutskie et al., 2010; Leisenring et al., 2012) H2RG detector noise.

For both modes, realizations of detector noise are added to the science frames. Calibration frames are also propagated through the same process. Apart from flux calibration, the calibration frames are necessary for the actual extraction step for the least-squares and sparse matrix extraction methods.

4.3.5 Data Reduction Pipeline

In order to convert the simulated data in low-resolution mode to data cubes, the simulation uses `MEAD` (Briesemeister et al., 2018) to facilitate the translation of raw detector readout frames and metadata into data cubes containing spatial and spectral information. This simulation tool has been extensively used to test the implementations of aperture, optimal (Horne, 1986), least-squares (Brandt

et al., 2017; Draper et al., 2014), sparse matrix extraction of the spectra into data cubes, and we are exploring the efficiency of other data structures to optimize this extraction. Figure 4.5 depicts raw simulated data, the recovered images and injected/recovered spectra for a short integration of an A0 star at 10pc in L band.

The med-resolution mode required development of a new module for `MEAD`, as the slicer pseudoslit reformats the dispersed 18×18 lenslet pupil images in a fundamentally different way than the lenslet array alone. The selected order of 324 spectra are separated by ~ 6 pixels and have the dynamic range limited by the detector layout of 2048 pixels, slicer design, and disperser profiles. These spectra are extracted with any of the four extraction methods previously implemented for the low-resolution mode for these longer spectra. This early data reduction pipeline for the med-resolution modes will drive investigation towards a more robust pipeline in the future.

4.4 Simulation and Design

The simultaneous development of instrument and instrument simulation has many engineering and design benefits. The simulation has been used to quantify requirements set by the fiducial science cases and to test the consequences of update to the design of the instrument on meeting these requirements.

Background radiation sets unique limitations on the science capabilities of

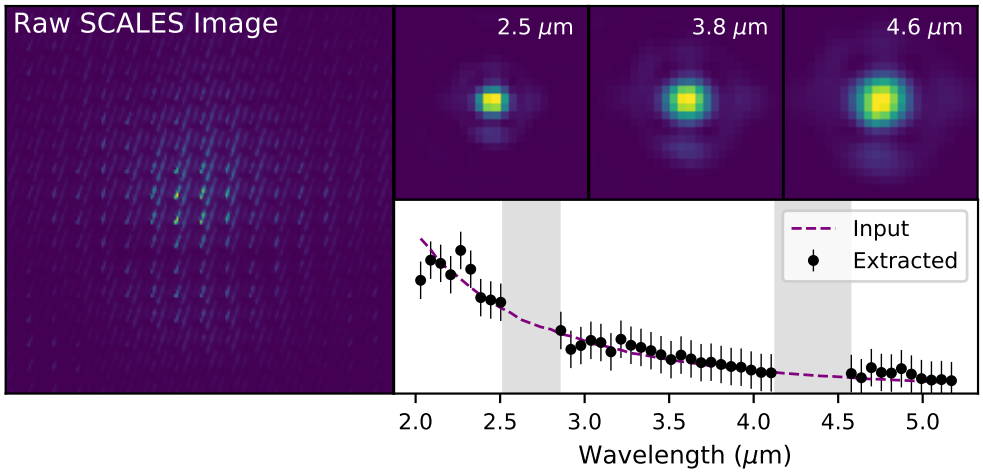

Figure 4.5: Left: A zoomed-in single sky-subtracted data frame produce in low-resolution simulation of an A0 star at 10pc with the 2-5μm filter mode. The color stretch is square root in order to depict more spaxels. Right/Top: The extracted point spread function for the image at 2.5μm, 3.8μm, and 4.6μm, respectively. The color stretch is linear. Right/Bottom: The input and extracted spectrum with errors from 4 seconds on target and 4 seconds on sky performed with aperture extraction. The grey shading denote regions of high telluric absorption. Deviations in K band are driven by red-leaks, warranting use of an informed extraction (least-squares) over aperture extraction.

SCALES. The issue manifests most notably in the 2-5 μm filter in low-resolution mode, where the thermal background at the red end of the filter is orders of magnitude brighter than the thermal background at the blue end. For the desired fill factor of the detector, the spectra are limited in their separation, and the bright red ends of spectra neighbor the blue ends of other spectra. These red leaks are an inherent source of noise that would limit the usefulness of broad filters without appropriate filter design. This requirement has been investigated with the simulation and used to set the requirements on the transmission of light at the red end of this filter.

An incomplete list of the other uses of the simulation include the consequences of deviation from polynomial dispersion, deviation from rectilinear grid of lenslet pupil images at the focal plane, stability/reproducibility requirements of the disperser elements and other wheels, material transmission, drift, optical quality, etc. on target sources that we have identified as fiducial science cases for SCALES.

Designing appropriate observation patterns is also relevant to maximize astrophysical photons while mitigating the thermal background at these wavelengths. The small field of view of the med-resolution mode when observing high-contrast targets necessitates an informed observation pattern to obtain calibrations, sky frames, dark frames and on target frames in a sky-rotating-frame, all of which we are using this tool to model and investigate.

4.5 Astrophysics with SCALES

The unique capabilities of SCALES opens an otherwise inaccessible parameter space of spatiospectral heterogeneity in astrophysics explored at small angular separation. SCALES is particularly capable of accessing unexplored regions of parameter space in which many detectable exoplanets are expected to exist. This is facilitated by combining thermal infrared (2-5 μm) sensitivity in the region of greatest exoplanet-star contrast (Skemer et al., 2014) and integral field spectroscopy for distinguishing exoplanets from residual diffracted starlight.

The synergy of astrometric detection with *Gaia* and *WFIRST*-WFI and direct detection of exoplanets with SCALES has been identified with this simulation (Brandt et al., 2019a). Gaia's extended 9-year survey is expected to yield a catalog of 70,000 exoplanets (Perryman et al., 2014). We predict 9 exoplanets ($<13M_{jup}$) and 67 brown dwarfs ($>13M_{jup}$) will be accessible to direct imaging with thermal emission by SCALES when initially detected through astrometry with *Gaia* (Brandt et al., 2019a). With a single position measure by *WFIRST*-WFI in 2030, this expands to 19 exoplanets and 144 brown dwarfs. These complementary measurements are sensitive to stellar mass estimates (Nielsen et al., 2014) down to $\sim$ 300K, where water clouds manifest in M-band spectra (Skemer et al., 2016a). For previously-discovered directly-imaged planetary-mass or near-planetary-mass companions (Bowler, 2016), SCALES will complement near-infrared spectroscopy

with thermal infrared spectroscopy to improve estimation of important quantities for exoplanets, like luminosities, masses, molecular abundances (e.g. CO, CO_2, H_2O, CH_4), temperatures, and cloud coverage.

For practical reasons, exoplanet imaging surveys have focused on young exoplanetary systems, where stellar emission is set by core mean molecular weight near pure hydrogen and exoplanets passively radiate residual heat of formation (Biller et al., 2007; Vigan et al., 2012). However, accretion shocks are efficient at radiating away energy in planets formed via core accretion, resulting in a population of exoplanets with relatively cold initial conditions (< 600K). Near-infrared integral field spectrographs are not sensitive to such "cold-start" planets (Stone et al., 2018c), which have only imaged planets as cold as $\sim 600 - 750$K (Macintosh et al., 2015b). SCALES is sensitive to the thermal emission of this hypothetical population, probing the old and cold exoplanets.

In protoplanetary systems, it is possible to estimate mass accretion and $M_p M_d$ when young planets are embedded in natal discs (Sallum et al., 2016; Currie et al., 2019). Thermal infrared integral field spectroscopy would be particularly useful for distinguishing scattered light of circumstellar disks and regions of bright hydrogen-gas shocks consistent with protoplanets, as measured by the Br-γ line. SCALES also uniquely opens the capacity to map circumstellar disks in water ice (Podio et al., 2013) and PAH emission. The simulation package is deployed with

the previous examples included.

SCALES integral field spectroscopy also opens a unique parameter space in solar system, galactic and extragalactic astronomy. The contribution of background emission is diminished by dispersion, providing uniquely sensitive measurements of extended sources of thermal/redshifted emission. For example, volcanic eruptions and the extent of their lava fields can be investigated on Io (See Section 5.2), and carbon-based weather can be mapped on Titan. SCALES is sensitive to Brackett-, Pfund-, and CO-line mapping in bright young supernovae. The carbonaceous dust in unshocked ejecta of nearby remnants is sensitive to dust formation/destruction (Kotak et al., 2005). SCALES can also explore spatially-resolved nuclear/star-forming regions in nearby bright galaxies for characterization from PAH emission in dusty AGN tori (Marco and Brooks, 2003) and hot dust emission.

4.5.1 HR 8799-like System

Lenslet-based integral field spectrographs are uniquely adept at imaging spectroscopy of exoplanetary systems because the optical distortion is not amplified when subsampling the focal plane with the lenslet array. The design of having the image slicer component downstream of the lenslet array also mitigates this problem that it would otherwise have, enabling high-spatial resolution thermal infrared integral field spectroscopy at low- and med- spectral resolutions.

Point sources were arrayed in the input field to be reminiscent of the HR 8799 system to represent an A0 star accompanied by three companions at 1000K, 1400K and 900K, each with radius 1 R_J, log(g) = 4.0, and distance = 40.9 pc. The PHOENIX atmospheric code was used to calculate the model spectra (Barman et al., 2011). The b component of the real system has no analog here, as is not contained within the field of view of the low-resolution integral field spectrograph when the other exoplanets are required to be in every image.

Two hours of integration were simulated with positions and sky rotation set by starting when HR 8799 was nearest zenith. We used a constant phase screen and no coronagraph for internal testing purposes, and angular differential imaging was used to remove the point spread function of the primary. These observations are background limited for NIRC2 (with the possible exception of HR 8799 e) so this is a reasonable assumption until we implement the coronagraph in the code. Three representative slices of the data cube and the input/output spectra of this simulation are shown in Figure 4.6.

For the med-resolution simulation, we look at a point source with an SED representative of HR 8799c. The small field of view of this mode requires an observation pattern that nods between the target, blank sky, and a PSF calibrator (usually the primary star). Two hours of total integration time following this pattern were simulated with positions and sky rotation set by starting when HR

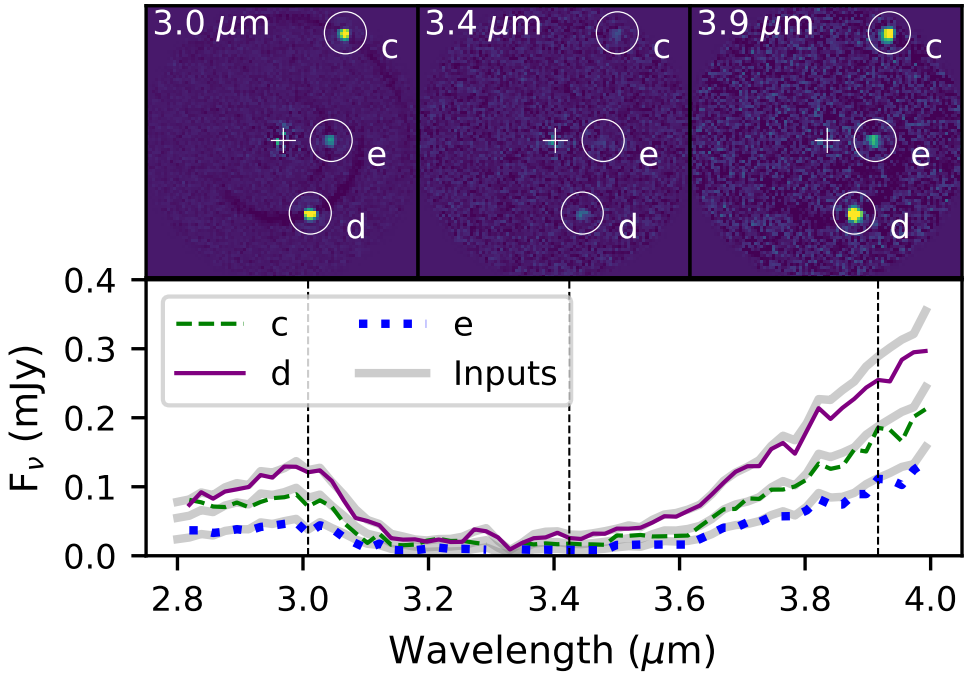

Figure 4.6: Top: Simulations of the 3.0, 3.4 and 3.9 micron images of a 2-hr integration of a HR 8799-like system at L band, processed with a naive, non-aggressive application of full-frame Angular Differential Imaging. Bottom: The input and recovered spectra of the HR 8799cde-like exoplanets from the same simulation at L band

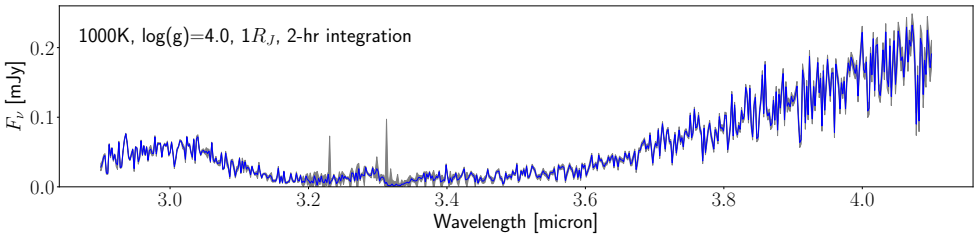

Figure 4.7: The recovered spectrum of the analog of HR 8799c with error bars using the med-resolution mode in L band for a 2-hr integration. The region near 3.3 microns has lower SNR due to both low telluric transmission and low astrophysical emission. Given the size of spectral resolution elements and linear dispersion model, there are 600 wavelength bins depicted here.

8799 was nearest zenith (irrespective of whether that is consistent with daytime for the real HR 8799). The PSF was assumed not to translate due to pointing errors. The resulting recovered spectrum is depicted in Figure 4.7.

4.5.2 Io Volcanoes

SCALES will monitor the locations, temperature, and extents of volcanoes on Io. For large eruptions, SCALES can map the extent of thermally active fields extending across the disc of Io while they cool. We assess SCALES's ability to recover the temperature of volcanoes on the surface of Io with a simple model for its surface. This model includes a uniform disk emitting isotropically with volcanoes as extended sources emitting at various temperatures enumerated in (de

Kleer et al., 2017) to replicate lava fields as some volcanoes would be marginally resolved at the blue end of the 2-5 μm band. A more sophisticated model including Io's rotation as a uniform sphere emitting isotropically could be done in the future.

We demonstrate the use of the 2-5 μm filter: simultaneous coverage of a significant portion of the spectral energy distribution from thermal emission of a volcano lava field. With one filter, we can determine the temperature of volcanoes (Figure 4.8).

4.6 Summary

We presented the end-to-end simulation of the low-/med-resolution integral field spectrographs for SCALES, the dedicated high contrast IFU operating from 2-5 μm at R$\sim$ 100 $-$ 10000. Simultaneous development of the data reduction pipeline, simulation and the instrument itself enables exploration of consequences of design decisions and the capabilities of the instrument for delivering unique integral field spectrograph data.

Acknowledgments

We gratefully acknowledge the support of the Heising-Simons Foundation through grant #2019-1697. ZWB is supported by the National Science Foun-

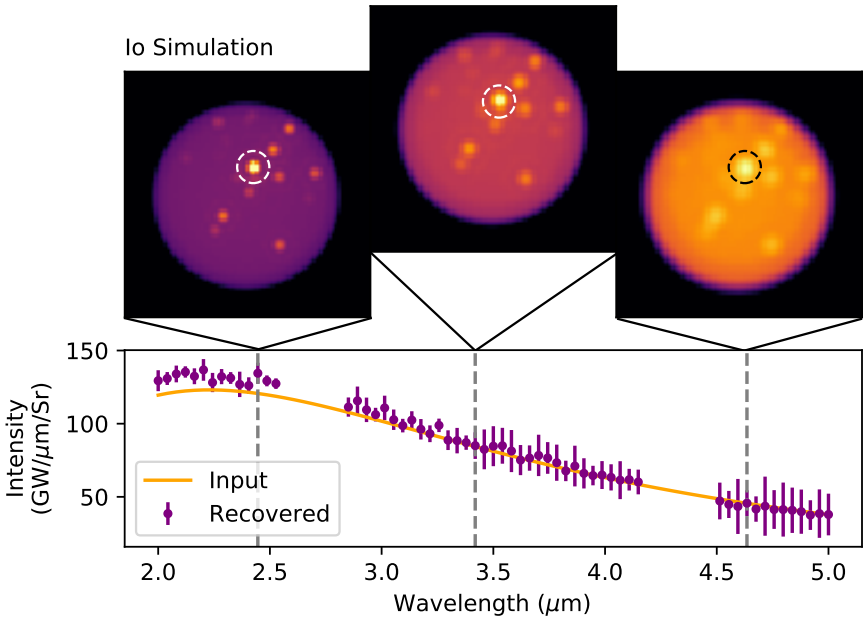

Figure 4.8: Top: Simulations of the 2.4, 3.4 and 4.6 micron images of a 2-hr integration of our Io model at 2-5 μm band, processed with a naive, non-aggressive application of full-frame Angular Differential Imaging. Bottom: The input and recovered spectra of the Loki Patera-like volcano from the same simulation at 2-5 μm band. Note the excess intensity in K band is caused by the volcano being marginally resolved and our extraction not accounting for this. The gaps in the spectrum are regions of high telluric absorption.

dation Graduate Research Fellowship under Grant No. 1842400. This paper is based on work funded by NSF Grant 1608834.

Chapter 5

Information Content Approach to Trade Studies for SCALES

Adapted from

Information Content Approach to Trade Studies for SCALES

Z. W. Briesemeister, S. Sallum, A. I. J. Skemer, and N. Batalha

Proceedings of the SPIE, Volume 11823, id. 1182308 7 pp. (2021)

DOI: 10.1117/12.2594880, ©SPIE. Reproduced with permission

Abstract

The advantage of having a high-fidelity instrument simulation tool developed in tandem with novel instrumentation is having the ability to investigate, in isolation and in combination, the wide parameter space set by the instrument design. SCALES, the third generation thermal-infrared diffraction limited imager and low/med-resolution integral field spectrograph being designed for Keck, is an instrument unique in design in order to optimize for its driving science case of direct detection and characterization of thermal emission from cold exoplanets. This warranted an end-to-end simulation tool that systematically produces realistic mock data from SCALES to probe the recovery of injected signals under changes in instrument design parameters. In this paper, we quantify optomechanical tolerance and detector electronic requirements set by the fiducial science cases using information content analysis, and test the consequences of updates to the design of the instrument on meeting these requirements.

5.1 Introduction

The Santa Cruz Array of Lenslets for Exoplanet Spectroscopy (SCALES) instrument will deliver 10-m class diffraction-limited thermal infrared low-/med-resolution spectra and imaging of low mass companions, cold brown dwarfs, cir-

cumstellar discs, and more. During the proposal stage, we identified the high-level requirements and overall specifications that lead all the design stages for instrument subsystems (Stelter et al., 2020). These fiducial science targets drive the optomechanical and electrical design decisions for each subsystem, defining requirements, modes of operation, relative position, orientation, quality, and general tolerances. Tolerances have a critical role in the manufacturing of instruments. Ultimately, the manufacturing accuracy of the instrument sets the limits of observability, and more importantly, characterizability of exoplanet atmospheres. This motivates our current study, in which we investigate how deviations in the optomechanics and electronics of the SCALES instrument will affect our ability to accurately characterize the atmospheres of exoplanets.

SCALES is equipped with low- and medium-resolution spectroscopic modes across six different wavelength ranges and nine different spectral resolving powers that can all be used for spectroscopy of exoplanets. In this paper, we seek to identify what the limits of these modes will be, in terms of exoplanet characterization, if the instrument were to deviate from the ideal design of SCALES. The most rigorous way of accomplishing this is through atmospheric retrieval, which links atmospheric models to the data in a Bayesian framework (Madhusudhan, 2018; Barstow and Heng, 2020). While robust in its ability to derive non-Gaussian posterior distributions on atmospheric parameters of interest, it is computationally

intractable given the diverse instrument phase space of SCALES and the possible atmospheric parameter space of known exoplanets. Instead, we treat this as an information content theory problem (Shannon and Weaver, 1949), where one (or multiple) elements in an atmosphere and instrument model is perturbed. This allows determination of SCALES' ability to constrain physical atmospheric parameters (e.g. $[M/H]$, C/O) as a function of various observational setups using "information loss", measured in bits, as a quantitative metric. We will model the effects of these perturbations with the SCALES simulation tool (Briesemeister et al., 2020).

One might expect that if you perturb an optical element enough, the spectrograph simply will not work. So in between working and not working there is an extreme perturbation, such that no amount of exposure time would be sufficient to increase the information about model parameters with respect to priors. There is also a less extreme perturbation, such that you are limited by the amount of exposure time you can allocate to your target to gain sufficient information to satisfy fiducial science goals. This concept brings us to information content analysis, and restructures our investigation of tolerances in a way to answer the question: "Is the rate of information content per observation sufficient to satisfy the fiducial science case requirement for a given exposure time?"

5.2 Information Content

The methodology we used for assessing information content of atmospheric observables from the modes of SCALES is based on optimal estimation theory (Rodgers, 2000). This theory has been used recently in two studies for optimizing JWST observations (Batalha and Line, 2017; Howe et al., 2017), and in a broad range of Earth and Solar System studies. We direct readers to (Rodgers 2000) for an in-depth description of information content analysis, as well as the notation used here. A brief summary of salient features of the information content analysis is included here for completeness.

Information content H is broadly defined as the change in entropy S on making a measurement. In terms of probability distribution functions (PDFs) and Bayesian methods, it can be understood as the difference in entropy of PDF $P(\mathbf{x})$ and PDF $P(\mathbf{x}|\mathbf{y})$, where the state vector $\mathbf{x}$ describes the state of the atmosphere and the quantities which will be measured in order to retrieve $\mathbf{x}$ are represented by the measurement vector $\mathbf{y}$. In the case of SCALES, $\mathbf{y}$ is the spectrum measured. For our initial analysis, we simplify the state vector to be $\mathbf{x} = [T(P), [M/H], C/O, g]$, which neglects clouds. Here, $T(P)$ is the pressure-dependent temperature profile, $[M/H]$ is metallicity, C/O is the carbon-to-oxygen ratio, and g is the gravity. The information content $H = S[P(\mathbf{x})] - S[P(\mathbf{x}|\mathbf{y})]$ measured in bits describes the decrease in entropy of the probability that a certain state exists

following a measurement.

The relationship between the measurement and the atmospheric state $\mathbf{y} = \mathbf{F}(\mathbf{x})$ is highly non-linear and depends on the instrument and spectral extraction methods used. However, a Taylor expansion of the model around some reference state is adequate for appropriately small deviations. This linearization sets the Jacobian matrix $K_{ij} = \partial F_i(\mathbf{x})/\partial \mathbf{x_j}$ as the appropriate operator, describing how sensitive the model is to slight perturbations in each state vector parameter.

Under the assumption of Gaussian distributions, as done in (Rodgers 2000),

$$H = -\frac{1}{2} \ln |\hat{\mathbf{S}}^{-1} \mathbf{S_a}| \tag{5.1}$$

and

$$\hat{\mathbf{S}} = (\mathbf{K^T S_e^{-1} K} + \mathbf{S_a^{-1}})^{-1} \tag{5.2}$$

where $\hat{\mathbf{S}}$, $\mathbf{S_e}$ and $\mathbf{S_a}$ are the posterior error, data error and prior covariance of the state parameters, respectively. The quantification of information content relies on the construction of accurate Jacobian $\mathbf{K}$, and accurate estimation of prior and data error covariance. The parameter uncertainties are quantified in the diagonal elements of the posterior covariance matrix $\hat{\mathbf{S}}$.

5.3 Modeling & Retrieval Approach

5.3.1 Emission Spectra Models

We use the PICASO code that enables computation of reflected light, thermal and transmission spectroscopy for exoplanets and Brown Dwarfs (Batalha et al., 2019). For the analysis in this paper, we used self-consistent pressure-temperature profile from the Sonora 2018 model series for non-irradiated, substellar mass object (Marley et al., 2021). Given the temperature-pressure profile of the atmosphere and the elemental abundances parameterized with metallicity, $[M/H]$, and C/O, the model first computes the thermochemical equilibrium molecular mixing ratios (and mean molecular weight) using the publicly available Chemical Equilibrium with Applications code (CEA[1]) (McBride and Gordon, 1996). The thermochemically derived opacity relevant mixing ratio profiles (H_2O, CH_4, CO, CO_2, NH_3, H_2S, C_2H_2, HCN, TiO, VO, Na, K, FeH, H_2, He), temperature profile, and planet bulk parameters are then fed into a emission spectrum model.

5.3.2 SCALES Noise Models

Sufficient reproduction of the processes involved in astrophysical detection is necessary to calculate $\mathbf{K}$ and $\mathbf{S_e}$. To be explicit in our modelling, we enumerate these processes here.

[1]https://www.grc.nasa.gov/WWW/CEAWeb/

In the detector model, the sensor can be treated as an array of pixels that take an input (a number of photons) and transforms these values to an output (a digital value in analog-to-digital units, or ADU). In performing this transformation, various sources of noise are added to the signal so that, given a camera's output in ADU, we can only make probabilistic inferences about the actual number of photons impinging on it. The simplest model would depend on five free parameters: the quantum efficiency $\eta(\lambda)$ [e^-/γ], the read noise magnitude σ_r [e^-_{rms}], the dark current $\mu(T)$ [e^-/s], the sensitivity (amplification of the voltage in the pixel from the photoelectrons) K [ADU/ e^-], and the bit-depth of the camera k.

The noise generator of HxRG detectors from (Rauscher, 2015) identifies and implements non-white sources of noise, which are added to our detector model. A model of the linearity of LMIRCam was used as the model for linearity in the simulation. The electric field from the AO simulations are converted it into units of photons from the irradiance of the field using the magnitude of the time-averaged Poynting vector of a linearly-polarized electromagnetic wave in free space. Photon shot noise from the source and background are added. ADU are treated as discrete integer units. Finally, the effects of readout direction, manifesting as crosstalk, are applied (George et al., 2018).

The raw detector frames constructed by the simulation are then reduced into sky-subtracted data cubes $\mathbf{D}$ with the associated spectral covariance cubes $\mathbf{\Sigma}$ using

the data reduction pipeline (Briesemeister et al., 2018). A telluric calibrator star **M** is also simulated in a similar fashion.

5.3.3 Covariance propagation

The proper approach to treating the PSF fitting as a weighted least squares problem becomes intractable due to the large covariance matrices that would need to be inverted. For context, integral field spectrograph data products are data cubes with (n_λ, n_x, n_y) dimensions. In principle, every point (λ, x, y) in this cube is correlated to every other point, so the appropriate covariance matrix would be $(n_\lambda n_x n_y \times n_\lambda n_x n_y)$ matrix, or for SCALES low-resolution L-band, $(\sim 10^6 \times \sim 10^6)$. Windowing in the spatial coordinates to select a region of interest would reduce this number significantly, but still greatly limits efficiency.

Along with windowing to a 17 $\times$ 17 spaxel region around our target point spread function, we chose to make all spatial covariance components zeros so the matrix becomes sparse and a far more tractable problem (Briesemeister et al., 2019). We propose the data **D** at spatial coordinate (j, k) to be drawn from a multivariate normal distribution with mean $\mathbf{M}\beta$ and covariance $\mathbf{\Sigma}$, for contrast β with respect to the calibrator **M**. We then minimize the square Mahalanobis length to optimize the contrast spectrum.

$$\hat{\beta} = \arg\min_{\beta}(\mathbf{D} - \mathbf{M}\beta)^T\mathbf{\Sigma}^{-1}(\mathbf{D} - \mathbf{M}\beta) = (\mathbf{M}^T\mathbf{\Sigma}^{-1}\mathbf{M})^{-1}\mathbf{M}^T\mathbf{\Sigma}^{-1}\mathbf{D} \tag{5.3}$$

$$cov(\hat{\beta}) = (\mathbf{M}^T \mathbf{\Sigma}^{-1} \mathbf{M})^{-1} \tag{5.4}$$

These quantities are still contrasts with respect to the calibrator flux. Assuming the calibrator has the same exposure time and has not reached saturation, the contrast and covariance can be multiplied by the expected spectrum of the calibrator and its square, respectively, to represent the best-fit spectra $\hat{\mathbf{f}}$ and data error covariance matrix $\mathbf{S_e}$.

5.3.4 The Jacobian

The derivatives of the Jacobian $\mathbf{K} = \partial F_i / \partial x_j$ are calculated by centered finite-differencing scheme for each state vector parameter. We consider two different models for $\mathbf{F}$ in our approach. The first assumes $\mathbf{F}$ is only affected by the atmospheric physical model, the second assumes $\mathbf{F}$ is affected by both the atmospheric and the instrument model. The first scenario describes the case in which all instrument systematics can be removed during the data reduction process, and you are left with the raw atmospheric flux and the associated measurement errors. The latter considers the scenario that instrument systematics affect the ultimately flux measurements. Both models are depicted in Figure 5.1, where the pale blue Jacobians represent the first model and the K-, L- and M-band lines represent the second model. The instrument systematics do reduce the sensitivity at each band to elements of the state vector, and in a non-linear way.

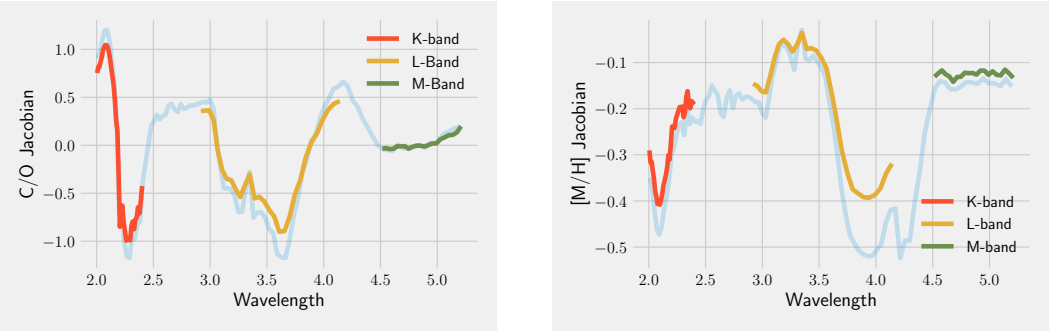

Figure 5.1: The centered finite-difference scheme-derived Jacobians for C/O and $[M/H]$ at K-, L-, and M-bands for a 1500K, $log(g) = 4$, $[M/H] = 1$, $C/O = .55$. The deviations were $\pm.001$ in metallicity and C/O, and the Jacobians are scaled by 10^7. The Jacobian in pale blue was calculated without passing the spectra through the SCALES simulator, binned at resolution of 100. The SCALES model is notably less sensitive at nearly all spectral bins to the hypothetical instrument capable of perfect recovery of the Jacobian.

5.4 Information Content Analysis

The following analysis explores information content for the two composition parameters, $[M/H]$ and C/O, that are used to parameterize elemental abundances that define the mixing ratios ξ_i. Other quantities $[T,\ g]$ are of interest, but we wanted to be specific for our investigation. We set a naive prior $\mathbf{S_a}$ of ± 6 *dex* in both quantities, expressing essentially no prior knowledge of the atmosphere composition.

SCALES has nine separate spectroscopic modes, each of which are sensitive to complementary and supplementary information content for various astrophysical signals. Naturally, one may expect there exist situations where observing in multiple modes would be advantageous from an information content context. The discussion in Batalha and Line (2017) presents arguments for why this may not necessarily be the case due to saturation of information. An in-depth exploration of using such multiple mode observations remains as work for future papers. In what follows we use information content to specifically focus on the 2-5.2 micron mode of SCALES, as it represents one of the more pathological observation modes due to the exceptionally bright sky background in M-band encroaching on bluer ends of neighbor spectra (Figure 5.2).

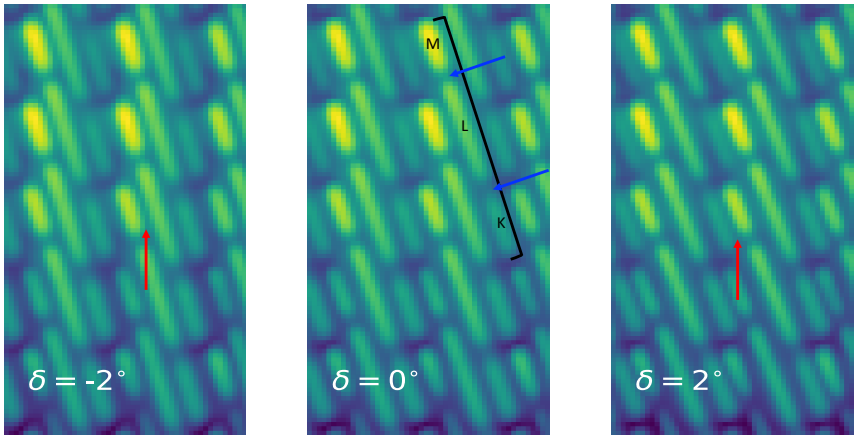

Figure 5.2: The raw detector readout of a bright star in the 2-5 micron mode near the peak of the point spread function at three dispersion angles, set to $\tan^{-1}(1/3)$ and $\tan^{-1}(1/3)\pm 2°$. The color scale is logarithmic. Detector systematics were removed for clarity. The anatomy of a single trace is distinguished in the middle panel, with a bright M-band lobe in the upper left, followed by a gap due to telluric water absorption marked in the blue arrow, a longer L-band lobe, another gap due to telluric water absorption marked in the blue arrow, followed by K-band light. The red arrows point out regions where the bright, variable thermal background in M-band lobes contribute to not only to flux, but also noise, in neighboring K- and L-band spectra, modifying the Jacobian $\mathbf{K}$.

5.4.1 Case study: Misaligned Disperser

This IC approach can be used to tolerance optomechanical design of SCALES. In this case study, we perturb the ideal model of SCALES, such that the angle of dispersion deviates from the fiducial value of $\tan^{-1}(1/3)$. This manifests as a deflection from the ideal angle of the micropupils on the detector. This ideal angle was designed such that it maximizes the length and spectral resolution of the spectra as well as detector usage without the spectra overlapping. This case study will test how much the dispersion angle can be perturbed until the gain of information content is insufficient to satisfy the the fiducial science case within the exposure time.

In previous papers, we have used the simulation as an exposure time calculator to translate the fiducial science case requirements in terms of exposure time. In this case study, we set the requirement that we observe the signal-to-noise ratio of C/O and $[M/H]$ to be greater than 5 in a 1500K brown dwarf at 100pc within two hours total integration time. The diagonal element of the posterior covariance matrix $\hat{\mathbf{S}}$ corresponding to C/O and $[M/H]$ uncertainty is used to define the amount of information content necessary to meet this requirement. We then perturbed the model of SCALES by changing the angle of dispersion (Figure 2), and extracting the spectra assuming this new dispersion angle is known. Once the spectra begin to overlap, the overwhelming number of background photons

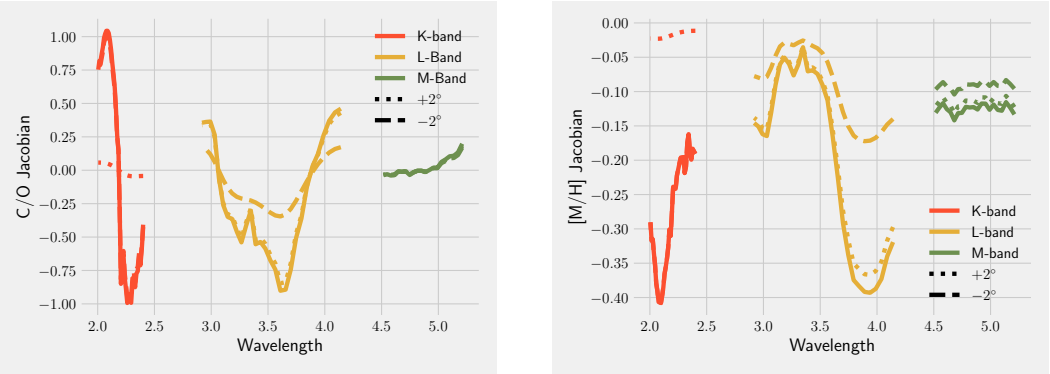

Figure 5.3: The centered finite-difference scheme-derived Jacobians for C/O and $[M/H]$ at K-, L-, and M-bands for a 1500K, $log(g) = 4$, $[M/H] = 1$, $C/O = .55$. The deviations were $\pm.001$ in metallicity and C/O, and the Jacobians are scaled by 10^7. These Jacobians are accompanied by the same measurements taken when the disperser is shifted by $+2°$. The K- and L-band Jacobians are strongly diminished by impinging M-band light from neighboring spaxels.

in neighboring spaxels will begin to inflate the values of flux in the blue end of individual spaxels. This inflation rapidly deviates the extracted spectrum from the expected spectrum to the point where there is very little increase in information, relative to the prior (Figure 3).

According to our translation of this fiducial science requirement, and with all other degrees of freedom fixed, a realistic SCALES can deviate in dispersion angle from the ideal SCALES for all angles with information contents above 20.1 for $[M/H]$ and 20.4 bits for C/O (Figure 4.). At angles more extreme than $\theta \in (18.2°, 18.7°)$, SCALES would not be capable of observing a source satisfying this requirement within the alloted exposure time.

5.5 Summary

Using an emission spectra model, we computed how sensitive the SCALES instrument is to detecting changes in the state vector that define the models. These sensitivities make up the Jacobian, which allowed us to compute the information content of each spectrum. The information content, measured in bits, describes how the state of knowledge (relative to the prior) has increased by making a measurement. We applied this analysis to the case study of a particular optic that is perturbed in such a way to displace the intense thermal background at the red ends of these spectra onto neighboring, dimmer blue ends of spectra.

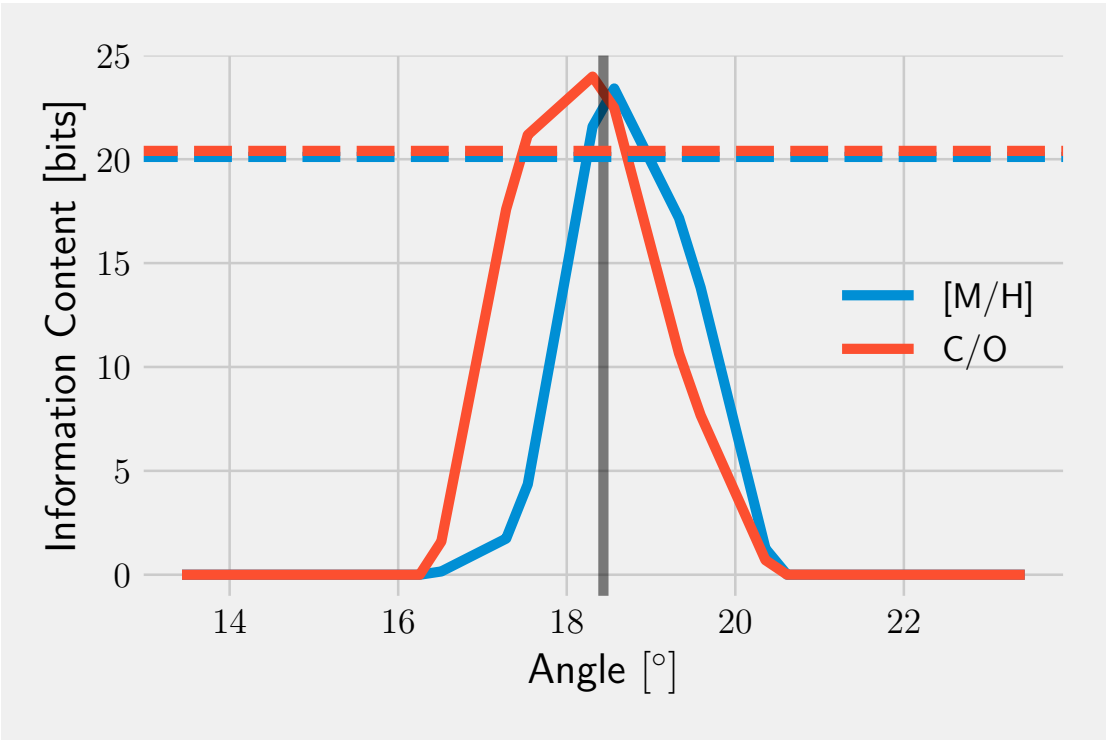

Figure 5.4: The information content in C/O and $[M/H]$ for the fiducial science case described in the text at several dispersion angles. The vertical line denotes $\tan^{-1}(1/3)$, and the respective horizontal lines corresponds to information content necessary to satisfy the fiducial science goal.

The effect on information content was quantified in order to set a scientifically motivated tolerance of the angle of the dispersing element for SCALES. In doing so, we established a recipe to systematically follow to obtain tolerances other free parameters in the SCALES model.

SCALES is expected to be deployed in 2025. After commissioning we will have a much better idea of what the inherent systematics are for each of the exoplanet spectroscopy modes. Until our knowledge of instruments improve, we can use these promising IC analyses to design optimized observing strategies for future proposals.

Acknowledgments

We gratefully acknowledge the support of the Heising-Simons Foundation through grant #2019-1697. ZWB is supported by the National Science Foundation Graduate Research Fellowship under Grant No. 1842400.

Chapter 6

Conclusion

6.1 Comparison to Existing and Upcoming Instruments

Most IFSs with goals of direct imaging exoplanets operate at low-spectral resolutions (R<200), in part because the lenslet array preserves optical quality as it samples the field before any optical aberrations are imparted by downstream spectroscopic optics. This can make it difficult to distinguish between continuum effects (such as clouds and temperature-pressure profiles) and broad molecular band-heads (such as CH_4 and CO). In addition to a low-resolution mode (R$\sim$100), SCALES features a medium-resolution mode (R$\sim$2000), which is unique to high-contrast coronagraphic integral field spectrographs. This will allow line-by-line

identification of major and minor gaseous constituents (Figure 6.1). There is no other instrument capable of doing this today.

The *James Webb Space Telescope* (JWST) has an integral field spectrograph, but it is not coronagraphic and is generally not usable for studying close-in exoplanets. Keck's OSIRIS instrument (Larkin et al., 2006) is certainly complementary, providing R$\sim$4000 spectra of exoplanets from 1–2 μm, but it does not have a coronagraph and is not optimized for high-contrast imaging. GPI 2.0 (Chilcote et al., 2020) and SPHERE+ (Boccaletti et al., 2020) will also provide complementary spectra in the near-infrared at lower resolutions. Keck's KPIC instrument is also complementary, providing R$\sim$35,000 spectroscopy of exoplanets. However, KPIC is generally used for detecting the presence of molecules, exoplanet spins and exoplanet RVs via the cross-correlation method (e.g., Wang et al., 2021), while SCALES is more optimal for obtaining flux densities at high signal-to-noise. Decades of studying free-floating brown dwarfs, which are analogs to gas-giant exoplanets, shows the incredible scientific power of medium resolution spectroscopy (Cushing et al., 2005).

In general, SCALES integral field spectroscopy will provide an improvement over imaging for most thermal-infrared science cases that don't require a large field-of-view. SCALES will continue the scientific legacy of NIRC2, while also providing a venue for studying JWST discoveries at higher spatial resolution.

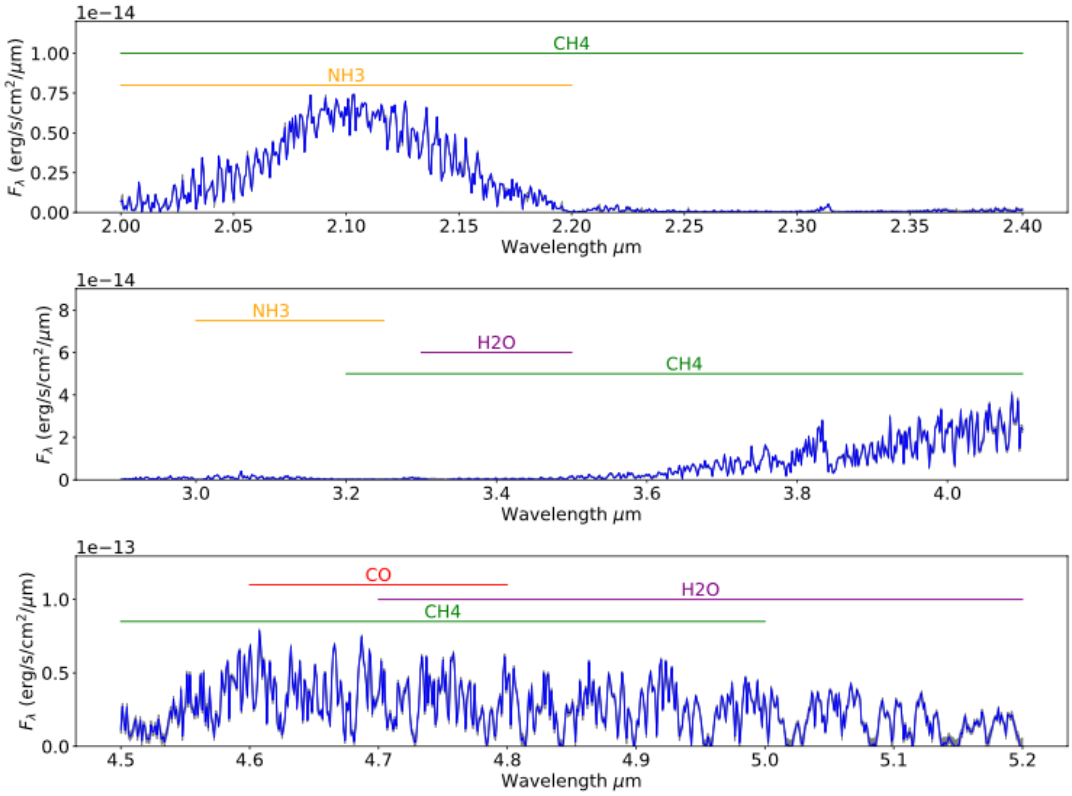

Figure 6.1: Simulation from Chapter 4, K-band (top), L-band (middle), and M-band (bottom) medium resolution mode SCALES observations of a 500 K planet at a distance of 15 pc. The assumed integration time is 10 hours, and the extracted spectrum is shown in blue with error bars overlaid in grey. SCALES' wavelength coverage will lead to constraints on molecules such as H_2O, CO, CH_4, NH_3 (see horizontal bars), which can be used to calculate properties such as metallicities and C/O ratios.

And while SCALES's driving science case is exoplanet spectroscopy, the resulting design cover a unique parameter space that will make SCALES an exciting instrument for many subfields of astronomy and planetary science.

6.2 Synergy of Direct Imaging and Astrometric Detection

In the past decade, substantial effort has been put in to find young gas giants around nearby moving group stars. Thousands of hours of 8- to 10-m class telescope time were devoted to performing high-contrast imaging surveys of hundreds of young stars, but the overall detection rate turned out to be low. Moving to 30-m class telescopes is not expected to help; wide separation gas giants are just intrinsically rare. Clearly, the strategies of the past will not yield the sample we need to test models of gas giant formation and evolution.

In order to circumvent the "blind" nature of previous direct imaging surveys with prohibitively low detection rates, we identified full-sky absolute astrometry as a powerful complement to direct imaging surveys of exoplanets (Brandt et al., 2019a). Facilitated by space-based astrometric missions providing an age-insensitive population of tens of thousands of substellar and planetary-mass companions detected through the astrometric reflex motion of their host, the most

sensitive upcoming space- and ground-based direct imaging/spectroscopy surveys will characterize the atmospheres and system architectures of *hundreds* of exoplanetary systems. This population would be *transformative* to the field of exoplanets; we could robustly test models of exoplanet atmospheres, reliably extract physical parameters using spectral signature retrieval, determine planetary system architectures, and could provide answers to open questions in planet formation and migration on both individual and population levels.

The synergy between full-sky absolute astrometry and direct imaging of exoplanets is being addressed from both sides: (1) the Wide-Field Instrument on the NASA space mission, *Nancy Grace Roman Space Telescope* (hereafter, *Roman*), is capable of detecting the astrometric reflex motion of a planet-hosting star, and will improve the astrometric precision, baseline, and dynamical mass constraints established by ESA space missions *Hipparcos* and *Gaia*; and (2) current and upcoming near- and thermal-infrared space- and ground-based instruments are deploying in the near term on *Roman*–CGI (Coronagraph Instrument), *James Webb Space Telescope* (*JWST*), SCALES, GPI 2.0 (Chilcote et al., 2020), SPHERE+ (Boccaletti et al., 2020), and comprise the most sensitive arsenal we have to directly characterize the atmospheres of exoplanets.

Widest-period planets are the easiest ones to follow up with high-contrast instruments and test model atmospheres and planet formation scenarios, but the

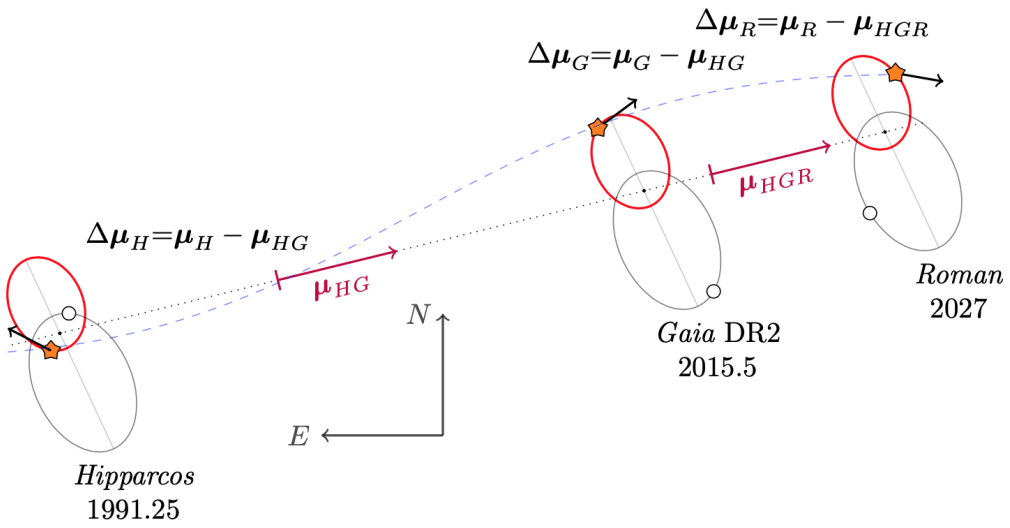

Figure 6.2: Principle of the determination of the proper motion anomaly at respective epochs. The photocenter (dashed blue) of the system evolves due to the influence of a photometrically-negligible companion (white circle) on the star (orange star). By combining astrometry and RV data, we measure the full 3D acceleration of a star in response to an unseen companion, which depends only on companion mass and separation. Therefore, a single imaging measurement of separation uniquely determines the dynamical mass.

hardest ones to find both with current astrometry and RV measurements due to their small signals. How will we confirm the astrometric detections, and how will we push the sensitivity further?

Earlier probes of full-sky absolute astrometry, namely the ESA space missions *Hipparcos* and *Gaia* extend the astrometric baseline back $\gtrsim$30 years. *Hipparcos* epoch astrometry was used to fit planet orbits, but the precision was shown to be insufficient, and more recent work suggests that the re-reduction of *Hipparcos* overfit bright stars (Anderson and Francis, 2012). *Gaia* has both internal and (unknown) external uncertainties which are generically underestimated, and the form of error inflation that is needed depends on magnitude, color, and position of the star; these can only be calibrated with the aid of a comparison sample where the solution is known. Quasars can provide this reference sample at faint magnitudes, but for bright stars, we need independent astrometry. *Hipparcos* serves this purpose today, but only up to $\sim$11 mag. This leaves out a great number of low-mass stars as close as $\sim$10 pc – there is no way to independently verify their astrometry. When measuring the significance of astrometric accelerations and thus the companion masses, it is essential to have well-calibrated uncertainties (Brandt, 2018). From the perspective of high-contrast imaging, *Gaia* has two glaring shortcomings: (1) Limited independent verification of precision; and (2) A lack of sensitivity to orbital periods significantly longer than 10 years.

The answer to both is sporadic, continued astrometric monitoring. While *Roman* alone will be unable to measure exoplanet orbits longer than 10 years, it will be sensitive to measuring stellar accelerations because the positional departure from linear motion for short orbital arcs scales as t^2. *Gaia* is currently measuring full-sky absolute astrometry to exceptional precision with its 9-year extended mission, and is expected to discover thousands of new exoplanets (Perryman et al., 2014). This astrometry can already constrain the masses of nearby massive exoplanets and brown dwarfs in combination with RV measurements (Brandt et al., 2019b).

Roman will effectively extend this baseline to 40 years. This will enable an independent calibration of *Gaia*'s astrometry, particularly of its uncertainties, and provide sensitivity to longer orbital periods. The *Hipparcos–Gaia–Roman* baseline has precisions in mean proper motion that are generally much higher than that of any individual baseline, and will be capable of probing even lower accelerations, and ever-longer orbital periods. This even improves prospects of imaging exoplanets with SCALES (Figure 6.3) and CGI (Figure 6.4).

The convergence between the commissioning of SCALES (first light 2025) and the launch of *Roman* is serendipitous: the subpopulation of directly observable exoplanets newly detected through space-based astrometry provides a unique, unbiased, and underexplored parameter space to bridge the census of

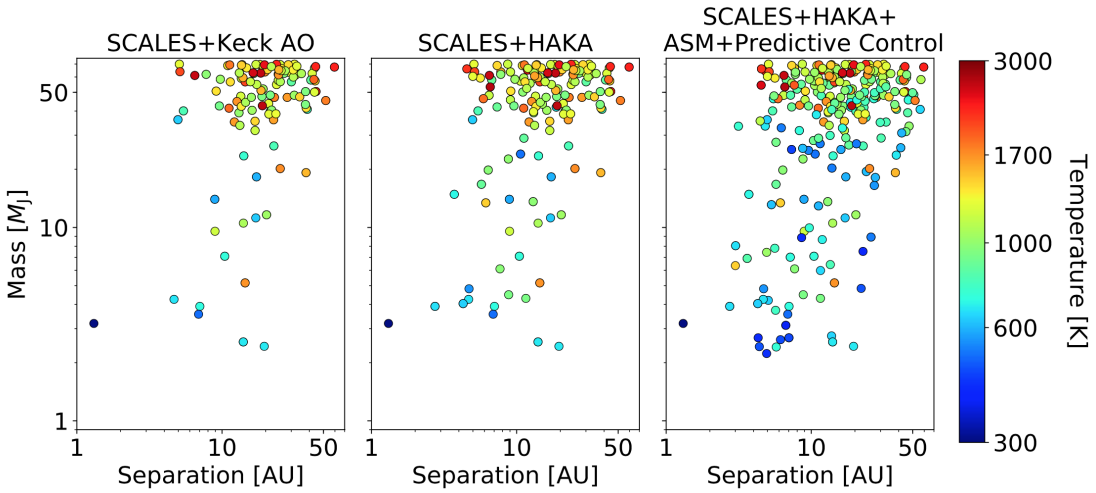

Figure 6.3: Properties of simulated companions in Hipparcos–Gaia–Roman baseline for SCALES with three adaptive optics state and astrometric data releases: the current Keck AO system with *Gaia* EDR3, a proposed high-order deformable mirror HAKA with *Gaia* DR4, and HAKA plus an adaptive secondary mirror + predictive control and the first epoch of *Roman* astrometry. A companion is determined to be astrometrically detected if fitting a full orbital model improves the astrometric residuals by $\Delta\chi^2 \geq 30$ over a fit assuming constant proper motion (Perryman et al., 2014), with orbital elements propagated to 2025.

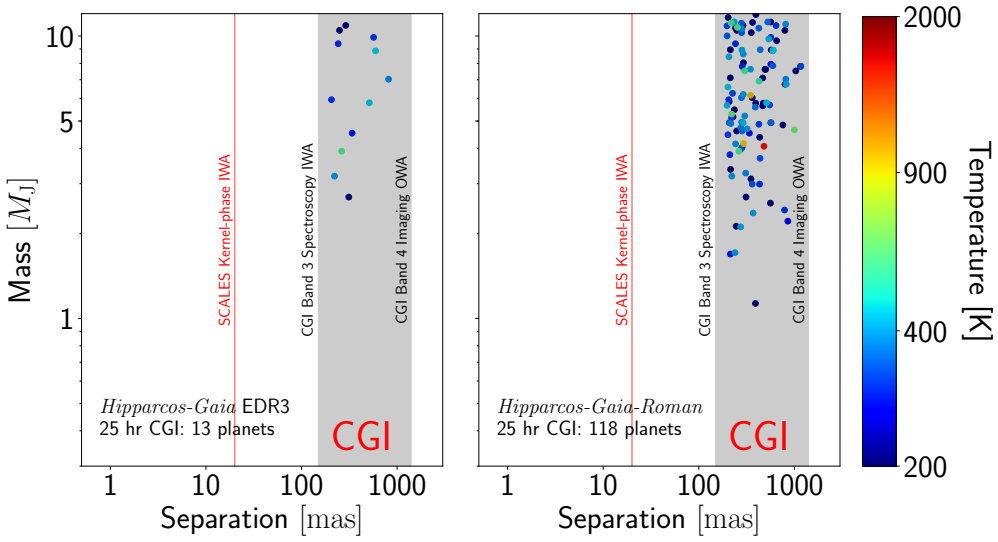

Figure 6.4: Properties of simulated planetary-mass companions detected by *Roman*–CGI in thermal emission in the *Hipparcos–Gaia* EDR3 and *Hipparcos–Gaia–Roman* baselines. Determining the capabilities of reflected light detections will also be considered in the proposed survey. These simulations combined contrast curves for 25hr integrations at Band 3 (B3; 730 nm) spectroscopy and Band 4 (B4; 825 nm) imaging, and assumed the color relationships $G_{RP} - B3 = 0$ and $G_{RP} - B4 = 0$.

well-characterized gas giant planets (Brandt et al., 2019a). Direct characterization of this trove has the capacity to vastly improve our understanding of the outcomes of planetary formation, migration, cooling, chemistry and circulation.

As a NASA Postdoctoral Fellow at Goddard, I will to expand upon the preliminary investigations into WFI astrometric capabilities in several key ways:

1. Investigate detector systematics, determine the domain of recoverability from saturation, and determine their limitations for astrometric surveys

2. Investigate how telescope dynamics modify the point spread function to improve or degrade the ability to determine the center of a star

3. Design an early "snapshot" WFI astrometric survey to select targets for characterization with *Roman* Coronographic Instrument (CGI)

4. Fine tune other WFI surveys at no scientific cost to them in order to "piggyback" them to increase the epochs for astrometric detection of exoplanets

These activities will place new, direct constraints on WFI astrometric detection of exoplanets, adjust yield estimates of direct imaging missions in the immediate term (SCI-06), and provide the most promising targets for space- and ground-based characterization. As there are no future NASA missions planned capable of astrometric detection of exoplanets, enabling and maximizing this science now is critical to expanding the outcomes of *Roman*.

Project 1 entails investigating the nonlinearity, persistence, and saturation of the 10-micron pitch Teledyne HAWAII-4RG (H4RG-10; Mosby et al., 2020) detectors to explore their impact on astrometry with WFI. The Goddard Detector Characterization Lab (DCL) has selected the flight detectors for *Roman*. The flight spares exist to provide meaningful characterization of the H4RG-10s, with the flexibility to continually test them. Over the next few years, the *Roman* Project Science team and DCL will be planning and executing a range of experiments with flight spare detectors that are relevant to WFI astrometric precision. At Goddard, I will be able to directly collaborate with these teams to propose new configurations of measurements of the detector characteristics, prototype algorithms for recovering information in saturated point spread functions with actual H4RG-10 detector data, and simulate the contributions of error enumerated by Melchior et al. (2018).

For Project 2, I plan to investigate how the realistic point spread functions caused by the structural-thermal observatory environment will impact the ability to determine photocenters. I will take advantage of the continuing integrated modeling of *Roman* based on JWST (Johnston et al., 2004) to use simulations of point spread functions calculated through time-series wavefront errors due to the telescope in order to determine the magnitude of deviation of the point spread functions across the WFI field in high fidelity for the first time. I will explore

how we might take advantage of point spread function aberration knowledge to improve photocenter determinations.

Both projects are space-based equivalents to my ground-based studies of the SCALES detector and instrument using my end-to-end simulator (Chapters 4 and 5). These two projects will provide direct constraints on the astrometric capabilities of WFI, and will also enable the weak lensing and microlensing teams to make assessments of WFI's capabilities for their respective science goals. The end product will provide realistic simulations containing all pertinent effects and conditions from the observational process specific to the *Roman* mission that may affect the quality of photocenter determination from real WFI images. These simulations provide a foundation to characterize the relative impact of undesired effects and to validate the astrometric detections themselves.

Projects 3 will define a single epoch of high-precision astrometry with WFI to provide exceptional value to exoplanet science in general and to high-contrast imaging in particular. A shallow, full-sky WFI astrometric survey will help discover *hundreds* of exoplanets accessible to direct imaging from the ground and space, including CGI (Figure 6.4). The sample has a well-defined selection criteria, making it ideally suited to detailed comparisons to planet formation models. This survey would:

1. Measure and correct any systematics in *Gaia* astrometry

2. Identify hundreds of long-period planets around nearby stars, which can then be imaged by space- and ground-based telescopes

3. Enable dynamical mass measurements of hundreds of planets, and place models of planet and brown dwarf evolution on a firm observational footing

The early nature of the survey is motivated by the concerted effort it takes to vet these systems with adaptive optics or speckle interferometers to exclude systems pathological to high-contrast imaging (e.g. Bowler et al., 2021), and measure RV trends to resolve dynamical mass degeneracies. While this proposal focuses on the exoplanet science case, such a survey could also search for accelerations caused by dark matter halos, and might discover black holes and neutron stars that are not accreting. The proposed survey would also perform full-sky infrared photometry, which enables its own array of science, including full-sky reference images for transient astronomy, and a detailed comparison map for the Vera Rubin Observatory enabling further cross-calibration.

Project 4 builds upon the use case of Project 3 by enabling simultaneous measurements of astrometric epochs observed within other WFI surveys; nearly every image taken with WFI is expected to contain a large number of exoplanet-hosting stars and quasar anchors for determination of the inertial reference frame. By "piggy-backing" on other WFI surveys, Project 4 maximizes WFI exoplanet science. Project 4 will utilize the requirements derived from Projects 1 and 2 to

determine what, if any, requirements we can place on other WFI surveys, such that their science objectives are unaffected while enabling ancillary astrometric epochs in support of this project. These projects maximize astrometric capabilities of WFI, and fine-tune other surveys at no scientific cost. The end product will direct early CGI science, as we will detect a broad range of directly observable exoplanets that can be characterized with CGI, and we will improve upon CGI's scientific yield compared to just using the *Hipparcos–Gaia* baseline (Figures 6.3 and 6.4).

With a sample of exoplanets discovered astrometrically with precise dynamical masses, we can move away from assuming stellar ages and planet cooling curves and fitting to observed luminosities. This sample will *test*, rather than assume, models of planet formation and evolution, and comprise a much larger and diverse sample than what we currently have.

With our current sample (∼dozens), we can correlate exoplanet radii and masses with orbital and stellar properties to compare to predictions of planet formation theory (Winn and Fabrycky, 2015). WFI astrometry promises a sample of *hundreds* of directly observable exoplanets. Spectra from integral field spectrographs will be used to correlate exoplanets' elemental abundances and atmospheric chemistry with their orbits and masses, and study the dependence of planet properties on stellar properties at individual and population levels.

Astrometry is almost free of selection biases: its sensitivity depends only on stellar brightness and distance from Earth. WFI and CGI will open up the coldest planets (∼200K) for spectroscopy, where models have not yet been tested. With a large, nearly unbiased initial selection, we can resolve the theoretical uncertainties over initial entropy and study the evolution of planetary systems over billions of years.

6.3 Infrared Interferometric Imaging with SCALES

Enabling the direct detection and characterization of these exoplanets is approached in two ways: (1) observing at wavelengths with the least planet-star contrast; and (2) pushing the limits of current instrumentation and observational methods to be capable of distinguishing a planet from a star at angular separations of ten(s) of milliarcseconds. Cool ($T_{\rm eff} < 1000K$) exoplanets have the most favorable contrasts with respect to their host star in thermal infrared (2–5μm) bands (Chapter 3). A really rewarding path to follow would be to enable a combination of thermal infrared integral field spectroscopy and kernel-phase interferometry to characterize emission spectra of exoplanets beyond previous differential photometric methods. This cutting edge science will push the technological limits of SCALES, maximizing its potential for exoplanet characterization and providing the technical basis for future kernel-phase interferometric integral field spectro-

graph instruments on extremely large telescopes.

Interferometric imaging techniques that simulate a partial or whole aperture as an interferometric array have been developed to provide the method by which companion light can be distinguished from their host star light at an angular separation *inside* the Rayleigh Criterion limit. Infrared interferometric techniques involve simulating the pupil as an interferometric array, either by physically modifying the pupil with a pupil plane mask (NRM; Tuthill et al., 2000) or decomposing the entire pupil into a grid of subapertures in post-processing (kernel-phase; Figure 6.5; Martinache, 2010). In the high-adaptive optics correction limit, the observable quantities (closure-phases for NRM, kernel-phases for kernel-phase interferometry) are immune to the phase-noise that corrupt image quality in a conventional filled-aperture image, resulting in a better constrained PSF than conventional imaging would offer. However, NRM is severely flux-limited because the mask discards ∼95% of the gathered light.

Kernel-phase analysis applies similar interferometric techniques to an unobscured diffraction limited image, simulating the full telescope aperture as an interferometer composed of a grid of subapertures, and has been demonstrated on Hubble Space Telescope archival data (Martinache, 2010). Kernel-phase interferometry can detect companions at contrasts of ∼1:100 for separations even within the diffraction limit with much greater efficiency than NRM. This technique re-

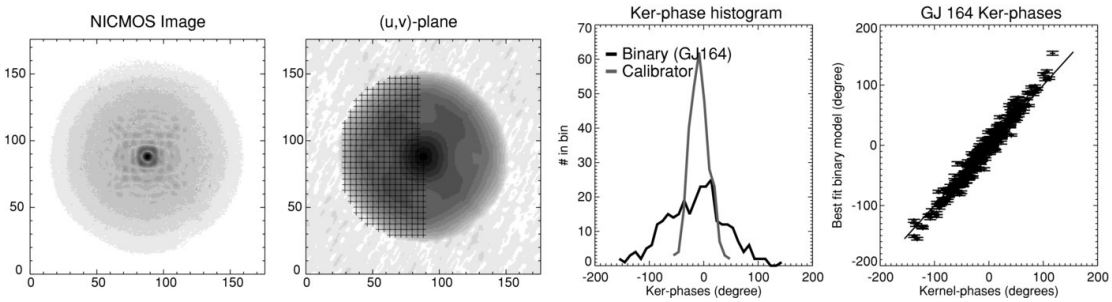

Figure 6.5: From left to right: (1) a narrow-band image is Fourier transformed to reveal a power spectrum (2) with redundancy of baseline indicated by color and a grid indicating the regions of the uv–plane sampled for kernel-phase calculation (the Fourier transform is symmetric, so the other side would provide the same samples). (3) The histogram of kernel-phases of the calibrator and a binary (GJ164), where the calibrator kernel-phases are zero within uncertainty and the binary has a greater diversity of kernel-phases as they system is inherently asymmetric. (4) The comparison of GJ164 measured kernel-phases and kernel-phases derived from a model fit with copies of the calibrator as binary components. From Martinache (2010).

quires image fidelity that has otherwise been unachievable from the ground except at $\gtrsim 5\mu$m. However, when coupled with an integral field spectrograph, the measured PSF encodes a hologram of the input wavefront (Martinache, 2016). This ends up relaxing the assumption of small aberrations, such that the capture range is no longer limited by the wavelength of operation but by the coherence length that is directly proportional to the spectral resolution of the data. While narrow-band filters typically have a spectral resolution of $<$10, SCALES offer six low-resolution integral field spectrograph modes with resolutions between 35 and 200.

The synergy of combining thermal infrared integral field spectroscopy and kernel-phase interferometry addresses the following key science factors that will enable the characterization of close-in exoplanets:

- Cool exoplanets have the most favorable contrasts (easiest to detect) with respect to their host star
- Sensitivity to a broad region of the spectral energy distribution with the most flux for cool exoplanets
- Sensitivity to $\gtrsim$30 mas separation from the ground
- Reduced dependence of extreme adaptive optics correction
- 100$\times$ greater observing efficiency than NRM

- Direct characterizing of a population of companions with measured dynamical masses from *Gaia*
- Spatially resolved thermal infrared spectra with complete stellar light rejection

As such, enabling this science with SCALES will be paramount to maximizing the science outcomes of the instrument, a goal that has guided my entire thesis. The subpopulation of directly observable exoplanets detected through space-based astrometry provides a unique, unbiased, and otherwise unexplored parameter space to bridge the census of well-characterized exoplanets.

Wavefront Metrology

Wavefront metrology is a natural consequence of dispersed kernel-phase interferometry, as the PSF as a function of wavelength encodes a hologram of the input wavefront. Excluding index of refraction changes, we can exploit the chromatic characteristics of instrumental phase in the same way it has been used for fringe tracking in long-baseline interferometry for decades (e.g., Pope et al., 2014). The concept for this is described in Martinache (2016).

When the monochromatic kernel-phases in an integral field spectrograph data cube are treated independently, attributing piston values to the baselines is a degenerate problem as in narrow-band kernel-phase. However, when treated in

concert, the PSFs as a function of wavelength provide unique sampling of the piston values for each baseline, and the degeneracy is lifted. This means performing kernel-phase interferometry with integral field spectrographs is simultaneously measuring the astrophysical data and wavefront metrology.

Reference Differential Imaging (RDI) for broadband kernel-phase has been necessary to provide a PSF calibrator for kernel-phase calibration of the datasets. Using calibrator PSFs on stars with different spectra or different instrumental wavefronts will result in imperfect calibration of the final kernel-phases and has been the key obstacle that has limited broadband kernel-phase. Standard narrowband calibration strategies explicitly remove sensitivity to the continuum signal. This needs to be addressed for kernel-phase interferometry with integral field spectrographs. The continuum contains critical information about the state vector of the atmosphere, notably temperature, surface gravity, C/O ratio, metallicity. Without advancements in calibration techniques, this will relegate the kernel-phase interferometric integral field spectrograph data to be strictly a detection tool rather than the atmospheric characterization instrument we need.

With an integral field spectrograph, the added wavefront metrology and dispersal of the PSF calibrator can be used to form a reference library that correlates strongly in wavefront metrology with the target dataset with no new observational cost. The spectrum of the star will no longer matter when scaled at each wave-

length appropriately. Combining with the adaptive optics telemetry from Keck, the imperfect calibration problem that has plagued the kernel-phase field is removed.

In principle, implementation only requires non-invasive software development and observation planning. This would make an excellent first year graduate student project, and should certainly be completed prior to SCALES first light in 2025.

6.4 Summary

In Chapter 1, I motivated the need for thermal infrared integral field spectroscopy for probing both young and mature exoplanets at wide separations from their host star to populate the underexplored parameter space. I introduced the challenges faced by high-contrast observers, and the technological development that went into overcoming these challenges. I introduced ALES and SCALES in preparation for the rest of the thesis.

In Chapter 2, I explored the ALES Data Reduction Pipeline and data processing tools developed by 2018 with a reprint of Briesemeister et al. (2018). The ALES Data Reduction Pipeline has been adapted to use for reducing the raw simulated data from Chapter 4. The work in this Chapter directly enabled (Briesemeister et al., 2019), Stone et al. (2020), Doelman et al. (2021), and Doelman

et al. (2022), each including Z. Briesemeister as co-author.

In Chapter 3, I report on the commissioning science data set for ALES, comprising L-band spectroscopy of HD 130948BC with a reprint of Briesemeister et al. (2019). Jointly using JHK photometry and ALES L-band spectra for HD 130948BC, we derive atmospheric parameters that are consistent with parameters derived from evolutionary models. We leverage the consistency of these atmospheric quantities to favor a younger age of the system compared to the older age determined with gyrochronology in order to address a luminosity discrepancy.

In Chapter 4, I described end-to-end simulations of the lenslet-based low-resolution integral field spectroscopy and the lenslet-slicer medium-resolution integral field spectroscopy of SCALES with a reprint of Briesemeister et al. (2020). The simulation processes arbitrary-resolution input intensity fields with a proposed observation pattern into an entire mock dataset of raw detector read-out lenslet-based IFS frames with calibrations and metadata, which are then reduced by the IFS data reduction pipeline to be analyzed by the user.

In Chapter 5, I describe an information content approach to tolerancing the SCALES instrument with simulations in a reprint of Briesemeister et al. (2021). We specifically focus on how deviations of the dispersion angle precluded the ability to observe atmospheric states within a set exposure time. This paradigm has been applied to other features in the simulation.

In Chapter 6, I concluded by placing SCALES in context of contemporary direct imaging instruments. Next, I described the synergy between direct imaging and astrometric detection of exoplanets from long-baseline all-sky astrometry, along with reporting on the activities I will be completing during my NPP Fellowship at Goddard. Finally, I discussed the extremely intriguing infrared interferometric capabilities of SCALES, and left this as future work.

Bibliography

F. Allard. The BT-Settl Model Atmospheres for Stars, Brown Dwarfs and Planets. In M. Booth, B. C. Matthews, and J. R. Graham, editors, *Exploring the Formation and Evolution of Planetary Systems*, volume 299 of *IAU Symposium*, pages 271–272, January 2014. doi: 10.1017/S1743921313008545.

E. Anderson and Ch. Francis. XHIP: An extended hipparcos compilation. *AstL*, 38(5):331–346, 2012. doi: 10.1134/S1063773712050015.

Sean M. Andrews, Katherine A. Rosenfeld, Adam L. Kraus, and David J. Wilner. The Mass Dependence between Protoplanetary Disks and their Stellar Hosts. *ApJ*, 771(2):129, July 2013. doi: 10.1088/0004-637X/771/2/129.

Astropy Collaboration, A. M. Price-Whelan, B. M. Sipőcz, H. M. Günther, P. L. Lim, S. M. Crawford, S. Conseil, D. L. Shupe, M. W. Craig, N. Dencheva, A. Ginsburg, J. T. VanderPlas, L. D. Bradley, D. Pérez-Suárez, M. de Val-Borro, T. L. Aldcroft, K. L. Cruz, T. P. Robitaille, E. J. Tollerud, C. Ardelean, T. Babej, Y. P. Bach, M. Bachetti, A. V. Bakanov, S. P. Bamford, G. Barentsen, P. Barmby, A. Baumbach, K. L. Berry, F. Biscani, M. Boquien, K. A. Bostroem, L. G. Bouma, G. B. Brammer, E. M. Bray, H. Breytenbach, H. Buddelmeijer, D. J. Burke, G. Calderone, J. L. Cano Rodríguez, M. Cara, J. V. M. Cardoso, S. Cheedella, Y. Copin, L. Corrales, D. Crichton, D. D'Avella, C. Deil, É. Depagne, J. P. Dietrich, A. Donath, M. Droettboom, N. Earl, T. Erben, S. Fabbro, L. A. Ferreira, T. Finethy, R. T. Fox, L. H. Garrison, S. L. J. Gibbons, D. A. Goldstein, R. Gommers, J. P. Greco, P. Greenfield, A. M. Groener, F. Grollier, A. Hagen, P. Hirst, D. Homeier, A. J. Horton, G. Hosseinzadeh, L. Hu, J. S. Hunkeler, Ž. Ivezić, A. Jain, T. Jenness, G. Kanarek, S. Kendrew, N. S. Kern, W. E. Kerzendorf, A. Khvalko, J. King, D. Kirkby, A. M. Kulkarni, A. Kumar, A. Lee, D. Lenz, S. P. Littlefair, Z. Ma, D. M. Macleod, M. Mastropietro, C. McCully, S. Montagnac, B. M. Morris, M. Mueller, S. J. Mumford, D. Muna, N. A. Murphy, S. Nelson, G. H. Nguyen, J. P. Ninan, M. Nöthe, S. Ogaz, S. Oh, J. K. Parejko, N. Parley, S. Pascual, R. Patil, A. A. Patil, A. L. Plunkett, J. X. Prochaska, T. Rastogi, V. Reddy Janga, J. Sabater, P. Sakurikar, M. Seifert,

L. E. Sherbert, H. Sherwood-Taylor, A. Y. Shih, J. Sick, M. T. Silbiger, S. Singanamalla, L. P. Singer, P. H. Sladen, K. A. Sooley, S. Sornarajah, O. Streicher, P. Teuben, S. W. Thomas, G. R. Tremblay, J. E. H. Turner, V. Terrón, M. H. van Kerkwijk, A. de la Vega, L. L. Watkins, B. A. Weaver, J. B. Whitmore, J. Woillez, V. Zabalza, and Astropy Contributors. The Astropy Project: Building an Open-science Project and Status of the v2.0 Core Package. *AJ*, 156:123, September 2018. doi: 10.3847/1538-3881/aabc4f.

Henning Avenhaus, Sascha P. Quanz, Antonio Garufi, Sebastian Perez, Simon Casassus, Christophe Pinte, Gesa H. M. Bertrang, Claudio Caceres, Myriam Benisty, and Carsten Dominik. Disks around T Tauri Stars with SPHERE (DARTTS-S). I. SPHERE/IRDIS Polarimetric Imaging of Eight Prominent T Tauri Disks. *ApJ*, 863(1):44, August 2018. doi: 10.3847/1538-4357/aab846.

V. P. Bailey, P. M. Hinz, A. T. Puglisi, S. Esposito, V. Vaitheeswaran, A. J. Skemer, D. Defrère, A. Vaz, and J. M. Leisenring. Large binocular telescope interferometer adaptive optics: on-sky performance and lessons learned. In *Adaptive Optics Systems IV*, volume 9148 of *Proc. SPIE*, page 914803, July 2014. doi: 10.1117/12.2057138.

A. Banzatti, P. Pinilla, L. Ricci, K. M. Pontoppidan, T. Birnstiel, and F. Ciesla. Direct Imaging of the Water Snow Line at the Time of Planet Formation using Two ALMA Continuum Bands. *ApJL*, 815(1):L15, December 2015. doi: 10.1088/2041-8205/815/1/L15.

I. Baraffe, D. Homeier, F. Allard, and G. Chabrier. New evolutionary models for pre-main sequence and main sequence low-mass stars down to the hydrogen-burning limit. *AAP*, 577:A42, May 2015. doi: 10.1051/0004-6361/201425481.

T. S. Barman, B. Macintosh, Q. M. Konopacky, and C. Marois. Clouds and Chemistry in the Atmosphere of Extrasolar Planet HR8799b. *ApJ*, 733:65, May 2011. doi: 10.1088/0004-637X/733/1/65.

T. S. Barman, Q. M. Konopacky, B. Macintosh, and C. Marois. Simultaneous Detection of Water, Methane, and Carbon Monoxide in the Atmosphere of Exoplanet HR8799b. *ApJ*, 804:61, May 2015. doi: 10.1088/0004-637X/804/1/61.

S. A. Barnes. Ages for Illustrative Field Stars Using Gyrochronology: Viability, Limitations, and Errors. *ApJ*, 669:1167–1189, November 2007. doi: 10.1086/519295.

Joanna K. Barstow and Kevin Heng. Outstanding Challenges of Exoplanet Atmospheric Retrievals. *SSR*, 216(5):82, June 2020. doi: 10.1007/s11214-020-00666-x.

Natasha E. Batalha and M. R. Line. Information Content Analysis for Selection of Optimal JWST Observing Modes for Transiting Exoplanet Atmospheres. *AJ*, 153(4):151, April 2017. doi: 10.3847/1538-3881/aa5faa.

Natasha E. Batalha, Mark S. Marley, Nikole K. Lewis, and Jonathan J. Fortney. Exoplanet Reflected-light Spectroscopy with PICASO. *ApJ*, 878(1):70, June 2019. doi: 10.3847/1538-4357/ab1b51.

J. W. Beletic, R. Blank, D. Gulbransen, D. Lee, M. Loose, E. C. Piquette, T. Sprafke, W. E. Tennant, M. Zandian, and J. Zino. Teledyne Imaging Sensors: infrared imaging technologies for astronomy and civil space. In *High Energy, Optical, and Infrared Detectors for Astronomy III*, volume 7021 of *Proc. SPIE*, page 70210H, July 2008. doi: 10.1117/12.790382.

G. Fritz Benedict, Barbara E. McArthur, Edmund P. Nelan, and Thomas E. Harrison. Astrometry with Hubble Space Telescope Fine Guidance Sensors A Review. *PASP*, 129(971):012001, 2017. doi: 10.1088/1538-3873/129/971/012001.

W. Benz, S. Ida, Y. Alibert, D. Lin, and C. Mordasini. Planet Population Synthesis. In Henrik Beuther, Ralf S. Klessen, Cornelis P. Dullemond, and Thomas Henning, editors, *Protostars and Planets VI*, page 691, January 2014. doi: 10.2458/azu_uapress_9780816531240-ch030.

Beth A. Biller, Laird M. Close, Elena Masciadri, Eric Nielsen, Rainer Lenzen, Wolfgang Brandner, Donald McCarthy, Markus Hartung, Stephan Kellner, Eric Mamajek, Thomas Henning, Douglas Miller, Matthew Kenworthy, and Craig Kulesa. An Imaging Survey for Extrasolar Planets around 45 Close, Young Stars with the Simultaneous Differential Imager at the Very Large Telescope and MMT. *Astrophysical Journal Supplemental*, 173(1):143–165, November 2007. doi: 10.1086/519925.

G. L. Bjoraker, H. P. Larson, and V. G. Kunde. The abundance and distribution of water vapor in Jupiter's atmosphere. *ApJ*, 311:1058–1072, December 1986a. doi: 10.1086/164842.

G. L. Bjoraker, H. P. Larson, and V. G. Kunde. The gas composition of Jupiter derived from 5 micron airborne spectroscopic observations. *Icarus*, 66:579–609, June 1986b. doi: 10.1016/0019-1035(86)90093-X.

A. Boccaletti, G. Chauvin, D. Mouillet, O. Absil, F. Allard, S. Antoniucci, J. C. Augereau, P. Barge, A. Baruffolo, J. L. Baudino, P. Baudoz, M. Beaulieu, M. Benisty, J. L. Beuzit, A. Bianco, B. Biller, B. Bonavita, M. Bonnefoy, S. Bos, J. C. Bouret, W. Brandner, N. Buchschache, B. Carry, F. Cantalloube, E. Cascone, A. Carlotti, B. Charnay, A. Chiavassa, E. Choquet, Y. Clenet, A. Crida, J. De Boer, V. De Caprio, S. Desidera, J. M. Desert, J. B. Delisle, P. Delorme, K. Dohlen, D. Doelman, C. Dominik, V. D Orazi, C. Dougados, S. Doute, D. Fedele, M. Feldt, F. Ferreira, C. Fontanive, T. Fusco, R. Galicher, A. Garufi, E. Gendron, A. Ghedina, C. Ginski, J. F. Gonzalez, D. Gratadour, R. Gratton, T. Guillot, S. Haffert, J. Hagelberg, T. Henning, E. Huby, M. Janson, I. Kamp, C. Keller, M. Kenworthy, P. Kervella, Q. Kral, J. Kuhn, E. Lagadec, G. Laibe, M. Langlois, A. M. Lagrange, R. Launhardt, L. Leboulleux, H. Le Coroller, G. Li Causi, M. Loupias, A. L. Maire, G. Marleau, F. Martinache, P. Martinez, D. Mary, M. Mattioli, J. Mazoyer, H. Meheut, F. Menard, D. Mesa, N. Meunier, Y. Miguel, J. Milli, M. Min, P. Molliere, C. Mordasini, G. Moretto, L. Mugnier, G. Muro Arena, N. Nardetto, M. N Diaye, N. Nesvadba, F. Pedichini, P. Pinilla, E. Por, A. Potier, S. Quanz, J. Rameau, R. Roelfsema, D. Rouan, E. Rigliaco, B. Salasnich, M. Samland, J. F. Sauvage, H. M. Schmid, D. Segransan, I. Snellen, F. Snik, F. Soulez, E. Stadler, D. Stam, M. Tallon, P. Thebault, E. Thiebaut, C. Tschudi, S. Udry, R. van Holstein, P. Vernazza, F. Vidal, A. Vigan, R. Waters, F. Wildi, M. Willson, A. Zanutta, A. Zavagno, and A. Zurlo. SPHERE+: Imaging young Jupiters down to the snowline. page arXiv:2003.05714, 2020.

William J. Borucki, David Koch, Gibor Basri, Natalie Batalha, Timothy Brown, Douglas Caldwell, John Caldwell, Jørgen Christensen-Dalsgaard, William D. Cochran, Edna DeVore, Edward W. Dunham, Andrea K. Dupree, Thomas N. Gautier, John C. Geary, Ronald Gilliland, Alan Gould, Steve B. Howell, Jon M. Jenkins, Yoji Kondo, David W. Latham, Geoffrey W. Marcy, Søren Meibom, Hans Kjeldsen, Jack J. Lissauer, David G. Monet, David Morrison, Dimitar Sasselov, Jill Tarter, Alan Boss, Don Brownlee, Toby Owen, Derek Buzasi, David Charbonneau, Laurance Doyle, Jonathan Fortney, Eric B. Ford, Matthew J. Holman, Sara Seager, Jason H. Steffen, William F. Welsh, Jason Rowe, Howard Anderson, Lars Buchhave, David Ciardi, Lucianne Walkowicz, William Sherry, Elliott Horch, Howard Isaacson, Mark E. Everett, Debra Fischer, Guillermo Torres, John Asher Johnson, Michael Endl, Phillip MacQueen, Stephen T. Bryson, Jessie Dotson, Michael Haas, Jeffrey Kolodziejczak, Jeffrey Van Cleve, Hema Chandrasekaran, Joseph D. Twicken, Elisa V. Quintana, Bruce D. Clarke, Christopher Allen, Jie Li, Haley Wu, Peter Tenenbaum, Ekaterina Verner, Frederick Bruhweiler, Jason Barnes, and Andrej Prsa. Kepler Planet-Detection Mis-

sion: Introduction and First Results. *Science*, 327(5968):977, February 2010. doi: 10.1126/science.1185402.

A. P. Boss. Giant planet formation by gravitational instability. *Science*, 276: 1836–1839, January 1997. doi: 10.1126/science.276.5320.1836.

B. P. Bowler, M. C. Liu, T. J. Dupuy, and M. C. Cushing. Near-infrared Spectroscopy of the Extrasolar Planet HR 8799 b. *ApJ*, 723:850–868, November 2010. doi: 10.1088/0004-637X/723/1/850.

Brendan P. Bowler. Imaging Extrasolar Giant Planets. *PASP*, 128(968):102001, October 2016. doi: 10.1088/1538-3873/128/968/102001.

Brendan P. Bowler, Michael Endl, William D. Cochran, Phillip J. MacQueen, Justin R. Crepp, Greg W. Doppmann, Shannon Dulz, Timothy D. Brandt, G. Mirek Brandt, Yiting Li, Trent J. Dupuy, Kyle Franson, Kaitlin M. Kratter, Caroline V. Morley, and Yifan Zhou. The McDonald Accelerating Stars Survey (MASS): Discovery of a Long-period Substellar Companion Orbiting the Old Solar Analog HD 47127. *ApJL*, 913(2):L26, 2021. doi: 10.3847/2041-8213/abfec8.

T. D. Brandt. The Hipparcos–Gaia Catalog of Accelerations. *ApJS*, 239:31, December 2018. doi: 10.3847/1538-4365/aaec06.

T. D. Brandt and C. X. Huang. The Age and Age Spread of the Praesepe and Hyades Clusters: a Consistent, ˜800 Myr Picture from Rotating Stellar Models. *ApJ*, 807:24, July 2015a. doi: 10.1088/0004-637X/807/1/24.

T. D. Brandt and C. X. Huang. Bayesian Ages for Early-type Stars from Isochrones Including Rotation, and a Possible Old Age for the Hyades. *ApJ*, 807:58, July 2015b. doi: 10.1088/0004-637X/807/1/58.

T. D. Brandt, M. Rizzo, T. Groff, J. Chilcote, J. P. Greco, N. J. Kasdin, M. A. Limbach, M. Galvin, C. Loomis, G. Knapp, M. W. McElwain, N. Jovanovic, T. Currie, K. Mede, M. Tamura, N. Takato, and M. Hayashi. Data reduction pipeline for the CHARIS integral-field spectrograph I: detector readout calibration and data cube extraction. *Journal of Astronomical Telescopes, Instruments, and Systems*, 3(4):048002, October 2017. doi: 10.1117/1.JATIS.3.4.048002.

Timothy Brandt, Zackery Briesemeister, Dmitry Savransky, Michael Fitzgerald, Benjamin Mazin, Jonathan Fortney, Trent Dupuy, Brendan Bowler, Stephanie Sallum, Dimitri Mawet, Andrew Skemer, Gautam Vasisht, Max Miller-Blanchard, Jason Wang, Olivier Guyon, Tiffany Meshkat, Rebecca

Jensen-Clem, Eugene Serabyn, Garreth Ruane, Michael Liu, Nemanja Jovanovic, Caroline Morley, Marshall Perrin, Michael McElwain, Aki Roberge, Julien Girard, Laird Close, Henry Ngo, Mark Marley, Eduardo Bendek, Sam Ragland, and Laurent Pueyo. Realizing the Promise of High-Contrast Imaging: More Than 100 Gas-Giant Planets with Masses, Orbits, and Spectra Enabled by Gaia+WFIRST Astrometry. *BAAS*, 51(3):269, May 2019a.

Timothy D. Brandt. The Hipparcos-Gaia Catalog of Accelerations: Gaia EDR3 Edition. *ApJS*, 254(2):42, June 2021. doi: 10.3847/1538-4365/abf93c.

Timothy D. Brandt, Trent J. Dupuy, and Brendan P. Bowler. Precise Dynamical Masses of Directly Imaged Companions from Relative Astrometry, Radial Velocities, and Hipparcos-Gaia DR2 Accelerations. *AJ*, 158(4):140, 2019b. doi: 10.3847/1538-3881/ab04a8.

Zackery Briesemeister, Andrew J. Skemer, Jordan M. Stone, R. Deno Stelter, Philip Hinz, Jarron Leisenring, Michael F. Skrutskie, Charles E. Woodward, and Travis Barman. MEAD: data reduction pipeline for ALES integral field spectrograph and LBTI thermal infrared calibration unit. In Christopher J. Evans, Luc Simard, and Hideki Takami, editors, *Ground-based and Airborne Instrumentation for Astronomy VII*, volume 10702 of *Society of Photo-Optical Instrumentation Engineers (SPIE) Conference Series*, page 107022Q, July 2018. doi: 10.1117/12.2312859.

Zackery Briesemeister, Steph Sallum, Andrew Skemer, R. Deno Stelter, Philip Hinz, and Timothy Brandt. End-to-end simulation of the SCALES integral field spectrograph. In *Society of Photo-Optical Instrumentation Engineers (SPIE) Conference Series*, volume 11447 of *Society of Photo-Optical Instrumentation Engineers (SPIE) Conference Series*, page 114474Z, December 2020. doi: 10.1117/12.2562143.

Zackery Briesemeister, Steph Sallum, Andrew Skemer, and Natasha Batalha. Information content approach to trade studies for SCALES. volume 11823, pages 48 – 54. SPIE, 2021. doi: 10.1117/12.2594880. URL https://doi.org/10.1117/12.2594880.

Zackery W. Briesemeister, Andrew J. Skemer, Jordan M. Stone, Travis S. Barman, Philip Hinz, Jarron Leisenring, Michael F. Skrutskie, Charles E. Woodward, and Eckhart Spalding. High Spatial Resolution Thermal Infrared Spectroscopy with ALES: Resolved Spectra of the Benchmark Brown Dwarf Binary HD 130948BC. *AJ*, 157(6):244, June 2019. doi: 10.3847/1538-3881/ab1901.

Stephen P Brooks and Andrew Gelman. General methods for monitoring convergence of iterative simulations. *Journal of computational and graphical statistics*, 7(4):434–455, 1998.

A. Burrows and J. Liebert. The science of brown dwarfs. *Reviews of Modern Physics*, 65:301–336, April 1993. doi: 10.1103/RevModPhys.65.301.

A. Burrows, M. Marley, W. B. Hubbard, J. I. Lunine, T. Guillot, D. Saumon, R. Freedman, D. Sudarsky, and C. Sharp. A Nongray Theory of Extrasolar Giant Planets and Brown Dwarfs. *ApJ*, 491:856–875, December 1997. doi: 10.1086/305002.

A. Burrows, W. B. Hubbard, J. I. Lunine, and J. Liebert. The theory of brown dwarfs and extrasolar giant planets. *Reviews of Modern Physics*, 73:719–765, July 2001. doi: 10.1103/RevModPhys.73.719.

A. Burrows, K. Heng, and T. Nampaisarn. The Dependence of Brown Dwarf Radii on Atmospheric Metallicity and Clouds: Theory and Comparison with Observations. *ApJ*, 736:47, July 2011. doi: 10.1088/0004-637X/736/1/47.

F. Cantalloube, E. H. Por, K. Dohlen, J. F. Sauvage, A. Vigan, M. Kasper, N. Bharmal, T. Henning, W. Brandner, J. Milli, C. Correia, and T. Fusco. Origin of the asymmetry of the wind driven halo observed in high-contrast images. *AAP*, 620:L10, December 2018. doi: 10.1051/0004-6361/201834311.

F. Cantalloube, O. J. D. Farley, J. Milli, N. Bharmal, W. Brandner, C. Correia, K. Dohlen, Th. Henning, J. Osborn, E. Por, M. Suárez Valles, and A. Vigan. Wind-driven halo in high-contrast images. I. Analysis of the focal-plane images of SPHERE. *AAP*, 638:A98, June 2020. doi: 10.1051/0004-6361/201937397.

E. Carolo, D. Vassallo, J. Farinato, M. Bergomi, M. Bonavita, A. Carlotti, V. D'Orazi, D. Greggio, D. Magrin, D. Mesa, E. Pinna, A. Puglisi, M. Stangalini, C. Verinaud, and V. Viotto. A comparison between different coronagraphic data reduction techniques. In Enrico Marchetti, Laird M. Close, and Jean-Pierre Véran, editors, *Adaptive Optics Systems V*, volume 9909 of *Society of Photo-Optical Instrumentation Engineers (SPIE) Conference Series*, page 99097Q, July 2016. doi: 10.1117/12.2232792.

Stefano Casertano, Adam G. Riess, Jay Anderson, Richard I. Anderson, J. Bradley Bowers, Kelsey I. Clubb, Aviv R. Cukierman, Alexei V. Filippenko, Melissa L. Graham, John W. MacKenty, Carl Melis, Brad E. Tucker, and Gautam Upadhya. Parallax of Galactic Cepheids from Spatially Scanning the Wide Field Camera 3 on the Hubble Space Telescope: The Case of SS Canis Majoris. *ApJ*, 825(1):11, 2016. doi: 10.3847/0004-637X/825/1/11.

G. Chabrier, J. Gallardo, and I. Baraffe. Evolution of low-mass star and brown dwarf eclipsing binaries. *AAP*, 472:L17–L20, September 2007. doi: 10.1051/0004-6361:20077702.

G. Chauvin, A. M. Lagrange, C. Dumas, B. Zuckerman, D. Mouillet, I. Song, J. L. Beuzit, and P. Lowrance. A giant planet candidate near a young brown dwarf. Direct VLT/NACO observations using IR wavefront sensing. *AAP*, 425: L29–L32, October 2004. doi: 10.1051/0004-6361:200400056.

E. Chiang and A. N. Youdin. Forming Planetesimals in Solar and Extrasolar Nebulae. *Annual Review of Earth and Planetary Sciences*, 38:493–522, May 2010. doi: 10.1146/annurev-earth-040809-152513.

Jeffrey Chilcote, Quinn Konopacky, Robert J. De Rosa, Randall Hamper, Bruce Macintosh, Christian Marois, Marshall D. Perrin, Dmitry Savransky, Rémi Soummer, Jean-Pierre Véran, Guido Agapito, Arlene Aleman, S. Mark Ammons, Marco Bonaglia, Marc-Andre Boucher, Maeve Curliss, Jennifer Dunn, Simone Esposito, Guillaume Filion, Joeleff Fitzsimmons, Isabel Kain, Dan Kerley, Jean-Thomas Landry, Olivier Lardiere, Marie Lemoine-Busserolle, Duan Li, Mary Anne Limbach, Alex Madurowicz, Jerome Maire, Mamadou N'Diaye, Eric L. Nielsen, Lisa Poyneer, Laurent Pueyo, Kaitlyn Summey, and Coleman Thomas. GPI 2.0: upgrading the Gemini Planet Imager. 11447:114471S, 2020. doi: 10.1117/12.2562578.

R. U. Claudi, M. Turatto, R. G. Gratton, J. Antichi, M. Bonavita, P. Bruno, E. Cascone, V. De Caprio, S. Desidera, E. Giro, D. Mesa, S. Scuderi, K. Dohlen, J. L. Beuzit, and P. Puget. SPHERE IFS: the spectro differential imager of the VLT for exoplanets search. In *Ground-based and Airborne Instrumentation for Astronomy II*, volume 7014 of *Proc. SPIE*, page 70143E, July 2008. doi: 10.1117/12.788366.

M. Cohen, W. A. Wheaton, and S. T. Megeath. Spectral Irradiance Calibration in the Infrared. XIV. The Absolute Calibration of 2MASS. *AJ*, 126:1090–1096, August 2003. doi: 10.1086/376474.

Christopher J. Crockett, Naved I. Mahmud, L. Prato, Christopher M. Johns-Krull, Daniel T. Jaffe, Patrick M. Hartigan, and Charles A. Beichman. A Search for Giant Planet Companions to T Tauri Stars. *ApJ*, 761(2):164, December 2012. doi: 10.1088/0004-637X/761/2/164.

I. J. M. Crossfield. Doppler imaging of exoplanets and brown dwarfs. *AAP*, 566: A130, June 2014. doi: 10.1051/0004-6361/201423750.

Andrew Cumming, R. Paul Butler, Geoffrey W. Marcy, Steven S. Vogt, Jason T. Wright, and Debra A. Fischer. The Keck Planet Search: Detectability and the Minimum Mass and Orbital Period Distribution of Extrasolar Planets. *PASP*, 120(867):531, May 2008. doi: 10.1086/588487.

T. Currie, A. Burrows, Y. Itoh, S. Matsumura, M. Fukagawa, D. Apai, N. Madhusudhan, P. M. Hinz, T. J. Rodigas, M. Kasper, T.-S. Pyo, and S. Ogino. A Combined Subaru/VLT/MMT 1-5 μm Study of Planets Orbiting HR 8799: Implications for Atmospheric Properties, Masses, and Formation. *ApJ*, 729:128, March 2011. doi: 10.1088/0004-637X/729/2/128.

Thayne Currie, Christian Marois, Lucas Cieza, Gijs D. Mulders, Kellen Lawson, Claudio Caceres, Dary Rodriguez-Ruiz, John Wisniewski, Olivier Guyon, Timothy D. Brandt, N. Jeremy Kasdin, Tyler D. Groff, Julien Lozi, Jeffrey Chilcote, Klaus Hodapp, Nemanja Jovanovic, Frantz Martinache, Nour Skaf, Wladimir Lyra, Motohide Tamura, Ruben Asensio-Torres, Ruobing Dong, Carol Grady, Benjamin Gerard, Misato Fukagawa, Derek Hand, Masahiko Hayashi, Thomas Henning, Tomoyuki Kudo, Masayuki Kuzuhara, Jungmi Kwon, Michael W. McElwain, and Taichi Uyama. No Clear, Direct Evidence for Multiple Protoplanets Orbiting LkCa 15: LkCa 15 bcd are Likely Inner Disk Signals. *Astrophysical Journal*, 877(1):L3, May 2019. doi: 10.3847/2041-8213/ab1b42.

M. C. Cushing, M. S. Marley, D. Saumon, B. C. Kelly, W. D. Vacca, J. T. Rayner, R. S. Freedman, K. Lodders, and T. L. Roellig. Atmospheric Parameters of Field L and T Dwarfs. *ApJ*, 678:1372–1395, May 2008. doi: 10.1086/526489.

Michael C. Cushing, John T. Rayner, and William D. Vacca. An Infrared Spectroscopic Sequence of M, L, and T Dwarfs. *ApJ*, 623(2):1115–1140, April 2005. doi: 10.1086/428040.

I. Czekala, S. M. Andrews, K. S. Mandel, D. W. Hogg, and G. M. Green. Constructing a Flexible Likelihood Function for Spectroscopic Inference. *ApJ*, 812: 128, October 2015. doi: 10.1088/0004-637X/812/2/128.

Gennaro D'Angelo and Francesco Marzari. Outward Migration of Jupiter and Saturn in Evolved Gaseous Disks. *ApJ*, 757(1):50, September 2012. doi: 10.1088/0004-637X/757/1/50.

J. de Boer, G. Salter, M. Benisty, A. Vigan, A. Boccaletti, P. Pinilla, C. Ginski, A. Juhasz, A. L. Maire, S. Messina, S. Desidera, A. Cheetham, J. H. Girard, Z. Wahhaj, M. Langlois, M. Bonnefoy, J. L. Beuzit, E. Buenzli, G. Chauvin, C. Dominik, M. Feldt, R. Gratton, J. Hagelberg, A. Isella, M. Janson, C. U.

Keller, A. M. Lagrange, J. Lannier, F. Menard, D. Mesa, D. Mouillet, M. Mugrauer, S. Peretti, C. Perrot, E. Sissa, F. Snik, N. Vogt, A. Zurlo, and SPHERE Consortium. Multiple rings in the transition disk and companion candidates around RX J1615.3-3255. High contrast imaging with VLT/SPHERE. *AAP*, 595:A114, November 2016. doi: 10.1051/0004-6361/201629267.

K. de Kleer, M. Skrutskie, J. Leisenring, A. G. Davies, A. Conrad, I. de Pater, A. Resnick, V. Bailey, D. Defrère, P. Hinz, A. Skemer, E. Spalding, A. Vaz, C. Veillet, and C. E. Woodward. Multi-phase volcanic resurfacing at Loki Patera on Io. *Nature*, 545(7653):199–202, May 2017. doi: 10.1038/nature22339.

D. Defrère, O. Absil, P. Hinz, J. Kuhn, D. Mawet, B. Mennesson, A. Skemer, K. Wallace, V. Bailey, E. Downey, C. Delacroix, O. Durney, P. Forsberg, C. Gomez, S. Habraken, W. F. Hoffmann, M. Karlsson, M. Kenworthy, J. Leisenring, M. Montoya, L. Pueyo, M. Skrutskie, and J. Surdej. L'-band AGPM vector vortex coronagraph's first light on LBTI/LMIRCam. In *Adaptive Optics Systems IV*, volume 9148 of *Proc. SPIE*, page 91483X, July 2014. doi: 10.1117/12.2057205.

Sarah E. Dodson-Robinson and Colette Salyk. Transitional Disks as Signposts of Young, Multiplanet Systems. *ApJ*, 738(2):131, September 2011. doi: 10.1088/0004-637X/738/2/131.

D. S. Doelman, F. Snik, E. H. Por, S. P. Bos, G. P. P. L. Otten, M. Kenworthy, S. Y. Haffert, M. Wilby, A. J. Bohn, B. J. Sutlieff, K. Miller, M. Ouellet, J. de Boer, C. U. Keller, M. J. Escuti, S. Shi, N. Z. Warriner, K. Hornburg, J. L. Birkby, J. Males, K. M. Morzinski, L. M. Close, J. Codona, J. Long, L. Schatz, J. Lumbres, A. Rodack, K. Van Gorkom, A. Hedglen, O. Guyon, J. Lozi, T. Groff, J. Chilcote, N. Jovanovic, S. Thibault, C. de Jonge, G. Allain, C. Vallée, D. Patel, O. Côté, C. Marois, P. Hinz, J. Stone, A. Skemer, Z. Briesemeister, A. Boehle, A. M. Glauser, W. Taylor, P. Baudoz, E. Huby, O. Absil, B. Carlomagno, and C. Delacroix. Vector-apodizing phase plate coronagraph: design, current performance, and future development [Invited]. *AO*, 60(19):D52, July 2021. doi: 10.1364/AO.422155.

David S. Doelman, Jordan M. Stone, Zackery W. Briesemeister, Andrew J. I. Skemer, Travis Barman, Laci S. Brock, Philip M. Hinz, Alexander Bohn, Matthew Kenworthy, Sebastiaan Y. Haffert, Frans Snik, Steve Ertel, Jarron M. Leisenring, Charles E. Woodward, and Michael F. Skrutskie. L-band Integral Field Spectroscopy of the HR 8799 Planetary System. *AJ*, 163(5):217, May 2022. doi: 10.3847/1538-3881/ac5d52.

Olivier Doré, Christopher Hirata, Yun Wang, David Weinberg, Ivano Baronchelli, Andrew Benson, Peter Capak, Ami Choi, Tim Eifler, Shoubaneh Hemmati, Shirley Ho, Albert Izard, Bhuvnesh Jain, Mike Jarvis, Alina Kiessling, Elisabeth Krause, Elena Massara, Dan Masters, Alex Merson, Hironao Miyatake, Andres Plazas Malagon, Rachel Mandelbaum, Lado Samushia, Chaz Shapiro, Melanie Simet, David Spergel, Harry Teplitz, Michael Troxel, Rachel Bean, James Colbert, Chen He Heinrich, Katrin Heitmann, George Helou, Michael Hudson, Eric Huff, Alexie Leauthaud, Niall MacCrann, Nikhil Padmanabhan, Alice Pisani, Jason Rhodes, Eduardo Rozo, Mike Seiffert, Kendrick Smith, Masahiro Takada, Anja von der Linden, Robert Lupton, Naoki Yoshida, Hao-Yi Wu, and Ying Zu. WFIRST Science Investigation Team "Cosmology with the High Latitude Survey" Annual Report 2017. page arXiv:1804.03628, 2018.

S. T. Douglas, M. A. Agüeros, K. R. Covey, P. A. Cargile, T. Barclay, A. Cody, S. B. Howell, and T. Kopytova. K2 Rotation Periods for Low-mass Hyads and the Implications for Gyrochronology. *ApJ*, 822:47, May 2016. doi: 10.3847/0004-637X/822/1/47.

Z. H. Draper, C. Marois, S. Wolff, M. Perrin, P. J. Ingraham, J.-B. Ruffio, F. T. Rantakyro, M. Hartung, and S. J. Goodsell. Gemini planet imager observational calibrations IX: least-squares inversion flux extraction. In *Ground-based and Airborne Instrumentation for Astronomy V*, volume 9147 of *Proc. SPIE*, page 91474Z, July 2014. doi: 10.1117/12.2057156.

T. J. Dupuy and A. L. Kraus. Distances, Luminosities, and Temperatures of the Coldest Known Substellar Objects. *Science*, 341:1492–1495, September 2013. doi: 10.1126/science.1241917.

T. J. Dupuy and M. C. Liu. The Hawaii Infrared Parallax Program. I. Ultracool Binaries and the L/T Transition. *ApJS*, 201:19, August 2012. doi: 10.1088/0067-0049/201/2/19.

T. J. Dupuy and M. C. Liu. Individual Dynamical Masses of Ultracool Dwarfs. *ApJS*, 231:15, August 2017. doi: 10.3847/1538-4365/aa5e4c.

T. J. Dupuy, M. C. Liu, and M. J. Ireland. Dynamical Mass of the Substellar Benchmark Binary HD 130948BC. *ApJ*, 692:729–752, February 2009. doi: 10.1088/0004-637X/692/1/729.

T. J. Dupuy, M. C. Liu, B. P. Bowler, M. C. Cushing, C. Helling, S. Witte, and P. Hauschildt. Studying the Physical Diversity of Late-M Dwarfs with Dynamical Masses. *ApJ*, 721:1725–1747, October 2010. doi: 10.1088/0004-637X/721/2/1725.

T. J. Dupuy, M. C. Liu, and M. J. Ireland. Testing Theory with Dynamical Masses and Orbits of Ultracool Binaries. In C. Johns-Krull, M. K. Browning, and A. A. West, editors, *16th Cambridge Workshop on Cool Stars, Stellar Systems, and the Sun*, volume 448 of *Astronomical Society of the Pacific Conference Series*, page 111, December 2011.

T. J. Dupuy, M. C. Liu, and M. J. Ireland. New Evidence for a Substellar Luminosity Problem: Dynamical Mass for the Brown Dwarf Binary Gl 417BC. *ApJ*, 790:133, August 2014. doi: 10.1088/0004-637X/790/2/133.

C. Eiroa, J. P. Marshall, A. Mora, B. Montesinos, O. Absil, J. C. Augereau, A. Bayo, G. Bryden, W. Danchi, C. del Burgo, S. Ertel, M. Fridlund, A. M. Heras, A. V. Krivov, R. Launhardt, R. Liseau, T. Löhne, J. Maldonado, G. L. Pilbratt, A. Roberge, J. Rodmann, J. Sanz-Forcada, E. Solano, K. Stapelfeldt, P. Thébault, S. Wolf, D. Ardila, M. Arévalo, C. Beichmann, V. Faramaz, B. M. González-García, R. Gutiérrez, J. Lebreton, R. Martínez-Arnáiz, G. Meeus, D. Montes, G. Olofsson, K. Y. L. Su, G. J. White, D. Barrado, M. Fukagawa, E. Grün, I. Kamp, R. Lorente, A. Morbidelli, S. Müller, H. Mutschke, T. Nakagawa, I. Ribas, and H. Walker. DUst around NEarby Stars. The survey observational results. *AAP*, 555:A11, July 2013. doi: 10.1051/0004-6361/201321050.

S. Esposito, A. Riccardi, E. Pinna, A. Puglisi, F. Quirós-Pacheco, C. Arcidiacono, M. Xompero, R. Briguglio, G. Agapito, L. Busoni, L. Fini, J. Argomedo, A. Gherardi, G. Brusa, D. Miller, J. C. Guerra, P. Stefanini, and P. Salinari. Large Binocular Telescope Adaptive Optics System: new achievements and perspectives in adaptive optics. In *Astronomical Adaptive Optics Systems and Applications IV*, volume 8149 of *Proc. SPIE*, page 814902, October 2011. doi: 10.1117/12.898641.

J. K. Faherty, K. L. Cruz, E. L. Rice, and A. Riedel. Young brown dwarfs as giant exoplanet analogs . *Memorie della Societa Astronomica Italiana*, 84:955, 2013.

Rachel B. Fernandes, Gijs D. Mulders, Ilaria Pascucci, Christoph Mordasini, and Alexandre Emsenhuber. Hints for a Turnover at the Snow Line in the Giant Planet Occurrence Rate. *ApJ*, 874(1):81, March 2019. doi: 10.3847/1538-4357/ab0300.

Debra A. Fischer and Jeff Valenti. The Planet-Metallicity Correlation. *ApJ*, 622 (2):1102–1117, April 2005. doi: 10.1086/428383.

D. Foreman-Mackey. corner.py: Scatterplot matrices in Python. *The Journal of Open Source Software*, 1, June 2016. doi: 10.21105/joss.00024.

D. Foreman-Mackey, D. W. Hogg, D. Lang, and J. Goodman. emcee: The MCMC Hammer. *PASP*, 125:306, March 2013. doi: 10.1086/670067.

J. J. Fortney, M. S. Marley, D. Saumon, and K. Lodders. Synthetic Spectra and Colors of Young Giant Planet Atmospheres: Effects of Initial Conditions and Atmospheric Metallicity. *ApJ*, 683(2):1104–1116, August 2008. doi: 10.1086/589942.

François Fressin, Guillermo Torres, David Charbonneau, Stephen T. Bryson, Jessie Christiansen, Courtney D. Dressing, Jon M. Jenkins, Lucianne M. Walkowicz, and Natalie M. Batalha. The False Positive Rate of Kepler and the Occurrence of Planets. *ApJ*, 766(2):81, April 2013. doi: 10.1088/0004-637X/766/2/81.

Gaia Collaboration, A. G. A. Brown, A. Vallenari, T. Prusti, J. H. J. de Bruijne, F. Mignard, R. Drimmel, C. Babusiaux, C. A. L. Bailer-Jones, U. Bastian, and et al. Gaia Data Release 1. Summary of the astrometric, photometric, and survey properties. *AAP*, 595:A2, November 2016. doi: 10.1051/0004-6361/201629512.

Gaia Collaboration, A. G. A. Brown, A. Vallenari, T. Prusti, J. H. J. de Bruijne, C. Babusiaux, and C. A. L. Bailer-Jones. Gaia Data Release 2. Summary of the contents and survey properties. *ArXiv e-prints*, April 2018.

E. J. Gaidos, G. W. Henry, and S. M. Henry. Spectroscopy and Photometry of Nearby Young Solar Analogs. *AJ*, 120:1006–1013, August 2000. doi: 10.1086/301488.

R. Galicher, C. Marois, B. Macintosh, B. Zuckerman, T. Barman, Q. Konopacky, I. Song, J. Patience, D. Lafrenière, R. Doyon, and E. L. Nielsen. The International Deep Planet Survey. II. The frequency of directly imaged giant exoplanets with stellar mass. *AAP*, 594:A63, October 2016. doi: 10.1051/0004-6361/201527828.

K. Geißler, M. R. Sterzik, G. Chauvin, and E. Pantin. Mid-infrared imaging of brown dwarfs: Is HD 130948 BC variable? In E. Stempels, editor, *15th Cambridge Workshop on Cool Stars, Stellar Systems, and the Sun*, volume 1094 of *American Institute of Physics Conference Series*, pages 521–524, February 2009. doi: 10.1063/1.3099163.

A. Gelman and D. B. Rubin. Inference from Iterative Simulation Using Multiple Sequences. *Statistical Science*, 7:457–472, 1992. doi: 10.1214/ss/1177011136.

Elizabeth M. George, Simon M. Tulloch, and Derek J. Ives. Fast method of crosstalk characterization for HxRG detectors. *arXiv e-prints*, art. arXiv:1808.00790, August 2018.

C. Ginski, R. Neuhäuser, M. Mugrauer, T. O. B. Schmidt, and C. Adam. Orbital motion of the binary brown dwarf companions HD 130948 BC around their host star. *MNRAS*, 434:671–683, September 2013. doi: 10.1093/mnras/stt1059.

D. A. Golimowski, S. K. Leggett, M. S. Marley, X. Fan, T. R. Geballe, G. R. Knapp, F. J. Vrba, A. A. Henden, C. B. Luginbuhl, H. H. Guetter, J. A. Munn, B. Canzian, W. Zheng, Z. I. Tsvetanov, K. Chiu, K. Glazebrook, E. A. Hoversten, D. P. Schneider, and J. Brinkmann. L' and M' Photometry of Ultracool Dwarfs. *AJ*, 127:3516–3536, June 2004. doi: 10.1086/420709.

R. Gomes, H. F. Levison, K. Tsiganis, and A. Morbidelli. Origin of the cataclysmic Late Heavy Bombardment period of the terrestrial planets. *Nature*, 435(7041): 466–469, May 2005. doi: 10.1038/nature03676.

C. A. Gomez Gonzalez, O. Absil, P.-A. Absil, M. Van Droogenbroeck, D. Mawet, and J. Surdej. Low-rank plus sparse decomposition for exoplanet detection in direct-imaging ADI sequences. The LLSG algorithm. *AAP*, 589:A54, May 2016. doi: 10.1051/0004-6361/201527387.

Carlos Alberto Gomez Gonzalez, Olivier Wertz, Olivier Absil, Valentin Christiaens, Denis Defrère, Dimitri Mawet, Julien Milli, Pierre-Antoine Absil, Marc Van Droogenbroeck, Faustine Cantalloube, Philip M. Hinz, Andrew J. Skemer, Mikael Karlsson, and Jean Surdej. Vip : Vortex image processing package for high-contrast direct imaging. *The Astronomical Journal*, 154(1):7, 2017. URL http://stacks.iop.org/1538-3881/154/i=1/a=7.

J. Goodman and J. Weare. Ensemble samplers with affine invariance. *Communications in Applied Mathematics and Computational Science, Vol. 5, No. 1, p. 65-80, 2010*, 5:65–80, 2010. doi: 10.2140/camcos.2010.5.65.

S. Gossage, C. Conroy, A. Dotter, J. Choi, P. Rosenfield, P. Cargile, and A. Dolphin. Age Determinations of the Hyades, Praesepe, and Pleiades via MESA Models with Rotation. *ApJ*, 863:67, August 2018. doi: 10.3847/1538-4357/aad0a0.

M. Goto, N. Kobayashi, H. Terada, W. Gaessler, T. Kanzawa, H. Takami, N. Takato, Y. Hayano, Y. Kamata, M. Iye, D. J. Saint-Jacques, A. T. Tokunaga, D. Potter, and M. Cushing. Near-Infrared Adaptive Optics Spectroscopy of Binary Brown Dwarfs HD 130948B and HD 130948C. *ApJL*, 567:L59–L62, March 2002. doi: 10.1086/339800.

J. P. Greco and T. D. Brandt. The Measurement, Treatment, and Impact of Spectral Covariance and Bayesian Priors in Integral-field Spectroscopy of Exoplanets. *ApJ*, 833:134, December 2016. doi: 10.3847/1538-4357/833/2/134.

Manuel Guizar-Sicairos, Samuel T Thurman, and James R Fienup. Efficient subpixel image registration algorithms. *Optics letters*, 33(2):156–8, jan 2008. ISSN 0146-9592.

P. H. Hauschildt, F. Allard, and E. Baron. The NextGen Model Atmosphere Grid for 3000≤T_{eff} ≤10,000 K. *ApJ*, 512:377–385, February 1999. doi: 10.1086/306745.

Christiane Helling and Sarah Casewell. Atmospheres of brown dwarfs. *AAPR*, 22:80, November 2014. doi: 10.1007/s00159-014-0080-0.

Patrick Hennebelle and Gilles Chabrier. Analytical Theory for the Initial Mass Function: CO Clumps and Prestellar Cores. *ApJ*, 684(1):395–410, September 2008. doi: 10.1086/589916.

S. Hinkley, B. R. Oppenheimer, N. Zimmerman, D. Brenner, I. R. Parry, J. R. Crepp, G. Vasisht, E. Ligon, D. King, R. Soummer, A. Sivaramakrishnan, C. Beichman, M. Shao, L. C. Roberts, Jr., A. Bouchez, R. Dekany, L. Pueyo, J. E. Roberts, T. Lockhart, C. Zhai, C. Shelton, and R. Burruss. A New High Contrast Imaging Program at Palomar Observatory. *PASP*, 123:74, January 2011. doi: 10.1086/658163.

P. Hinz, P. Arbo, V. Bailey, T. Connors, O. Durney, S. Esposito, W. Hoffmann, T. Jones, J. Leisenring, M. Montoya, M. Nash, M. Nelson, T. McMahon, E. Pinna, A. Puglisi, A. Skemer, M. Skrutskie, and V. Vaitheeswaran. First AO-corrected interferometry with LBTI: steps towards routine coherent imaging observations. In *Optical and Infrared Interferometry III*, volume 8445 of *Proc. SPIE*, page 84450U, July 2012. doi: 10.1117/12.926746.

P. Hinz, V. P. Bailey, D. Defrère, E. Downey, S. Esposito, J. Hill, W. F. Hoffmann, J. Leisenring, M. Montoya, T. McMahon, A. Puglisi, A. Skemer, M. Skrutskie, V. Vaitheeswaran, and A. Vaz. Commissioning the LBTI for use as a nulling interferometer and coherent imager. In *Optical and Infrared Interferometry IV*, volume 9146 of *Proc. SPIE*, page 91460T, July 2014. doi: 10.1117/12.2057340.

P. M. Hinz, T. Bippert-Plymate, A. Breuninger, T. Connors, B. Duffy, S. Esposito, W. Hoffmann, J. Kim, J. Kraus, T. McMahon, M. Montoya, R. Nash, O. Durney, E. Solheid, A. Tozzi, and V. Vaitheeswaran. Status of the LBT interferometer. In *Optical and Infrared Interferometry*, volume 7013 of *Proc. SPIE*, page 701328, July 2008a. doi: 10.1117/12.790211.

P. M. Hinz, E. Solheid, O. Durney, and W. F. Hoffmann. NIC: LBTI's nulling and imaging camera. In *Optical and Infrared Interferometry*, volume 7013 of *Proc. SPIE*, page 701339, July 2008b. doi: 10.1117/12.790242.

P. M. Hinz, D. Defrère, A. Skemer, V. Bailey, J. Stone, E. Spalding, A. Vaz, E. Pinna, A. Puglisi, S. Esposito, M. Montoya, E. Downey, J. Leisenring, O. Durney, W. Hoffmann, J. Hill, R. Millan-Gabet, B. Mennesson, W. Danchi, K. Morzinski, P. Grenz, M. Skrutskie, and S. Ertel. Overview of LBTI: a multi-purpose facility for high spatial resolution observations. In *Optical and Infrared Interferometry and Imaging V*, volume 9907 of *Proc. SPIE*, page 990704, August 2016. doi: 10.1117/12.2233795.

P. M. Hinz, A. Skemer, J. Stone, O. M. Montoya, and O. Durney. Design of ALES: a broad wavelength integral field unit for LBTI/LMIRcam. In *Society of Photo-Optical Instrumentation Engineers (SPIE) Conference Series*, volume 10702 of *Society of Photo-Optical Instrumentation Engineers (SPIE) Conference Series*, page 107023L, July 2018. doi: 10.1117/12.2314289.

K. Horne. An optimal extraction algorithm for CCD spectroscopy. *PASP*, 98: 609–617, June 1986. doi: 10.1086/131801.

Alex R. Howe, Adam Burrows, and Drake Deming. An Information-theoretic Approach to Optimize JWST Observations and Retrievals of Transiting Exoplanet Atmospheres. *ApJ*, 835(1):96, January 2017. doi: 10.3847/1538-4357/835/1/96.

Renyu Hu. Information in the Reflected-light Spectra of Widely Separated Giant Exoplanets. *ApJ*, 887(2):166, December 2019. doi: 10.3847/1538-4357/ab58c7.

J. D. Hunter. Matplotlib: A 2d graphics environment. *Computing In Science & Engineering*, 9(3):90–95, 2007. doi: 10.1109/MCSE.2007.55.

P. Ingraham, M. S. Marley, D. Saumon, C. Marois, B. Macintosh, T. Barman, B. Bauman, A. Burrows, J. K. Chilcote, R. J. De Rosa, D. Dillon, R. Doyon, J. Dunn, D. Erikson, M. P. Fitzgerald, D. Gavel, S. J. Goodsell, J. R. Graham, M. Hartung, P. Hibon, P. G. Kalas, Q. Konopacky, J. A. Larkin, J. Maire, F. Marchis, J. McBride, M. Millar-Blanchaer, K. M. Morzinski, A. Norton, R. Oppenheimer, D. W. Palmer, J. Patience, M. D. Perrin, L. A. Poyneer, L. Pueyo, F. Rantakyrö, N. Sadakuni, L. Saddlemyer, D. Savransky, R. Soummer, A. Sivaramakrishnan, I. Song, S. Thomas, J. K. Wallace, S. J. Wiktorowicz, and S. G. Wolff. Gemini Planet Imager Spectroscopy of the HR 8799 Planets c and d. *ApJL*, 794:L15, October 2014. doi: 10.1088/2041-8205/794/1/L15.

Rebecca Jensen-Clem, Dimitri Mawet, Carlos A. Gomez Gonzalez, Olivier Absil, Ruslan Belikov, Thayne Currie, Matthew A. Kenworthy, Christian Marois, Johan Mazoyer, Garreth Ruane, Angelle Tanner, and Faustine Cantalloube. A New Standard for Assessing the Performance of High Contrast Imaging Systems. *AJ*, 155(1):19, January 2018. doi: 10.3847/1538-3881/aa97e4.

John D. Johnston, Joseph M. Howard, Gary E. Mosier, Keith A. Parrish, Mark A. McGinnis, A. Marcel Bluth, Kevin Kim, and Kong Q. Ha. Integrated modeling activities for the James Webb Space Telescope: structural-thermal-optical analysis. volume 5487, pages 600 – 610. Proc. SPIE, 2004. doi: 10.1117/12.551704. URL https://doi.org/10.1117/12.551704.

Eric Jones, Travis Oliphant, Pearu Peterson, et al. SciPy: Open source scientific tools for Python, 2001–. URL http://www.scipy.org/. [Online; accessed <today>].

M. Keppler, M. Benisty, A. Müller, Th. Henning, R. van Boekel, F. Cantalloube, C. Ginski, R. G. van Holstein, A. L. Maire, A. Pohl, M. Samland, H. Avenhaus, J. L. Baudino, A. Boccaletti, J. de Boer, M. Bonnefoy, G. Chauvin, S. Desidera, M. Langlois, C. Lazzoni, G. D. Marleau, C. Mordasini, N. Pawellek, T. Stolker, A. Vigan, A. Zurlo, T. Birnstiel, W. Brandner, M. Feldt, M. Flock, J. Girard, R. Gratton, J. Hagelberg, A. Isella, M. Janson, A. Juhasz, J. Kemmer, Q. Kral, A. M. Lagrange, R. Launhardt, A. Matter, F. Ménard, J. Milli, P. Mollière, J. Olofsson, L. Pérez, P. Pinilla, C. Pinte, S. P. Quanz, T. Schmidt, S. Udry, Z. Wahhaj, J. P. Williams, E. Buenzli, M. Cudel, C. Dominik, R. Galicher, M. Kasper, J. Lannier, D. Mesa, D. Mouillet, S. Peretti, C. Perrot, G. Salter, E. Sissa, F. Wildi, L. Abe, J. Antichi, J. C. Augereau, A. Baruffolo, P. Baudoz, A. Bazzon, J. L. Beuzit, P. Blanchard, S. S. Brems, T. Buey, V. De Caprio, M. Carbillet, M. Carle, E. Cascone, A. Cheetham, R. Claudi, A. Costille, A. Delboulbé, K. Dohlen, D. Fantinel, P. Feautrier, T. Fusco, E. Giro, L. Gluck, C. Gry, N. Hubin, E. Hugot, M. Jaquet, D. Le Mignant, M. Llored, F. Madec, Y. Magnard, P. Martinez, D. Maurel, M. Meyer, O. Möller-Nilsson, T. Moulin, L. Mugnier, A. Origné, A. Pavlov, D. Perret, C. Petit, J. Pragt, P. Puget, P. Rabou, J. Ramos, F. Rigal, S. Rochat, R. Roelfsema, G. Rousset, A. Roux, B. Salasnich, J. F. Sauvage, A. Sevin, C. Soenke, E. Stadler, M. Suarez, M. Turatto, and L. Weber. Discovery of a planetary-mass companion within the gap of the transition disk around PDS 70. *AAP*, 617:A44, 2018. doi: 10.1051/0004-6361/201832957.

S. Kiefer, A. J. Bohn, S. P. Quanz, M. Kenworthy, and T. Stolker. Spectral and angular differential imaging with SPHERE/IFS. Assessing the performance of

various PCA-based approaches to PSF subtraction. *AAP*, 652:A33, August 2021. doi: 10.1051/0004-6361/202140285.

Wilhelm Kley. Planet formation and disk-planet interactions. *arXiv e-prints*, art. arXiv:1707.07148, July 2017.

G. R. Knapp, S. K. Leggett, X. Fan, M. S. Marley, T. R. Geballe, D. A. Golimowski, D. Finkbeiner, J. E. Gunn, J. Hennawi, Z. Ivezić, R. H. Lupton, D. J. Schlegel, M. A. Strauss, Z. I. Tsvetanov, K. Chiu, E. A. Hoversten, K. Glazebrook, W. Zheng, M. Hendrickson, C. C. Williams, A. Uomoto, F. J. Vrba, A. A. Henden, C. B. Luginbuhl, H. H. Guetter, J. A. Munn, B. Canzian, D. P. Schneider, and J. Brinkmann. Near-Infrared Photometry and Spectroscopy of L and T Dwarfs: The Effects of Temperature, Clouds, and Gravity. *AJ*, 127:3553–3578, June 2004. doi: 10.1086/420707.

Maciej Konacki, Guillermo Torres, Saurabh Jha, and Dimitar D. Sasselov. An extrasolar planet that transits the disk of its parent star. *Nature*, 421(6922): 507–509, January 2003. doi: 10.1038/nature01379.

Q. M. Konopacky, A. M. Ghez, T. S. Barman, E. L. Rice, J. I. Bailey, III, R. J. White, I. S. McLean, and G. Duchêne. High-precision Dynamical Masses of Very Low Mass Binaries. *ApJ*, 711:1087–1122, March 2010. doi: 10.1088/0004-637X/711/2/1087.

Quinn M. Konopacky, Travis S. Barman, Bruce A. Macintosh, and Christian Marois. Detection of Carbon Monoxide and Water Absorption Lines in an Exoplanet Atmosphere. *Science*, 339(6126):1398–1401, 2013. doi: 10.1126/science.1232003.

Rubina Kotak, Peter Meikle, Schuyler D. van Dyk, Peter A. Höflich, and Seppo Mattila. Early-Time Spitzer Observations of the Type II Plateau Supernova SN 2004dj. *ApJ*, 628(2):L123–L126, August 2005. doi: 10.1086/432719.

J. E. Krist, C. A. Beichman, J. T. Trauger, M. J. Rieke, S. Somerstein, J. J. Green, S. D. Horner, J. A. Stansberry, F. Shi, M. R. Meyer, K. R. Stapelfeldt, and T. L. Roellig. Hunting planets and observing disks with the JWST NIRCam coronagraph. In *Techniques and Instrumentation for Detection of Exoplanets III*, volume 6693 of *Proc. SPIE*, page 66930H, September 2007. doi: 10.1117/12.734873.

D. Lafrenière, C. Marois, R. Doyon, D. Nadeau, and É. Artigau. A New Algorithm for Point-Spread Function Subtraction in High-Contrast Imaging: A Demonstration with Angular Differential Imaging. *ApJ*, 660:770–780, May 2007. doi: 10.1086/513180.

J. Larkin, M. Barczys, A. Krabbe, S. Adkins, T. Aliado, P. Amico, G. Brims, R. Campbell, J. Canfield, T. Gasaway, A. Honey, C. Iserlohe, C. Johnson, E. Kress, D. LaFreniere, J. Lyke, K. Magnone, N. Magnone, M. McElwain, J. Moon, A. Quirrenbach, G. Skulason, I. Song, M. Spencer, J. Weiss, and S. Wright. OSIRIS: a diffraction limited integral field spectrograph for Keck. In *Society of Photo-Optical Instrumentation Engineers (SPIE) Conference Series*, volume 6269 of *Proc. SPIE*, page 62691A, June 2006. doi: 10.1117/12.672061.

R. Launhardt, Th. Henning, A. Quirrenbach, D. Ségransan, H. Avenhaus, R. van Boekel, S. S. Brems, A. C. Cheetham, G. Cugno, J. Girard, N. Godoy, G. M. Kennedy, A. L. Maire, S. Metchev, A. Müller, A. Musso Barcucci, J. Olofsson, F. Pepe, S. P. Quanz, D. Queloz, S. Reffert, E. L. Rickman, H. L. Ruh, and M. Samland. ISPY-NACO Imaging Survey for Planets around Young stars. Survey description and results from the first 2.5 years of observations. *AAP*, 635:A162, March 2020. doi: 10.1051/0004-6361/201937000.

S. K. Leggett, D. A. Golimowski, X. Fan, T. R. Geballe, G. R. Knapp, J. Brinkmann, I. Csabai, J. E. Gunn, S. L. Hawley, T. J. Henry, R. Hindsley, Ž. Ivezić, R. H. Lupton, J. R. Pier, D. P. Schneider, J. A. Smith, M. A. Strauss, A. Uomoto, and D. G. York. Infrared Photometry of Late-M, L, and T Dwarfs. *ApJ*, 564:452–465, January 2002. doi: 10.1086/324037.

J. M. Leisenring, M. J. Nelson, W. F. Hoffmann, J. Schoenwald, A. Wong, and M. F. Skrutskie. Integration and characterization of HAWAII-1RG detector with FORCAST fast-readout electronics for LMIRcam. In *Ground-based and Airborne Instrumentation for Astronomy III*, volume 7735 of *Proc. SPIE*, page 77352N, July 2010. doi: 10.1117/12.857615.

J. M. Leisenring, M. F. Skrutskie, P. M. Hinz, A. Skemer, V. Bailey, J. Eisner, P. Garnavich, W. F. Hoffmann, T. Jones, M. Kenworthy, P. Kuzmenko, M. Meyer, M. Nelson, T. J. Rodigas, J. C. Wilson, and V. Vaitheeswaran. On-sky operations and performance of LMIRcam at the Large Binocular Telescope. In *Ground-based and Airborne Instrumentation for Astronomy IV*, volume 8446 of *Proc. SPIE*, page 84464F, September 2012. doi: 10.1117/12.924814.

J. M. Leisenring, P. M. Hinz, M. Skrutskie, A. Skemer, C. E. Woodward, C. Veillet, C. Arcidiacono, V. Bailey, M. Bertero, P. Boccacci, A. Conrad, K. de Kleer, I. de Pater, D. Defrère, J. Hill, K.-H. Hofmann, L. Kaltenegger, A. La Camera, M. J. Nelson, D. Schertl, J. Spencer, G. Weigelt, and J. C. Wilson. Fizeau interferometric imaging of Io volcanism with LBTI/LMIRcam. In *Optical and Infrared Interferometry IV*, volume 9146 of *Proc. SPIE*, page 91462S, July 2014. doi: 10.1117/12.2057290.

Harold F. Levison, Alessandro Morbidelli, Christa Van Laerhoven, Rodney Gomes, and Kleomenis Tsiganis. Origin of the structure of the Kuiper belt during a dynamical instability in the orbits of Uranus and Neptune. *Icarus*, 196 (1):258–273, July 2008. doi: 10.1016/j.icarus.2007.11.035.

L. Lindegren, U. Lammers, D. Hobbs, W. O'Mullane, U. Bastian, and J. Hernández. The astrometric core solution for the Gaia mission. Overview of models, algorithms, and software implementation. *AAP*, 538:A78, February 2012. doi: 10.1051/0004-6361/201117905.

L. Lindegren, J. Hernández, A. Bombrun, S. Klioner, U. Bastian, M. Ramos-Lerate, A. de Torres, H. Steidelmüller, C. Stephenson, D. Hobbs, U. Lammers, M. Biermann, R. Geyer, T. Hilger, D. Michalik, U. Stampa, P. J. McMillan, J. Castañeda, M. Clotet, G. Comoretto, M. Davidson, C. Fabricius, G. Gracia, N. C. Hambly, A. Hutton, A. Mora, J. Portell, F. van Leeuwen, U. Abbas, A. Abreu, M. Altmann, A. Andrei, E. Anglada, L. Balaguer-Núñez, C. Barache, U. Becciani, S. Bertone, L. Bianchi, S. Bouquillon, G. Bourda, T. Brüsemeister, B. Bucciarelli, D. Busonero, R. Buzzi, R. Cancelliere, T. Carlucci, P. Charlot, N. Cheek, M. Crosta, C. Crowley, J. de Bruijne, F. de Felice, R. Drimmel, P. Esquej, A. Fienga, E. Fraile, M. Gai, N. Garralda, J. J. González-Vidal, R. Guerra, M. Hauser, W. Hofmann, B. Holl, S. Jordan, M. G. Lattanzi, H. Lenhardt, S. Liao, E. Licata, T. Lister, W. Löffler, J. Marchant, J. M. Martin-Fleitas, R. Messineo, F. Mignard, R. Morbidelli, E. Poggio, A. Riva, N. Rowell, E. Salguero, M. Sarasso, E. Sciacca, H. Siddiqui, R. L. Smart, A. Spagna, I. Steele, F. Taris, J. Torra, A. van Elteren, W. van Reeven, and A. Vecchiato. Gaia Data Release 2. The astrometric solution. *AAP*, 616:A2, 2018. doi: 10.1051/0004-6361/201832727.

M. C. Liu, T. J. Dupuy, and K. N. Allers. The Hawaii Infrared Parallax Program. II. Young Ultracool Field Dwarfs. *ApJ*, 833:96, December 2016. doi: 10.3847/1538-4357/833/1/96.

M. Loose, J. Beletic, J. Blackwell, J. Garnett, S. Wong, D. Hall, S. Jacobson, M. Rieke, and G. Winters. The SIDECAR ASIC: focal plane electronics on a single chip. In J. B. Heaney and L. G. Burriesci, editors, *Cryogenic Optical Systems and Instruments XI*, volume 5904 of *Proc. SPIE*, pages 293–302, August 2005. doi: 10.1117/12.619638.

Steven D. Lord. A new software tool for computing Earth's atmospheric transmission of near- and far-infrared radiation. NASA Technical Memorandum 103957, December 1992.

F. J. Low and A. W. Davidson. The Thermal Emission of Jupiter and Saturn. In *Bulletin of the American Astronomical Society*, volume 1 of *BAAS*, page 200, March 1969.

Bernard Lyot. The study of the solar corona and prominences without eclipses (George Darwin Lecture, 1939). *MNRAS*, 99:580, June 1939. doi: 10.1093/mnras/99.8.580.

B. Macintosh, J. R. Graham, T. Barman, R. J. De Rosa, Q. Konopacky, M. S. Marley, C. Marois, E. L. Nielsen, L. Pueyo, A. Rajan, J. Rameau, D. Saumon, J. J. Wang, J. Patience, M. Ammons, P. Arriaga, E. Artigau, S. Beckwith, J. Brewster, S. Bruzzone, J. Bulger, B. Burningham, A. S. Burrows, C. Chen, E. Chiang, J. K. Chilcote, R. I. Dawson, R. Dong, R. Doyon, Z. H. Draper, G. Duchêne, T. M. Esposito, D. Fabrycky, M. P. Fitzgerald, K. B. Follette, J. J. Fortney, B. Gerard, S. Goodsell, A. Z. Greenbaum, P. Hibon, S. Hinkley, T. H. Cotten, L. W. Hung, P. Ingraham, M. Johnson-Groh, P. Kalas, D. Lafreniere, J. E. Larkin, J. Lee, M. Line, D. Long, J. Maire, F. Marchis, B. C. Matthews, C. E. Max, S. Metchev, M. A. Millar-Blanchaer, T. Mittal, C. V. Morley, K. M. Morzinski, R. Murray-Clay, R. Oppenheimer, D. W. Palmer, R. Patel, M. D. Perrin, L. A. Poyneer, R. R. Rafikov, F. T. Rantakyrö, E. L. Rice, P. Rojo, A. R. Rudy, J. B. Ruffio, M. T. Ruiz, N. Sadakuni, L. Saddlemyer, M. Salama, D. Savransky, A. C. Schneider, A. Sivaramakrishnan, I. Song, R. Soummer, S. Thomas, G. Vasisht, J. K. Wallace, K. Ward-Duong, S. J. Wiktorowicz, S. G. Wolff, and B. Zuckerman. Discovery and spectroscopy of the young jovian planet 51 Eri b with the Gemini Planet Imager. *Science*, 350(6256):64–67, October 2015a. doi: 10.1126/science.aac5891.

B. Macintosh, J. R. Graham, T. Barman, R. J. De Rosa, Q. Konopacky, M. S. Marley, C. Marois, E. L. Nielsen, L. Pueyo, A. Rajan, J. Rameau, D. Saumon, J. J. Wang, J. Patience, M. Ammons, P. Arriaga, E. Artigau, S. Beckwith, J. Brewster, S. Bruzzone, J. Bulger, B. Burningham, A. S. Burrows, C. Chen, E. Chiang, J. K. Chilcote, R. I. Dawson, R. Dong, R. Doyon, Z. H. Draper, G. Duchêne, T. M. Esposito, D. Fabrycky, M. P. Fitzgerald, K. B. Follette, J. J. Fortney, B. Gerard, S. Goodsell, A. Z. Greenbaum, P. Hibon, S. Hinkley, T. H. Cotten, L. W. Hung, P. Ingraham, M. Johnson-Groh, P. Kalas, D. Lafreniere, J. E. Larkin, J. Lee, M. Line, D. Long, J. Maire, F. Marchis, B. C. Matthews, C. E. Max, S. Metchev, M. A. Millar-Blanchaer, T. Mittal, C. V. Morley, K. M. Morzinski, R. Murray-Clay, R. Oppenheimer, D. W. Palmer, R. Patel, M. D. Perrin, L. A. Poyneer, R. R. Rafikov, F. T. Rantakyrö, E. L. Rice, P. Rojo, A. R. Rudy, J. B. Ruffio, M. T. Ruiz, N. Sadakuni, L. Saddlemyer, M. Salama, D. Savransky, A. C. Schneider, A. Sivaramakrishnan, I. Song, R. Soummer,

S. Thomas, G. Vasisht, J. K. Wallace, K. Ward-Duong, S. J. Wiktorowicz, S. G. Wolff, and B. Zuckerman. Discovery and spectroscopy of the young jovian planet 51 Eri b with the Gemini Planet Imager. *Science*, 350(6256):64–67, October 2015b. doi: 10.1126/science.aac5891.

B. A. Macintosh, J. R. Graham, D. W. Palmer, R. Doyon, J. Dunn, D. T. Gavel, J. Larkin, B. Oppenheimer, L. Saddlemyer, A. Sivaramakrishnan, J. K. Wallace, B. Bauman, D. A. Erickson, C. Marois, L. A. Poyneer, and R. Soummer. The Gemini Planet Imager: from science to design to construction. In *Adaptive Optics Systems*, volume 7015 of *Proc. SPIE*, page 701518, July 2008. doi: 10.1117/12.788083.

N. Madhusudhan, A. Burrows, and T. Currie. Model Atmospheres for Massive Gas Giants with Thick Clouds: Application to the HR 8799 Planets and Predictions for Future Detections. *ApJ*, 737:34, August 2011. doi: 10.1088/0004-637X/737/1/34.

Nikku Madhusudhan. *Atmospheric Retrieval of Exoplanets*, page 104. 2018. doi: 10.1007/978-3-319-55333-7_104.

J. Maire, M. D. Perrin, R. Doyon, E. Artigau, J. Dunn, D. T. Gavel, J. R. Graham, D. Lafrenière, J. E. Larkin, J.-F. Lavigne, B. A. Macintosh, C. Marois, B. Oppenheimer, D. W. Palmer, L. A. Poyneer, S. Thibault, and J.-P. Véran. Data reduction pipeline for the Gemini Planet Imager. In *Ground-based and Airborne Instrumentation for Astronomy III*, volume 7735 of *Proc. SPIE*, page 773531, July 2010. doi: 10.1117/12.858028.

E. E. Mamajek and L. A. Hillenbrand. Improved Age Estimation for Solar-Type Dwarfs Using Activity-Rotation Diagnostics. *ApJ*, 687:1264–1293, November 2008. doi: 10.1086/591785.

O. Marco and K. J. Brooks. VLT 3-5 micron spectroscopy and imaging of NGC 1068: Does the AGN hide nuclear starburst activity? *AAP*, 398:101–106, January 2003. doi: 10.1051/0004-6361:20021619.

G. D. Marleau and A. Cumming. Constraining the initial entropy of directly detected exoplanets. *MNRAS*, 437(2):1378–1399, January 2014. doi: 10.1093/mnras/stt1967.

M. S. Marley, J. Fortney, S. Seager, and T. Barman. Atmospheres of Extrasolar Giant Planets. In Bo Reipurth, David Jewitt, and Klaus Keil, editors, *Protostars and Planets V*, page 733, January 2007a.

M. S. Marley, D. Saumon, M. Cushing, A. S. Ackerman, J. J. Fortney, and R. Freedman. Masses, Radii, and Cloud Properties of the HR 8799 Planets. *ApJ*, 754:135, August 2012. doi: 10.1088/0004-637X/754/2/135.

Mark S. Marley, Jonathan J. Fortney, Olenka Hubickyj, Peter Bodenheimer, and Jack J. Lissauer. On the Luminosity of Young Jupiters. *ApJ*, 655(1):541–549, 2007b. doi: 10.1086/509759.

Mark S. Marley, Didier Saumon, Channon Visscher, Roxana Lupu, Richard Freedman, Caroline Morley, Jonathan J. Fortney, Christopher Seay, Adam J. R. W. Smith, D. J. Teal, and Ruoyan Wang. The Sonora Brown Dwarf Atmosphere and Evolution Models I. Model Description and Application to Cloudless Atmospheres in Rainout Chemical Equilibrium. *arXiv e-prints*, art. arXiv:2107.07434, July 2021.

Christian Marois, David Lafrenière, René Doyon, Bruce Macintosh, and Daniel Nadeau. Angular Differential Imaging: A Powerful High-Contrast Imaging Technique. *ApJ*, 641(1):556–564, April 2006. doi: 10.1086/500401.

Christian Marois, Bruce Macintosh, Travis Barman, B. Zuckerman, Inseok Song, Jennifer Patience, David Lafrenière, and René Doyon. Direct Imaging of Multiple Planets Orbiting the Star HR 8799. *Science*, 322(5906):1348, 2008. doi: 10.1126/science.1166585.

Christian Marois, B. Gerard, O. Lardière, A. Anthony, C. Bradley, J. Dunn, Q. Fu, T. Hardy, W. Heidrich, G. Herriot, E. Nielsen, S. Sivanandam, D. Sivransky, S. Thibault, W. Thompson, and J. P. Véran. Upgrading the Gemini Planet Imager calibration unit with a photon counting focal plane wavefront sensor. In *Society of Photo-Optical Instrumentation Engineers (SPIE) Conference Series*, volume 11448 of *Society of Photo-Optical Instrumentation Engineers (SPIE) Conference Series*, page 1144873, December 2020. doi: 10.1117/12.2563010.

Emily C. Martin, Gregory N. Mace, Ian S. McLean, Sarah E. Logsdon, Emily L. Rice, J. Davy Kirkpatrick, Adam J. Burgasser, Mark R. McGovern, and Lisa Prato. Surface Gravities for 228 M, L, and T Dwarfs in the NIRSPEC Brown Dwarf Spectroscopic Survey. *ApJ*, 838(1):73, March 2017. doi: 10.3847/1538-4357/aa6338.

Frantz Martinache. Kernel Phase in Fizeau Interferometry. *ApJ*, 724(1):464–469, November 2010. doi: 10.1088/0004-637X/724/1/464.

Frantz Martinache. Spectrally dispersed Fourier-phase analysis for redundant apertures. In Fabien Malbet, Michelle J. Creech-Eakman, and Peter G. Tuthill,

editors, *Optical and Infrared Interferometry and Imaging V*, volume 9907 of *Society of Photo-Optical Instrumentation Engineers (SPIE) Conference Series*, page 990712, August 2016. doi: 10.1117/12.2233395.

P. Martinez, M. Kasper, A. Costille, J. F. Sauvage, K. Dohlen, P. Puget, and J. L. Beuzit. Speckle temporal stability in XAO coronagraphic images. II. Refine model for quasi-static speckle temporal evolution for VLT/SPHERE. *AAP*, 554:A41, June 2013. doi: 10.1051/0004-6361/201220820.

Richard J. Mathar. Refractive index of humid air in the infrared: model fits. *Journal of Optics A: Pure and Applied Optics*, 9(5):470–476, May 2007. doi: 10.1088/1464-4258/9/5/008.

Dimitri Mawet, Laurent Pueyo, Peter Lawson, Laurent Mugnier, Wesley Traub, Anthony Boccaletti, John T. Trauger, Szymon Gladysz, Eugene Serabyn, Julien Milli, Ruslan Belikov, Markus Kasper, Pierre Baudoz, Bruce Macintosh, Christian Marois, Ben Oppenheimer, Harrisson Barrett, Jean-Luc Beuzit, Nicolas Devaney, Julien Girard, Olivier Guyon, John Krist, Bertrand Mennesson, David Mouillet, Naoshi Murakami, Lisa Poyneer, Dmitri Savransky, Christophe Vérinaud, and James K. Wallace. Review of small-angle coronagraphic techniques in the wake of ground-based second-generation adaptive optics systems. In Mark C. Clampin, Giovanni G. Fazio, Howard A. MacEwen, and Jr. Oschmann, Jacobus M., editors, *Space Telescopes and Instrumentation 2012: Optical, Infrared, and Millimeter Wave*, volume 8442 of *Society of Photo-Optical Instrumentation Engineers (SPIE) Conference Series*, page 844204, September 2012. doi: 10.1117/12.927245.

Michel Mayor and Didier Queloz. A Jupiter-mass companion to a solar-type star. *Nature*, 378(6555):355–359, November 1995. doi: 10.1038/378355a0.

B. J. McBride and S. Gordon. *Computer Program for Calculation of Complex Chemical Equilibrium Compositions and Application II. Users Manual and Program Description*. 1996.

M. W. McElwain, T. D. Brandt, M. Janson, G. R. Knapp, M. A. Peters, A. S. Burrows, A. Carlotti, M. A. Carr, T. Groff, J. E. Gunn, O. Guyon, M. Hayashi, N. J. Kasdin, M. Kuzuhara, R. H. Lupton, F. Martinache, D. Spiegel, N. Takato, M. Tamura, E. L. Turner, and R. J. Vanderbei. Scientific design of a high contrast integral field spectrograph for the Subaru Telescope. In *Ground-based and Airborne Instrumentation for Astronomy IV*, volume 8446 of *Proc. SPIE*, page 84469C, September 2012. doi: 10.1117/12.927108.

Christopher F. McKee and Eve C. Ostriker. Theory of Star Formation. *ARAA*, 45(1):565–687, September 2007. doi: 10.1146/annurev.astro.45.051806.110602.

Peter Melchior, David Spergel, and Arianna Lanz. In the Crosshair: Astrometric Exoplanet Detection with WFIRST's Diffraction Spikes. *AJ*, 155(2):102, 2018. doi: 10.3847/1538-3881/aaa422.

Brittany E. Miles, Andrew J. Skemer, Travis S. Barman, Katelyn N. Allers, and Jordan M. Stone. Methane in Analogs of Young Directly Imaged Exoplanets. *ApJ*, 869(1):18, December 2018. doi: 10.3847/1538-4357/aae6cd.

Brittany E. Miles, Andrew J. I. Skemer, Caroline V. Morley, Mark S. Marley, Jonathan J. Fortney, Katelyn N. Allers, Jacqueline K. Faherty, Thomas R. Geballe, Channon Visscher, Adam C. Schneider, Roxana Lupu, Richard S. Freedman, and Gordon L. Bjoraker. Observations of Disequilibrium CO Chemistry in the Coldest Brown Dwarfs. *AJ*, 160(2):63, August 2020. doi: 10.3847/1538-3881/ab9114.

Alessandro Morbidelli and Sean N. Raymond. Challenges in planet formation. *Journal of Geophysical Research (Planets)*, 121(10):1962–1980, October 2016. doi: 10.1002/2016JE005088.

Alessandro Morbidelli, Kleomenis Tsiganis, Aurélien Crida, Harold F. Levison, and Rodney Gomes. Dynamics of the Giant Planets of the Solar System in the Gaseous Protoplanetary Disk and Their Relationship to the Current Orbital Architecture. *AJ*, 134(5):1790–1798, November 2007. doi: 10.1086/521705.

C. Mordasini. Luminosity of young Jupiters revisited. Massive cores make hot planets. *AAP*, 558:A113, October 2013. doi: 10.1051/0004-6361/201321617.

C. V. Morley, J. J. Fortney, M. S. Marley, C. Visscher, D. Saumon, and S. K. Leggett. Neglected Clouds in T and Y Dwarf Atmospheres. *ApJ*, 756:172, September 2012. doi: 10.1088/0004-637X/756/2/172.

C. V. Morley, M. S. Marley, J. J. Fortney, R. Lupu, D. Saumon, T. Greene, and K. Lodders. Water Clouds in Y Dwarfs and Exoplanets. *ApJ*, 787:78, May 2014. doi: 10.1088/0004-637X/787/1/78.

K. M. Morzinski, J. R. Males, A. J. Skemer, L. M. Close, P. M. Hinz, T. J. Rodigas, A. Puglisi, S. Esposito, A. Riccardi, E. Pinna, M. Xompero, R. Briguglio, V. P. Bailey, K. B. Follette, D. Kopon, A. J. Weinberger, and Y.-L. Wu. Magellan Adaptive Optics First-light Observations of the Exoplanet β Pic b. II. 3-5 μm Direct Imaging with MagAO+Clio, and the Empirical Bolometric Luminosity

of a Self-luminous Giant Planet. *ApJ*, 815:108, December 2015. doi: 10.1088/0004-637X/815/2/108.

Gregory Mosby, Bernard Rauscher, Chris Bennett, Edward S. Cheng, Stephanie A. Cheung, Analia N. Cillis, David A. Content, David A. Cottingham, Roger D. Foltz, John D. Gygax, Robert J. Hill, Jeffrey W. Kruk, Jon S. Mah, Lane A. Meier, Chris A. Merchant, Laddawan R. Miko, Eric C. Piquette, Augustyn Waczynski, and Yiting Wen. Properties and characteristics of the Nancy Grace Roman Space Telescope H4RG-10 detectors. 6(4):1 – 37, 2020. doi: 10.1117/1.JATIS.6.4.046001. URL https://doi.org/10.1117/1.JATIS.6.4.046001.

Gijs D. Mulders, Fred J. Ciesla, Michiel Min, and Ilaria Pascucci. The Snow Line in Viscous Disks around Low-mass Stars: Implications for Water Delivery to Terrestrial Planets in the Habitable Zone. *ApJ*, 807(1):9, July 2015. doi: 10.1088/0004-637X/807/1/9.

Gijs D. Mulders, Ilaria Pascucci, Dániel Apai, and Fred J. Ciesla. The Exoplanet Population Observation Simulator. I. The Inner Edges of Planetary Systems. *AJ*, 156(1):24, July 2018. doi: 10.3847/1538-3881/aac5ea.

D. J. Mullan and J. MacDonald. Magnetic Models of the Brown Dwarfs HD 130948b and HD 130948c. *ApJ*, 713:1249–1255, April 2010. doi: 10.1088/0004-637X/713/2/1249.

Matthew W. Muterspaugh, Benjamin F. Lane, S. R. Kulkarni, Maciej Konacki, Bernard F. Burke, M. M. Colavita, M. Shao, William I. Hartkopf, Alan P. Boss, and M. Williamson. THE PHASES DIFFERENTIAL ASTROMETRY DATA ARCHIVE. v. CANDIDATE SUBSTELLAR COMPANIONS TO BINARY SYSTEMS. *The Astronomical Journal*, 140(6):1657–1671, oct 2010. doi: 10.1088/0004-6256/140/6/1657. URL https://doi.org/10.1088/0004-6256/140/6/1657.

Richard P. Nelson, John C. B. Papaloizou, Frédéric Masset, and Willy Kley. The migration and growth of protoplanets in protostellar discs. *MNRAS*, 318(1):18–36, October 2000. doi: 10.1046/j.1365-8711.2000.03605.x.

Eric L. Nielsen, Michael C. Liu, Zahed Wahhaj, Beth A. Biller, Thomas L. Hayward, Jared R. Males, Laird M. Close, Katie M. Morzinski, Andrew J. Skemer, Marc J. Kuchner, Timothy J. Rodigas, Philip M. Hinz, Mark Chun, Christ Ftaclas, and Douglas W. Toomey. The Gemini NICI Planet-Finding Campaign: The Orbit of the Young Exoplanet β Pictoris b. *Astrophysical Journal*, 794(2):158, October 2014. doi: 10.1088/0004-637X/794/2/158.

Eric L. Nielsen, Robert J. De Rosa, Bruce Macintosh, Jason J. Wang, Jean-Baptiste Ruffio, Eugene Chiang, Mark S. Marley, Didier Saumon, Dmitry Savransky, S. Mark Ammons, Vanessa P. Bailey, Travis Barman, Célia Blain, Joanna Bulger, Adam Burrows, Jeffrey Chilcote, Tara Cotten, Ian Czekala, Rene Doyon, Gaspard Duchêne, Thomas M. Esposito, Daniel Fabrycky, Michael P. Fitzgerald, Katherine B. Follette, Jonathan J. Fortney, Benjamin L. Gerard, Stephen J. Goodsell, James R. Graham, Alexandra Z. Greenbaum, Pascale Hibon, Sasha Hinkley, Lea A. Hirsch, Justin Hom, Li-Wei Hung, Rebekah Ilene Dawson, Patrick Ingraham, Paul Kalas, Quinn Konopacky, James E. Larkin, Eve J. Lee, Jonathan W. Lin, Jérôme Maire, Franck Marchis, Christian Marois, Stanimir Metchev, Maxwell A. Millar-Blanchaer, Katie M. Morzinski, Rebecca Oppenheimer, David Palmer, Jennifer Patience, Marshall Perrin, Lisa Poyneer, Laurent Pueyo, Roman R. Rafikov, Abhijith Rajan, Julien Rameau, Fredrik T. Rantakyrö, Bin Ren, Adam C. Schneider, Anand Sivaramakrishnan, Inseok Song, Remi Soummer, Melisa Tallis, Sandrine Thomas, Kimberly Ward-Duong, and Schuyler Wolff. The Gemini Planet Imager Exoplanet Survey: Giant Planet and Brown Dwarf Demographics from 10 to 100 au. *AJ*, 158(1):13, July 2019. doi: 10.3847/1538-3881/ab16e9.

B. R. Oppenheimer, S. R. Kulkarni, and J. R. Stauffer. Brown Dwarfs. In V. Mannings, A. P. Boss, and S. S. Russell, editors, *Protostars and Planets IV*, page 1313, May 2000.

Y. V. Pavlenko. H2O and HDO Bands in the Spectra of Late-Type Dwarfs. *Astronomy Reports*, 46:567–578, July 2002. doi: 10.1134/1.1495033.

A. Pavlov, O. Möller-Nilsson, M. Feldt, T. Henning, J.-L. Beuzit, and D. Mouillet. SPHERE data reduction and handling system: overview, project status, and development. In *Advanced Software and Control for Astronomy II*, volume 7019 of *Proc. SPIE*, page 701939, July 2008. doi: 10.1117/12.789110.

Matthew T. Penny, B. Scott Gaudi, Eamonn Kerins, Nicholas J. Rattenbury, Shude Mao, Annie C. Robin, and Sebastiano Calchi Novati. Predictions of the WFIRST Microlensing Survey. I. Bound Planet Detection Rates. *ApJS*, 241(1): 3, 2019. doi: 10.3847/1538-4365/aafb69.

M. D. Perrin, J. Maire, P. Ingraham, D. Savransky, M. Millar-Blanchaer, S. G. Wolff, J.-B. Ruffio, J. J. Wang, Z. H. Draper, N. Sadakuni, C. Marois, A. Rajan, M. P. Fitzgerald, B. Macintosh, J. R. Graham, R. Doyon, J. E. Larkin, J. K. Chilcote, S. J. Goodsell, D. W. Palmer, K. Labrie, M. Beaulieu, R. J. De Rosa, A. Z. Greenbaum, M. Hartung, P. Hibon, Q. Konopacky, D. Lafreniere, J.-F. Lavigne, F. Marchis, J. Patience, L. Pueyo, F. T. Rantakyrö, R. Soummer,

A. Sivaramakrishnan, S. Thomas, K. Ward-Duong, and S. Wiktorowicz. Gemini Planet Imager observational calibrations I: Overview of the GPI data reduction pipeline. In *Ground-based and Airborne Instrumentation for Astronomy V*, volume 9147 of *Proc. SPIE*, page 91473J, July 2014. doi: 10.1117/12.2055246.

M. A. C. Perryman, L. Lindegren, J. Kovalevsky, E. Hoeg, U. Bastian, P. L. Bernacca, M. Crézé, F. Donati, M. Grenon, M. Grewing, F. van Leeuwen, H. van der Marel, F. Mignard, C. A. Murray, R. S. Le Poole, H. Schrijver, C. Turon, F. Arenou, M. Froeschlé, and C. S. Petersen. The HIPPARCOS Catalogue. *AAP*, 323:L49–L52, July 1997.

M. A. C. Perryman, A. G. A. Brown, Y. Lebreton, A. Gomez, C. Turon, G. Cayrel de Strobel, J. C. Mermilliod, N. Robichon, J. Kovalevsky, and F. Crifo. The Hyades: distance, structure, dynamics, and age. *AAP*, 331:81–120, March 1998.

Michael Perryman. *The Exoplanet Handbook*. 2018.

Michael Perryman, Joel Hartman, Gáspár Á. Bakos, and Lennart Lindegren. Astrometric Exoplanet Detection with Gaia. *ApJ*, 797(1):14, 2014. doi: 10.1088/0004-637X/797/1/14.

Erik A. Petigura, Geoffrey W. Marcy, and Andrew W. Howard. A Plateau in the Planet Population below Twice the Size of Earth. *ApJ*, 770(1):69, June 2013. doi: 10.1088/0004-637X/770/1/69.

P. Pinilla, L. Klarmann, T. Birnstiel, M. Benisty, C. Dominik, and C. P. Dullemond. A tunnel and a traffic jam: How transition disks maintain a detectable warm dust component despite the presence of a large planet-carved gap. *AAP*, 585:A35, January 2016. doi: 10.1051/0004-6361/201527131.

L. Podio, I. Kamp, C. Codella, S. Cabrit, B. Nisini, C. Dougados, G. Sandell, J. P. Williams, L. Testi, W. F. Thi, P. Woitke, R. Meijerink, M. Spaans, G. Aresu, F. Ménard, and C. Pinte. Water Vapor in the Protoplanetary Disk of DG Tau. *Astrophysical Journal Letters*, 766(1):L5, March 2013. doi: 10.1088/2041-8205/766/1/L5.

James B. Pollack, Olenka Hubickyj, Peter Bodenheimer, Jack J. Lissauer, Morris Podolak, and Yuval Greenzweig. Formation of the Giant Planets by Concurrent Accretion of Solids and Gas. *Icarus*, 124(1):62–85, November 1996. doi: 10.1006/icar.1996.0190.

Benjamin Pope, Nick Cvetojevic, Anthony Cheetham, Frantz Martinache, Barnaby Norris, and Peter Tuthill. A demonstration of wavefront sensing and mirror phasing from the image domain. *MNRAS*, 440(1):125–133, May 2014. doi: 10.1093/mnras/stu218.

D. Potter, E. L. Martín, M. C. Cushing, P. Baudoz, W. Brandner, O. Guyon, and R. Neuhäuser. Hokupa'a-Gemini Discovery of Two Ultracool Companions to the Young Star HD 130948. *ApJL*, 567:L133–L136, March 2002. doi: 10.1086/339999.

A. Rajan, J. Rameau, R. J. De Rosa, M. S. Marley, J. R. Graham, B. Macintosh, C. Marois, C. Morley, J. Patience, L. Pueyo, D. Saumon, K. Ward-Duong, S. M. Ammons, P. Arriaga, V. P. Bailey, T. Barman, J. Bulger, A. S. Burrows, J. Chilcote, T. Cotten, I. Czekala, R. Doyon, G. Duchêne, T. M. Esposito, M. P. Fitzgerald, K. B. Follette, J. J. Fortney, S. J. Goodsell, A. Z. Greenbaum, P. Hibon, L.-W. Hung, P. Ingraham, M. Johnson-Groh, P. Kalas, Q. Konopacky, D. Lafrenière, J. E. Larkin, J. Maire, F. Marchis, S. Metchev, M. A. Millar-Blanchaer, K. M. Morzinski, E. L. Nielsen, R. Oppenheimer, D. Palmer, R. I. Patel, M. Perrin, L. Poyneer, F. T. Rantakyrö, J.-B. Ruffio, D. Savransky, A. C. Schneider, A. Sivaramakrishnan, I. Song, R. Soummer, S. Thomas, G. Vasisht, J. K. Wallace, J. J. Wang, S. Wiktorowicz, and S. Wolff. Characterizing 51 Eri b from 1 to 5 μm: A Partly Cloudy Exoplanet. *AJ*, 154:10, July 2017. doi: 10.3847/1538-3881/aa74db.

Bernard J. Rauscher. Teledyne H1RG, H2RG, and H4RG Noise Generator. *PASP*, 127(957):1144, November 2015. doi: 10.1086/684082.

J. T. Rayner, M. C. Cushing, and W. D. Vacca. The Infrared Telescope Facility (IRTF) Spectral Library: Cool Stars. *ApJS*, 185:289–432, December 2009. doi: 10.1088/0067-0049/185/2/289.

L. Ricci, P. Cazzoletti, I. Czekala, S. M. Andrews, D. Wilner, L. Szűcs, G. Lodato, L. Testi, I. Pascucci, S. Mohanty, D. Apai, J. M. Carpenter, and B. P. Bowler. ALMA Observations of the Young Substellar Binary System 2M1207. *AJ*, 154 (1):24, July 2017. doi: 10.3847/1538-3881/aa78a0.

W. K. M. Rice, P. J. Armitage, M. R. Bate, and I. A. Bonnell. The effect of cooling on the global stability of self-gravitating protoplanetary discs. *MNRAS*, 339: 1025–1030, March 2003. doi: 10.1046/j.1365-8711.2003.06253.x.

W. K. M. Rice, Philip J. Armitage, Kenneth Wood, and G. Lodato. Dust filtration at gap edges: implications for the spectral energy distributions of discs with

embedded planets. *MNRAS*, 373(4):1619–1626, December 2006. doi: 10.1111/j.1365-2966.2006.11113.x.

Adam G. Riess, Stefano Casertano, Jay Anderson, John MacKenty, and Alexei V. Filippenko. Parallax beyond a Kiloparsec from Spatially Scanning the Wide Field Camera 3 on the Hubble Space Telescope. *ApJ*, 785(2):161, 2014. doi: 10.1088/0004-637X/785/2/161.

Adam G. Riess, Stefano Casertano, Wenlong Yuan, Lucas Macri, Jay Anderson, John W. MacKenty, J. Bradley Bowers, Kelsey I. Clubb, Alexei V. Filippenko, David O. Jones, and Brad E. Tucker. New Parallaxes of Galactic Cepheids from Spatially Scanning the Hubble Space Telescope: Implications for the Hubble Constant. *ApJ*, 855(2):136, 2018. doi: 10.3847/1538-4357/aaadb7.

Maxime J. Rizzo, Tyler D. Groff, Neil T. Zimmermann, Qian Gong, Avi M. Mandell, Prabal Saxena, Michael W. McElwain, Aki Roberge, John Krist, A. J. Eldorado Riggs, Eric J. Cady, Camilo Mejia Prada, Timothy Brandt, Ewan Douglas, and Kerri Cahoy. Simulating the WFIRST coronagraph integral field spectrograph. In *Society of Photo-Optical Instrumentation Engineers (SPIE) Conference Series*, volume 10400 of *Society of Photo-Optical Instrumentation Engineers (SPIE) Conference Series*, page 104000B, September 2017. doi: 10.1117/12.2273066.

A. C. Robin, X. Luri, C. Reylé, Y. Isasi, E. Grux, S. Blanco-Cuaresma, F. Arenou, C. Babusiaux, M. Belcheva, R. Drimmel, C. Jordi, A. Krone-Martins, E. Masana, J. C. Mauduit, F. Mignard, N. Mowlavi, B. Rocca-Volmerange, P. Sartoretti, E. Slezak, and A. Sozzetti. Gaia Universe model snapshot. A statistical analysis of the expected contents of the Gaia catalogue. *AAP*, 543: A100, July 2012. doi: 10.1051/0004-6361/201118646.

Clive D. Rodgers. *Inverse Methods for Atmospheric Sounding: Theory and Practice*. 2000. doi: 10.1142/3171.

Garreth Ruane, Dimitri Mawet, Bertrand Mennesson, Jeffrey Jewell, and Stuart Shaklan. Vortex coronagraphs for the Habitable Exoplanet Imaging Mission concept: theoretical performance and telescope requirements. *Journal of Astronomical Telescopes, Instruments, and Systems*, 4:015004, January 2018. doi: 10.1117/1.JATIS.4.1.015004.

Steph Sallum, Josh Eisner, Laird M. Close, Philip M. Hinz, Katherine B. Follette, Kaitlin Kratter, Andrew J. Skemer, Vanessa P. Bailey, Runa Briguglio, Denis Defrere, Bruce A. Macintosh, Jared R. Males, Katie M. Morzinski, Alfio T. Puglisi, Timothy J. Rodigas, Eckhart Spalding, Peter G. Tuthill, Amali Vaz,

Alycia Weinberger, and Marco Xomperio. Imaging protoplanets: observing transition disks with non-redundant masking. In Fabien Malbet, Michelle J. Creech-Eakman, and Peter G. Tuthill, editors, *Optical and Infrared Interferometry and Imaging V*, volume 9907 of *Society of Photo-Optical Instrumentation Engineers (SPIE) Conference Series*, page 99070D, August 2016. doi: 10.1117/12.2231764.

D. Saumon and M. S. Marley. The Evolution of L and T Dwarfs in Color-Magnitude Diagrams. *ApJ*, 689:1327–1344, December 2008. doi: 10.1086/592734.

Claude E. Shannon and Warren Weaver. *The mathematical theory of communication*. 1949.

Fang Shi, Eric Cady, Byoung-Joon Seo, Xin An, Kunjithapatham Balasubramanian, Brian Kern, Raymond Lam, David Marx, Dwight Moody, Camilo Mejia Prada, Keith Patterson, Ilya Poberezhskiy, Joel Shields, Erkin Sidick, Hong Tang, John Trauger, Tuan Truong, Victor White, Daniel Wilson, and Hanying Zhou. Dynamic testbed demonstration of WFIRST coronagraph low order wavefront sensing and control (LOWFS/C). In *Society of Photo-Optical Instrumentation Engineers (SPIE) Conference Series*, volume 10400 of *Society of Photo-Optical Instrumentation Engineers (SPIE) Conference Series*, page 104000D, September 2017. doi: 10.1117/12.2274887.

Anand Sivaramakrishnan, Christopher D. Koresko, Russell B. Makidon, Thomas Berkefeld, and Marc J. Kuchner. Ground-based Coronagraphy with High-order Adaptive Optics. *ApJ*, 552(1):397–408, May 2001. doi: 10.1086/320444.

A. J. Skemer, P. M. Hinz, S. Esposito, A. Burrows, J. Leisenring, M. Skrutskie, S. Desidera, D. Mesa, C. Arcidiacono, F. Mannucci, T. J. Rodigas, L. Close, D. McCarthy, C. Kulesa, G. Agapito, D. Apai, J. Argomedo, V. Bailey, K. Boutsia, R. Briguglio, G. Brusa, L. Busoni, R. Claudi, J. Eisner, L. Fini, K. B. Follette, P. Garnavich, R. Gratton, J. C. Guerra, J. M. Hill, W. F. Hoffmann, T. Jones, M. Krejny, J. Males, E. Masciadri, M. R. Meyer, D. L. Miller, K. Morzinski, M. Nelson, E. Pinna, A. Puglisi, S. P. Quanz, F. Quiros-Pacheco, A. Riccardi, P. Stefanini, V. Vaitheeswaran, J. C. Wilson, and M. Xompero. First Light LBT AO Images of HR 8799 bcde at 1.6 and 3.3 μm: New Discrepancies between Young Planets and Old Brown Dwarfs. *ApJ*, 753:14, July 2012. doi: 10.1088/0004-637X/753/1/14.

A. J. Skemer, M. S. Marley, P. M. Hinz, K. M. Morzinski, M. F. Skrutskie, J. M. Leisenring, L. M. Close, D. Saumon, V. P. Bailey, R. Briguglio, D. Defrere,

S. Esposito, K. B. Follette, J. M. Hill, J. R. Males, A. Puglisi, T. J. Rodigas, and M. Xompero. Directly Imaged L-T Transition Exoplanets in the Mid-infrared. *ApJ*, 792:17, September 2014. doi: 10.1088/0004-637X/792/1/17.

A. J. Skemer, P. Hinz, M. Montoya, M. F. Skrutskie, J. Leisenring, O. Durney, C. E. Woodward, J. Wilson, M. Nelson, V. Bailey, D. Defrere, and J. Stone. First light with ALES: A 2-5 micron adaptive optics Integral Field Spectrograph for the LBT. In *Techniques and Instrumentation for Detection of Exoplanets VII*, volume 9605 of *Proc. SPIE*, page 96051D, September 2015. doi: 10.1117/12.2187284.

A. J. Skemer, P. Hinz, J. Stone, M. Skrutskie, C. E. Woodward, J. Leisenring, and Z. Briesemeister. ALES: Overview and Upgrades. *ArXiv e-prints*, August 2018a.

Andrew J. Skemer, Caroline V. Morley, Katelyn N. Allers, Thomas R. Geballe, Mark S. Marley, Jonathan J. Fortney, Jacqueline K. Faherty, Gordon L. Bjoraker, and Roxana Lupu. The First Spectrum of the Coldest Brown Dwarf. *Astrophysical Journal*, 826(2):L17, August 2016a. doi: 10.3847/2041-8205/826/2/L17.

Andrew J. Skemer, Caroline V. Morley, Neil T. Zimmerman, Michael F. Skrutskie, Jarron Leisenring, Esther Buenzli, Mickael Bonnefoy, Vanessa Bailey, Philip Hinz, Denis Defrére, Simone Esposito, Dániel Apai, Beth Biller, Wolfgang Brandner, Laird Close, Justin R. Crepp, Robert J. De Rosa, Silvano Desidera, Josh Eisner, Jonathan Fortney, Richard Freedman, Thomas Henning, Karl-Heinz Hofmann, Taisiya Kopytova, Roxana Lupu, Anne-Lise Maire, Jared R. Males, Mark Marley, Katie Morzinski, Apurva Oza, Jenny Patience, Abhijith Rajan, George Rieke, Dieter Schertl, Joshua Schlieder, Jordan Stone, Kate Su, Amali Vaz, Channon Visscher, Kimberly Ward-Duong, Gerd Weigelt, and Charles E. Woodward. The LEECH Exoplanet Imaging Survey: Characterization of the Coldest Directly Imaged Exoplanet, GJ 504 b, and Evidence for Superstellar Metallicity. *ApJ*, 817(2):166, February 2016b. doi: 10.3847/0004-637X/817/2/166.

Andrew J. Skemer, Philip Hinz, Jordan Stone, Michael Skrutskie, Charles E. Woodward, Jarron Leisenring, and Zackery Briesemeister. ALES: overview and upgrades. In Christopher J. Evans, Luc Simard, and Hideki Takami, editors, *Ground-based and Airborne Instrumentation for Astronomy VII*, volume 10702 of *Society of Photo-Optical Instrumentation Engineers (SPIE) Conference Series*, page 107020C, July 2018b. doi: 10.1117/12.2314091.

Andrew J. Skemer, Deno Stelter, Dimitri Mawet, Michael Fitzgerald, Benjamin Mazin, Olivier Guyon, Christian Marois, Zackery Briesemeister, Timothy Brandt, Jeffrey Chilcote, Jacques-Robert Delorme, Nemanja Jovanovic, Jessica Lu, Maxwell Millar-Blanchaer, James Wallace, Gautam Vasisht, Lewis C. Roberts, and Ji Wang. The planetary systems imager: 2-5 micron channel. In Christopher J. Evans, Luc Simard, and Hideki Takami, editors, *Ground-based and Airborne Instrumentation for Astronomy VII*, volume 10702 of *Society of Photo-Optical Instrumentation Engineers (SPIE) Conference Series*, page 10702A5, July 2018c. doi: 10.1117/12.2314173.

M. F. Skrutskie, T. Jones, P. Hinz, P. Garnavich, J. Wilson, M. Nelson, E. Solheid, O. Durney, W. Hoffmann, V. Vaitheeswaran, T. McMahon, J. Leisenring, and A. Wong. The Large Binocular Telescope mid-infrared camera (LMIRcam): final design and status. In *Ground-based and Airborne Instrumentation for Astronomy III*, volume 7735 of *Proc. SPIE*, page 77353H, July 2010. doi: 10.1117/12.857724.

B. A. Smith and R. J. Terrile. A Circumstellar Disk around β Pictoris. *Science*, 226(4681):1421–1424, December 1984. doi: 10.1126/science.226.4681.1421.

R. Soummer, L. Pueyo, and J. Larkin. Detection and Characterization of Exoplanets and Disks Using Projections on Karhunen-Loève Eigenimages. *The Astronomical Journal Letters*, 755:L28, August 2012. doi: 10.1088/2041-8205/755/2/L28.

A. Sozzetti, P. Giacobbe, M. G. Lattanzi, G. Micela, R. Morbidelli, and G. Tinetti. Astrometric detection of giant planets around nearby M dwarfs: the Gaia potential. *MNRAS*, 437(1):497–509, 2014. doi: 10.1093/mnras/stt1899.

E. Spalding, P. Hinz, S. Ertel, E. Maier, and J. Stone. Towards controlled Fizeau observations with the Large Binocular Telescope. *ArXiv e-prints*, June 2018a.

Eckhart Spalding, Phil Hinz, Steve Ertel, Erin Maier, and Jordan Stone. Towards controlled Fizeau observations with the Large Binocular Telescope. In Michelle J. Creech-Eakman, Peter G. Tuthill, and Antoine Mérand, editors, *Optical and Infrared Interferometry and Imaging VI*, volume 10701 of *Society of Photo-Optical Instrumentation Engineers (SPIE) Conference Series*, page 107010J, July 2018b. doi: 10.1117/12.2315498.

W. B. Sparks, H. C. Ford, J. Krist, M. Clampin, and D. Golimowski. Wavelength Dependence of the ACS Coronagraphic PSF. In *American Astronomical Society Meeting Abstracts*, volume 201 of *American Astronomical Society Meeting Abstracts*, page 21.03, December 2002.

David S. Spiegel and Adam Burrows. Spectral and Photometric Diagnostics of Giant Planet Formation Scenarios. *ApJ*, 745(2):174, February 2012. doi: 10.1088/0004-637X/745/2/174.

D. Stamatellos, D. A. Hubber, and A. P. Whitworth. Brown dwarf formation by gravitational fragmentation of massive, extended protostellar discs. *MNRAS*, 382:L30–L34, November 2007. doi: 10.1111/j.1745-3933.2007.00383.x.

R. Deno Stelter, Andrew J. Skemer, Steph Sallum, Renate Kupke, Phil Hinz, Dimitri Mawet, Rebecca Jensen-Clem, Christopher Ratliffe, Nicholas MacDonald, William Deich, Gabriel Kruglikov, Marc Kassis, Jim Lyke, Zackary Briesemeister, Brittany Miles, Benjamin Gerard, Michael Fitzgerald, Timothy Brandt, and Christian Marois. Update on the preliminary design of SCALES: the Santa Cruz Array of Lenslets for Exoplanet Spectroscopy. In *Society of Photo-Optical Instrumentation Engineers (SPIE) Conference Series*, volume 11447 of *Society of Photo-Optical Instrumentation Engineers (SPIE) Conference Series*, page 1144764, December 2020. doi: 10.1117/12.2562768.

D. C. Stephens, S. K. Leggett, M. C. Cushing, M. S. Marley, D. Saumon, T. R. Geballe, D. A. Golimowski, X. Fan, and K. S. Noll. The 0.8-14.5 μm Spectra of Mid-L to Mid-T Dwarfs: Diagnostics of Effective Temperature, Grain Sedimentation, Gas Transport, and Surface Gravity. *ApJ*, 702:154–170, September 2009. doi: 10.1088/0004-637X/702/1/154.

D. J. Stevenson. The search for brown dwarfs. *Annual Rev. Astron. Astrophys*, 29:163–193, 1991. doi: 10.1146/annurev.aa.29.090191.001115.

T. Stolker, M. Min, D. M. Stam, P. Mollière, C. Dominik, and L. B. F. M. Waters. Polarized scattered light from self-luminous exoplanets. Three-dimensional scattering radiative transfer with ARTES. *AAP*, 607:A42, November 2017. doi: 10.1051/0004-6361/201730780.

J. M. Stone, J. Eisner, A. Skemer, K. M. Morzinski, L. Close, J. Males, T. J. Rodigas, P. Hinz, and A. Puglisi. L-band Spectroscopy with Magellan-AO/Clio2: First Results on Young Low-mass Companions. *ApJ*, 829:39, September 2016. doi: 10.3847/0004-637X/829/1/39.

J. M. Stone, A. J. Skemer, P. Hinz, Z. Briesemeister, T. Barman, C. E. Woodward, M. Skrutskie, and J. Leisenring. On-Sky Operations with the ALES Integral Field Spectrograph. *ArXiv e-prints*, August 2018a.

Jordan M. Stone, Andrew J. Skemer, Philip Hinz, Zack Briesemeister, Travis Barman, Charles E. Woodward, Mike Skrutskie, and Jarron Leisenring. On-sky

operations with the ALES integral field spectrograph. In Christopher J. Evans, Luc Simard, and Hideki Takami, editors, *Ground-based and Airborne Instrumentation for Astronomy VII*, volume 10702 of *Society of Photo-Optical Instrumentation Engineers (SPIE) Conference Series*, page 107023F, July 2018b. doi: 10.1117/12.2313977.

Jordan M. Stone, Andrew J. Skemer, Philip M. Hinz, Mariangela Bonavita, Kaitlin M. Kratter, Anne-Lise Maire, Denis Defrere, Vanessa P. Bailey, Eckhart Spalding, Jarron M. Leisenring, S. Desidera, M. Bonnefoy, Beth Biller, Charles E. Woodward, Th. Henning, Michael F. Skrutskie, J. A. Eisner, Justin R. Crepp, Jennifer Patience, Gerd Weigelt, Robert J. De Rosa, Joshua Schlieder, Wolfgang Brandner, Dániel Apai, Kate Su, Steve Ertel, Kimberly Ward-Duong, Katie M. Morzinski, Dieter Schertl, Karl-Heinz Hofmann, Laird M. Close, Stefan S. Brems, Jonathan J. Fortney, Apurva Oza, Esther Buenzli, and Brandon Bass. The LEECH Exoplanet Imaging Survey: Limits on Planet Occurrence Rates under Conservative Assumptions. *Astronomical Journal*, 156(6):286, December 2018c. doi: 10.3847/1538-3881/aaec00.

Jordan M. Stone, Travis Barman, Andrew J. Skemer, Zackery W. Briesemeister, Laci S. Brock, Philip M. Hinz, Jarron M. Leisenring, Charles E. Woodward, Michael F. Skrutskie, and Eckhart Spalding. High-contrast Thermal Infrared Spectroscopy with ALES: The 3-4 μm Spectrum of κ Andromedae b. *AJ*, 160 (6):262, December 2020. doi: 10.3847/1538-3881/abbef3.

L. Tal-Or, S. Zucker, I. Ribas, G. Anglada-Escudé, and A. Reiners. Prospects for detecting the astrometric signature of Barnard's Star b. *AAP*, 623:A10, 2019. doi: 10.1051/0004-6361/201834643.

Edward W. Thommes, Martin J. Duncan, and Harold F. Levison. The formation of Uranus and Neptune in the Jupiter-Saturn region of the Solar System. *Nature*, 402(6762):635–638, December 1999. doi: 10.1038/45185.

Daniel Peter Thorngren and Jonathan J. Fortney. Bayesian Inference of the Composition and Inflation Power of Hot Jupiters. In *AAS/Division for Planetary Sciences Meeting Abstracts #48*, volume 48 of *AAS/Division for Planetary Sciences Meeting Abstracts*, page 212.08, October 2016.

G. Tinetti, P. Drossart, P. Eccleston, P. Hartogh, A. Heske, J. Leconte, G. Micela, M. Ollivier, G. Pilbratt, L. Puig, D. Turrini, B. Vandenbussche, P. Wolkenberg, E. Pascale, J. P. Beaulieu, M. Güdel, M. Min, M. Rataj, T. Ray, I. Ribas, J. Barstow, N. Bowles, A. Coustenis, V. Coudé du Foresto, L. Decin, T. Encrenaz, F. Forget, M. Friswell, M. Griffin, P. O. Lagage, P. Malaguti, A. Moneti, J. C. Morales, E. Pace, M. Rocchetto, S. Sarkar, F. Selsis, W. Taylor,

J. Tennyson, O. Venot, I. P. Waldmann, G. Wright, T. Zingales, and M. R. Zapatero-Osorio. The science of ARIEL (Atmospheric Remote-sensing Infrared Exoplanet Large-survey). volume 9904 of *Proc. SPIE*, page 99041X, 2016. doi: 10.1117/12.2232370.

A. T. Tokunaga, D. A. Simons, and W. D. Vacca. The Mauna Kea Observatories Near-Infrared Filter Set. II. Specifications for a New JHKL'M' Filter Set for Infrared Astronomy. *PASP*, 114:180–186, February 2002. doi: 10.1086/338545.

W. A. Traub and B. R. Oppenheimer. Direct Imaging of Exoplanets. In S. Seager, editor, *Exoplanets*, pages 111–156. 2010.

K. Tsiganis, R. Gomes, A. Morbidelli, and H. F. Levison. Origin of the orbital architecture of the giant planets of the Solar System. *Nature*, 435(7041):459–461, May 2005. doi: 10.1038/nature03539.

Peter G. Tuthill, John D. Monnier, and William C. Danchi. Aperture masking interferometry on the Keck I Telescope: new results from the diffraction limit. 4006:491–498, July 2000. doi: 10.1117/12.390244.

J. A. Valenti and D. A. Fischer. Spectroscopic Properties of Cool Stars (SPOCS). I. 1040 F, G, and K Dwarfs from Keck, Lick, and AAT Planet Search Programs. *ApJS*, 159:141–166, July 2005. doi: 10.1086/430500.

S. van der Walt, S. C. Colbert, and G. Varoquaux. The NumPy Array: A Structure for Efficient Numerical Computation. *Computing in Science and Engineering*, 13(2):22–30, March 2011. doi: 10.1109/MCSE.2011.37.

Julian C. van Eyken, David R. Ciardi, Kaspar von Braun, Stephen R. Kane, Peter Plavchan, Chad F. Bender, Timothy M. Brown, Justin R. Crepp, Benjamin J. Fulton, Andrew W. Howard, Steve B. Howell, Suvrath Mahadevan, Geoffrey W. Marcy, Avi Shporer, Paula Szkody, Rachel L. Akeson, Charles A. Beichman, Andrew F. Boden, Dawn M. Gelino, D. W. Hoard, Solange V. Ramírez, Luisa M. Rebull, John R. Stauffer, Joshua S. Bloom, S. Bradley Cenko, Mansi M. Kasliwal, Shrinivas R. Kulkarni, Nicholas M. Law, Peter E. Nugent, Eran O. Ofek, Dovi Poznanski, Robert M. Quimby, Richard Walters, Carl J. Grillmair, Russ Laher, David B. Levitan, Branimir Sesar, and Jason A. Surace. The PTF Orion Project: A Possible Planet Transiting a T-Tauri Star. *ApJ*, 755(1):42, August 2012. doi: 10.1088/0004-637X/755/1/42.

Maaike van Kooten, Niek Doelman, and Matthew Kenworthy. Impact of time-variant turbulence behavior on prediction for adaptive optics systems. *Journal of the Optical Society of America A*, 36(5):731, May 2019. doi: 10.1364/JOSAA.36.000731.

F. van Leeuwen. Validation of the new Hipparcos reduction. *AAP*, 474(2):653–664, 2007. doi: 10.1051/0004-6361:20078357.

A. Vigan, J. Patience, C. Marois, M. Bonavita, R. J. De Rosa, B. Macintosh, I. Song, R. Doyon, B. Zuckerman, D. Lafrenière, and T. Barman. The International Deep Planet Survey. I. The frequency of wide-orbit massive planets around A-stars. *Astronomy & Astrophysics*, 544:A9, August 2012. doi: 10.1051/0004-6361/201218991.

A. Vigan, C. Fontanive, M. Meyer, B. Biller, M. Bonavita, M. Feldt, S. Desidera, G. D. Marleau, A. Emsenhuber, R. Galicher, K. Rice, D. Forgan, C. Mordasini, R. Gratton, H. Le Coroller, A. L. Maire, F. Cantalloube, G. Chauvin, A. Cheetham, J. Hagelberg, A. M. Lagrange, M. Langlois, M. Bonnefoy, J. L. Beuzit, A. Boccaletti, V. D'Orazi, P. Delorme, C. Dominik, Th. Henning, M. Janson, E. Lagadec, C. Lazzoni, R. Ligi, F. Menard, D. Mesa, S. Messina, C. Moutou, A. Müller, C. Perrot, M. Samland, H. M. Schmid, T. Schmidt, E. Sissa, M. Turatto, S. Udry, A. Zurlo, L. Abe, J. Antichi, R. Asensio-Torres, A. Baruffolo, P. Baudoz, J. Baudrand, A. Bazzon, P. Blanchard, A. J. Bohn, S. Brown Sevilla, M. Carbillet, M. Carle, E. Cascone, J. Charton, R. Claudi, A. Costille, V. De Caprio, A. Delboulbé, K. Dohlen, N. Engler, D. Fantinel, P. Feautrier, T. Fusco, P. Gigan, J. H. Girard, E. Giro, D. Gisler, L. Gluck, C. Gry, N. Hubin, E. Hugot, M. Jaquet, M. Kasper, D. Le Mignant, M. Llored, F. Madec, Y. Magnard, P. Martinez, D. Maurel, O. Möller-Nilsson, D. Mouillet, T. Moulin, A. Origné, A. Pavlov, D. Perret, C. Petit, J. Pragt, P. Puget, P. Rabou, J. Ramos, E. L. Rickman, F. Rigal, S. Rochat, R. Roelfsema, G. Rousset, A. Roux, B. Salasnich, J. F. Sauvage, A. Sevin, C. Soenke, E. Stadler, M. Suarez, Z. Wahhaj, L. Weber, and F. Wildi. The SPHERE infrared survey for exoplanets (SHINE). III. The demographics of young giant exoplanets below 300 au with SPHERE. *AAP*, 651:A72, July 2021. doi: 10.1051/0004-6361/202038107.

J. J. Wang, J. R. Graham, L. Pueyo, P. Kalas, M. A. Millar-Blanchaer, J.-B. Ruffio, R. J. De Rosa, S. M. Ammons, P. Arriaga, V. P. Bailey, T. S. Barman, J. Bulger, A. S. Burrows, A. Cardwell, C. H. Chen, J. K. Chilcote, T. Cotten, M. P. Fitzgerald, K. B. Follette, R. Doyon, G. Duchêne, A. Z. Greenbaum, P. Hibon, L.-W. Hung, P. Ingraham, Q. M. Konopacky, J. E. Larkin, B. Macintosh, J. Maire, F. Marchis, M. S. Marley, C. Marois, S. Metchev, E. L. Nielsen, R. Oppenheimer, D. W. Palmer, R. Patel, J. Patience, M. D. Perrin, L. A. Poyneer, A. Rajan, J. Rameau, F. T. Rantakyrö, D. Savransky, A. Sivaramakrishnan, I. Song, R. Soummer, S. Thomas, G. Vasisht, D. Vega, J. K. Wallace, K. Ward-Duong, S. J. Wiktorowicz, and S. G. Wolff. The Orbit and Transit

Prospects for β Pictoris b Constrained with One Milliarcsecond Astrometry. *AJ*, 152:97, October 2016. doi: 10.3847/0004-6256/152/4/97.

Jason J. Wang, Jean-Baptiste Ruffio, Evan Morris, Jacques-Robert Delorme, Nemanja Jovanovic, Jacklyn Pezzato, Daniel Echeverri, Luke Finnerty, Callie Hood, J. J. Zanazzi, Marta L. Bryan, Charlotte Z. Bond, Sylvain Cetre, Emily C. Martin, Dimitri Mawet, Andy Skemer, Ashley Baker, Jerry W. Xuan, J. Kent Wallace, Ji Wang, Randall Bartos, Geoffrey A. Blake, Andy Boden, Cam Buzard, Benjamin Calvin, Mark Chun, Greg Doppmann, Trent J. Dupuy, Gaspard Duchêne, Y. Katherina Feng, Michael P. Fitzgerald, Jonathan Fortney, Richard S. Freedman, Heather Knutson, Quinn Konopacky, Scott Lilley, Michael C. Liu, Ronald Lopez, Roxana Lupu, Mark S. Marley, Tiffany Meshkat, Brittany Miles, Maxwell Millar-Blanchaer, Sam Ragland, Arpita Roy, Garreth Ruane, Ben Sappey, Tobias Schofield, Lauren Weiss, Edward Wetherell, Peter Wizinowich, and Marie Ygouf. Detection and Bulk Properties of the HR 8799 Planets with High-resolution Spectroscopy. *AJ*, 162(4):148, October 2021. doi: 10.3847/1538-3881/ac1349.

Joshua N. Winn and Daniel C. Fabrycky. The Occurrence and Architecture of Exoplanetary Systems. *ARAA*, 53:409–447, 2015. doi: 10.1146/annurev-astro-082214-122246.

A. Wolszczan and D. A. Frail. A planetary system around the millisecond pulsar PSR1257 + 12. *Nature*, 355(6356):145–147, January 1992. doi: 10.1038/355145a0.

E. L. Wright, P. R. M. Eisenhardt, A. K. Mainzer, M. E. Ressler, R. M. Cutri, T. Jarrett, J. D. Kirkpatrick, D. Padgett, R. S. McMillan, M. Skrutskie, S. A. Stanford, M. Cohen, R. G. Walker, J. C. Mather, D. Leisawitz, T. N. Gautier, III, I. McLean, D. Benford, C. J. Lonsdale, A. Blain, B. Mendez, W. R. Irace, V. Duval, F. Liu, D. Royer, I. Heinrichsen, J. Howard, M. Shannon, M. Kendall, A. L. Walsh, M. Larsen, J. G. Cardon, S. Schick, M. Schwalm, M. Abid, B. Fabinsky, L. Naes, and C.-W. Tsai. The Wide-field Infrared Survey Explorer (WISE): Mission Description and Initial On-orbit Performance. *AJ*, 140:1868–1881, December 2010. doi: 10.1088/0004-6256/140/6/1868.

I. Yamamura, T. Tsuji, and T. Tanabé. AKARI Observations of Brown Dwarfs. I. CO and CO_2 Bands in the Near-infrared Spectra. *ApJ*, 722:682–698, October 2010. doi: 10.1088/0004-637X/722/1/682.

Liang Yu, Joshua N. Winn, Michaël Gillon, Simon Albrecht, Saul Rappaport, Allyson Bieryla, Fei Dai, Laetitia Delrez, Lynne Hillenbrand, Matthew J. Holman, Andrew W. Howard, Chelsea X. Huang, Howard Isaacson, Emmanuel

Jehin, Monika Lendl, Benjamin T. Montet, Philip Muirhead, Roberto Sanchis-Ojeda, and Amaury H. M. J. Triaud. Tests of the Planetary Hypothesis for PTFO 8-8695b. *ApJ*, 812(1):48, October 2015. doi: 10.1088/0004-637X/812/1/48.

Guchuan Zhu, Jean Lévine, Laurent Praly, and Yves-Alain Peter. Flatness-based control of electrostatically actuated mems with application to adaptive optics: A simulation study. *Journal of Microelectromechanical Systems*, 15, 11 2006. doi: 10.1109/JMEMS.2006.880198.

N. Zimmerman, D. Brenner, B. R. Oppenheimer, I. R. Parry, S. Hinkley, S. Hunt, and R. Roberts. A Data-Cube Extraction Pipeline for a Coronagraphic Integral Field Spectrograph. *PASP*, 123:746, June 2011. doi: 10.1086/660818.

A. Zurlo, A. Vigan, D. Mesa, R. Gratton, C. Moutou, M. Langlois, R. U. Claudi, L. Pueyo, A. Boccaletti, A. Baruffolo, J.-L. Beuzit, A. Costille, S. Desidera, K. Dohlen, M. Feldt, T. Fusco, T. Henning, M. Kasper, P. Martinez, O. Moeller-Nilsson, D. Mouillet, A. Pavlov, P. Puget, J.-F. Sauvage, M. Turatto, S. Udry, F. Vakili, R. Waters, and R. F. Wildi. Performance of the VLT Planet Finder SPHERE. I. Photometry and astrometry precision with IRDIS and IFS in laboratory. *AAP*, 572:A85, December 2014. doi: 10.1051/0004-6361/201424204.